A process model for friction stir welding of age hardening aluminium alloys

by

Øyvind Frigaard

A thesis submitted to
The Norwegian University of Science and Technology (NTNU)
in partial fulfilment of the requirements for the degree of

Doktor Ingeniør

Trondheim,
August 1999

PREFACE

This work has been carried out at the Department of Materials Technology and Electrochemistry, The Norwegian University of Science and Technology. The author started on a three-year doctoral programme autumn 1996.

Professor Øysten Grong, NTNU initiated the work, in collaboration with dr.ing. Ole Terje Midling at Hydro Aluminium, R&D Materials Technology. The work has been organised via the "Aluminium in Ship" programme, a group sponsored project financed by Hydro, Kværner, Det Norske Veritas and the Norwegian Research Council.

The main results presented in this thesis have been published in various conference proceedings, including: The 7th International Conference on Joints in Aluminium (INALCO'98), Cambridge, UK, 15-17 April 1998, The 6th International Conference on Aluminium Alloys (ICAA-6), Toyohasi, Japan, 5-10 July 1998, The First International Symposium on Friction Stir Welding, Thousand Oaks, California, USA, 14-16 June 1999. A condensed version of the thesis is also being prepared for publication in Metallurgical and Materials Transactions.

Trondheim, 1999-08-09

Øyvind Frigaard

ACKNOWLEDGEMENTS

ABSTRACT

This doctoral thesis is concerned with process modelling of friction stir welding (FSW). The primary objective of the work has been to develop a process model within the scope of a personal computer. The model presented here calculates the thermal field during welding and the resulting hardness distribution for a wide range of operating conditions.

The thesis is divided into seven parts where Part I is a literature review, starting with a general presentation of the friction stir welding technology and some of the reported advantages obtained using this technique. Then a general review of friction stir welding of age hardenable aluminium alloys is presented. This part also includes detailed description of the Al-Mg-Si and Al-Zn-Mg systems, with particular emphasis on the microstructural changes occurring in the heat-affected zone (HAZ) during welding of these alloys.

In Part II of the thesis a 2-D numerical heat flow model for friction stir welding of aluminium alloys has been developed, based on the finite difference approach. The code is implemented in MatLab 4.0, and is validated by comparison with outputs from the exact analytical line source solution. The model predictions show that the welding cycle can be divided into four main stages:
  (i)   The stationary heating period: where the material beneath the shoulder is preheated to a certain temperature to sustain the plastic deformation during welding.
  (i)   The transient heating period: where the heat starts to build up around the shoulder as the tool moves until saturation occurs.
  (ii) The pseudo steady state period: where the thermal field around the tool remains essentially constant during the welding operation.
  (iii) The post steady state period: where reflection of heat from the end plate surface leads to additional build-up of heat around the tool shoulder.
It is concluded that the simplified 2-D heat flow model captures the basic features of the FSW process, but is not suitable for quantitative predictions because it omits a consideration of the heat conduction occurring in the through-thickness direction of the plate.

In Part III of the thesis a full 3-D numerical heat flow model for friction stir welding of aluminium alloys has been developed, based on the method of finite differences. A number of specific features are built into the model; i.e. heat generation both beneath the tool shoulder and around the rotating pin and the

use of an non-uniform grid for a quick and reliable solution of the heat flow equation. The algorithm is implemented in MatLab 5.2, and calculates the thermal programme in butt welds for fixed starting conditions. The results show that the temperature in front of the tool is most critical, since the parent material must be pre-heated to a certain temperature before it can sustain the plastic deformation. The heating rate is, in turn, determined by the applied heat input and the geometry of the aluminium plate. In practice, this imposes restrictions on the welding speed v and the net power q_0 for a given plate thickness d to avoid surface defects or excessive HAZ softening. At pseudo-steady state the different welding variables can be combined in a single process parameter, q_0/vd (kJ/mm^2), which controls the thermal programme during FSW.

Part IV of the thesis is concerned with measurements of the temperature distribution during FSW. The experiments were performed at Hydro R&D Materials Technology, Karmøy, Norway, using a dedicated FSW machine. The measurements were performed on 7108-T79 and 6082-T6 plates, using an insulated backing in order to avoid excessive heat loss to the surroundings. The in-situ thermocouple measurements were done both in the HAZ and in the region adjacent to the plastizied region at three different welding speeds (5, 8 and 12mm/s). Based on these results it is concluded that the heat source during FSW is axisymmetric and that the outer contour of the plastically deformed region corresponds approximately to the 450°C isotherm.

Part V of the thesis is concerned with characterisation of the microstructure within the plastically deformed region of the friction stir welds. First a series of post weld heat treatment experiments is performed in order to determine whether the static recrystallisation behaviour is affected by spatial variations in the subgrain structure. Subsequently, the electron back-scattered diffraction (EBSD) technique in scanning electron microscope (SEM) is used to reveal the subgrain structure of the as welded materials. It is concluded that the plastically defromed region can be divided in two distinct regions after the post weld heat treatment, i.e. recrystallised and non-recrystallised regions. The subgrain size in the regions recrystallised after post weld heat treatment is smaller compared to the regions that did not recrystallise. It is also observed that the subgrain structure contains both high and low angle grain boundaries, showing that dynamic recovery is the major softening mechanism during FSW of aluminium alloys. Calculations based on the Zener-Hollomon equation suggest that the local strain rate within the plastically deformed region varies from about 1 to 20s^{-1}.

In Part VI of the thesis the 3-D heat flow model is tested against the experimental results obtained from the in-situ thermocouple measurments. Furthermore, the thermal model is coupled with dedicated microstructure models in order to calculate the hardness distribution following welding. The results show that the process model adequately reproduces the thermal field during welding and the corresponding hardness distribution following welding. It is concluded that the combination of a microstructure model with an appropriate heat flow model creates a powerful tool for alloy design and optimisation of welding conditions for both Al-Mg-Si and Al-Zn-Mg extrusions.

Finally, in Part VII of the thesis the process model is applied in two different case studies pertaining to FSW of 6082-T6 and 7108-T79 extrusions, respectively. These are meant to illustrate the aptness of the approach and show how process modelling techniques can be used to rationalise problems of major industrial importance.

TABLE OF CONTENTS

PART I: GENERAL INTRODUCTION

1.1 Introduction

From being a material mainly used in drink cans and cooking foil aluminium alloys now rank second to steel as the most important structural material. Aluminium based alloys show good resistance to general corrosion, and have better stiffness/weight and strength/weight properties than steel /1/. The dominant use of aluminium alloys is in building industry and construction, e.g. panels, roofs and frames. Still the fastest growing sector is in transport, where aluminium alloys replace steel and cast iron in cars and mass-transit systems. This is due to the increasing demand of less environmental impact through weight reductions.

Within the transport industry heat treatable wrought aluminium alloys are most widely used. The versatility of the rolling and extrusion process routs makes it possible to produce complex sections of long length that exhibit medium to high strength. In order to use these profiles in load bearing structures joining is a key technology.

In 1991 W. Thomas at TWI invented and filed a patent/2/ for a solid state bonding technique for aluminium called friction stir welding (FSW). FSW has successfully been used to join a number of aluminium alloys, also those normally considered difficult to join by conventional fusion welding techniques, with low-distortion and reproducible quality. The process is implement to product designs previously not feasible /3,4/, including:

- Extruded lightweight panels, which are difficult to produce in large size, are welded together to form large structures.
- Dissimilar material combinations are joined, e.g. castings to extrusions, casting to wrought products etc.
- Multi-component shapes, such as long, large cross section, box sections and spars, which normally would not be practical or cost ineffective to extrude or cast.

In order to take full advantage of the FSW process, it is necessary to understand and predict the microstructure evolution during welding. All welding techniques applied to heat treatable alloys represent local reheating of a material that has undergone a tight temperature control to gain the desired mechanical properties. Hence, due concideration must be given to the HAZ (heat affected zone) thermal programme during welding in order to select welding parameters suitable for the given application /5,6/.

1.2 Basic principles of the FSW process

Figure 1 show the basic principles of the FSW process. The parts to be joint are placed on a backing plate and clamped in a manner that prevents the abutting joint faces from being forced apart. A cylindrical-shouldered tool, with a specially profiled projecting pin, is rotated and slowly pierced into the joint line. The pin length is equal to the required weld depth. When the rotating pin contacts the work surface, it rapidly friction heats the material at the joint contact, thus softening the material. Under an applied force the pin forges the material in its path, until the shoulder of the pin is in intimate contact with the work surface. At this juncture, the friction heating and deformation produced by the rotating shoulder and pin produces a substantial plasticized layer of metal beneath the tool shoulder and about the pin. When the pin is moved against the workpiece, or vice versa, the plasticized material at the shear side is crushed by the leading face of the pin profile and transported to the flow side by a mechanical stirring and forging action. Consequently, as the tool proceeds down the joint line it locally extrudes the material to form a solid-phase joint.
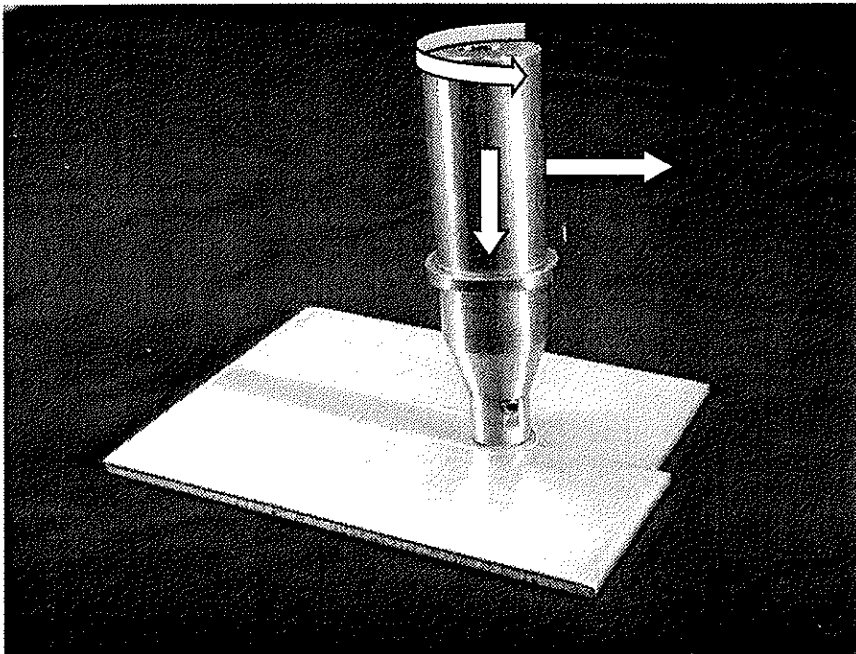
Figure 1 Basic principles of the FSW process.

1.3 Metallurgical characteristics

In general, the microstructure of a FSW joint can be divided in three different regions, illustrated in Figure 2.
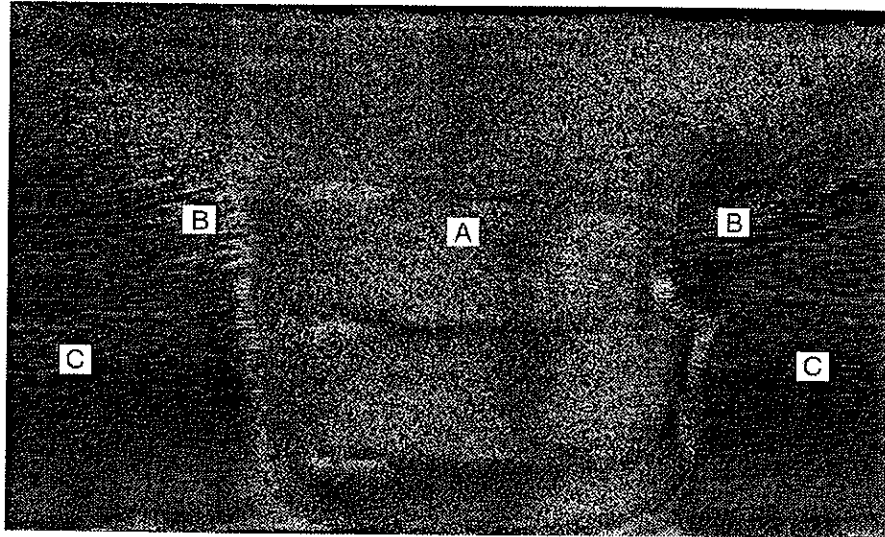
Figure 2 Overview of a friction stir aluminium weld, AA7108-T79.

A. Fully plasticied region.
B. Partly deformed region.
C. The heat affected zone.

Previous investigations carried out on conventional friction welded joints suggest that the fully platsicied region consists of a very fine subgrain structure, where the grain size is typically 3 to 6 µm /7/. This is due to a high deformation rate in the temperature range from 450-550°C, leading to dynamic recovery. The partly deformed region is a transition zone where temperature and deformation rate is lower, and hence the conditions for dynamic recovery are not reached. Outside this region the material will only respond to the imposed thermal field. The microstructure changes in the HAZ are therefore similar to those observed during conventional arc welding.

1.4 Metallurgical advantages

The main metallurgical advantage of solid state joining is that problems associated with the liquid/solid phase transformation are eliminated. The alloy composition is also preserved, and hence there is no loss of alloying elements due to evaporation. This makes it possible to recover more than 90% of the base metal mechanical properties after post weld heat treatment, as shown in Table 1.

Table 1 Typical mechanical properties of base materials and FSW joints /8/.

Alloy	Base material		FSW joints		Joint efficiency
	$Rp_{0.2}$	A5	$Rp_{0.2}$	A5	R_{mw}/R_{mBM}
AA6063.80-T5 as-welded	239	12.8	118	4-8	0.71
AA6082.50-T5 as-welded	247	8.9	115	5-8	0.74
AA6082.50-T5 post-welded			260	5-8	0.9
AA7108.50-T79 post-welded NA 6days	348	13.5	220	9-12	0.86
AA7108.50-T79 post-welded NA 45days			266	10-12	0.93

Moreover, the fine grained weld microstructure leads to joints showing better fatigue performance. Investigations of the fatigue properties of 5 mm plates of AA6082-T4 material show that the fatigue strength of FSW butt welds is typically 50% of the base material, compared to 32% for conventional MIG butt welds. In the former case the crack initiation starts always from interior defects, which means that the fatigue strength depends on the quality of the weld. Figure 3 shows some test results obtained for different AA6082-T4 weldments /9/.
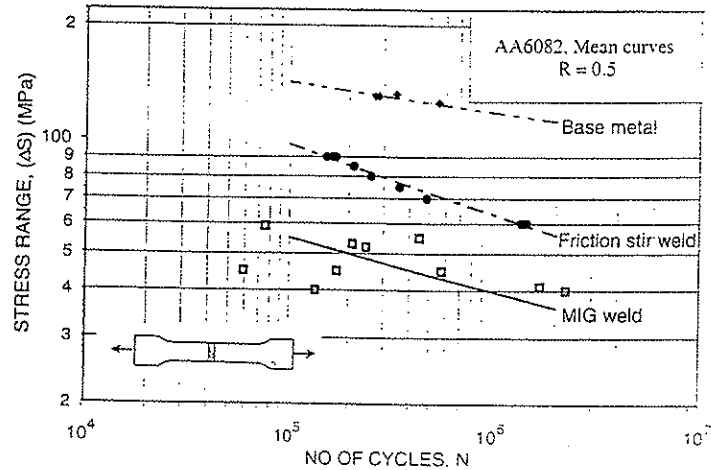
Figure 3 Fatigue data and mean life S-N curves for different AA6082-T4 weldments /9/.

1.5 Models for the HAZ microstructure evolution

In the following, relevant models for the HAZ microstructure evolution during welding of Al-Mg-Si and Al-Zn-Mg extrusions will be reviewed. However, first it is appropriate to start with a brief introduction to the physical metallurgy of age hardening aluminium alloys.

1.5.1 Age hardening aluminium alloys

In general, the strengthening effect of the age hardening alloys is related to the semicoherent transition structures reducing dislocation mobility provided by the presence of lattice strains and precipitate particles /10/. Further progress of the precipitation reaction produces growth of the transition phase particles, with an accompaning increase in coherency strains, until the strength of the interfacial bond is exceeded and coherency disappears. This frequently coincides with a change in the structure of the precipitate from the transition to the equilibrium phase. Strength progressively decreases with growth of equilibrium phase particles due to an increase in the interparticle spacing /10/.

The symbols and units used throughout the chapter are defined in Appendix 1.1.

1.5.2 Welding of Al-Mg-Si alloys

Broadly speaking, the ageing sequence within the 6xxx aluminium alloy series can be summarised as follows /11,12,13,14/:

Supersaturated solid solution $\Rightarrow$ GP zones $\Rightarrow$ β'' (Mg$_2$Si) needles $\Rightarrow$ β'(Mg$_2$Si) rods $\Rightarrow$ β equilibrium

Due to the low thermal stability of the hardening β''-precipitates reversion will occur to an increasing extend in the peak temperature range from 250 to 500°C during welding of AA6082-T6 alloys, as shown in Figure 4.
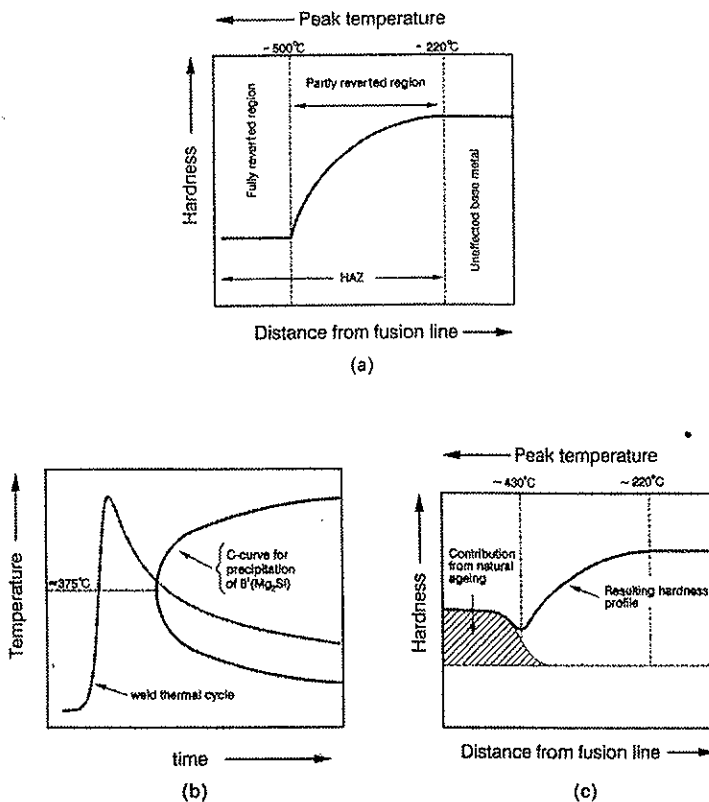
Figure 4 Schematic diagrams showing the sequence of reactions occurring in the HAZ of 6082-T6 aluminium welds; (a)Hardness distribution following β''(Mg$_2$Si) dissolution.; (b) Precipitation of β''(Mg$_2$Si) at dispersoids during the welding cycle (c) Hardness distribution after prolonged room temperature ageing /17/.

1.5.2.1 Kinetics of particle dissolution

For rod shaped particles embedded in a finite, depleted matrix, the rate of dissolution can be calculated by numerical methods from a simplified 2-D diffusion model /15,16/. Assuming that the precipitates are mainly aligned in one crystallographic direction, it is reasonable to approximate their distribution by that of a face-centred cubic (close-packet) space lattice, as shown in Figure 5a. If planes are placed midway between the nearest-neighbour particles, they enclose each particle in a separate cell. Since symmetry demands that the net flux of solute through the cell boundaries is zero, an inscribed cylinder whose volume is equivalent to that of the hexagonal cell approximately defines the dissolution zone.

It follows from Figure 5(b) that the rate of reversion can be reported as:

$$f/f_0 = (r/r_0)^2 \qquad (1)$$

where r_0 is the initial cylinder (particle) radius.

(a)

(b)
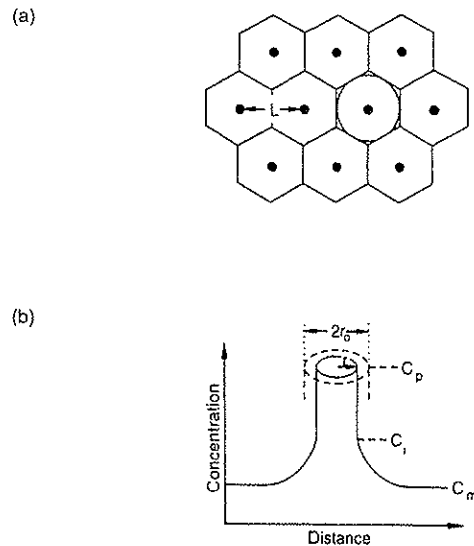
Figure 5 Simplified 2-D diffusion model for dissolution of rod-shaped particles in a finite, depleted matrix; (a) Dissolution cell geometry, (b) Particle/matrix concentration profile (moving boundary) /17/.

For a specific alloy, the ratio between r_0 and l (the mean interparticle spacing) can be calculated from a simple mass balance, assuming that all solute is tied-up in precipitates. Taking this ratio equal to 0.06 for rod-shaped precipitates in diluted alloys/18/, the kinetics of particle dissolution during isothermal heat treatment have been examined for a wide range of operational conditions. These results are presented in a general form in Figure 6 by the use of the following groups of dimensionless parameters:

$$\text{Dimensionless time } \tau = \frac{D_m t}{(r_0)^2} \qquad (2)$$

$$\text{Dimensionless supersaturation } \alpha = \frac{C_i - C_m}{C_p - C_i} \qquad (3)$$

The data in Figure 6 suggest that the reaction kinetics during the initial stage of the process are approximately described by the relation:

$$f/f_0 = 1 - c_2 \alpha(\tau)^{n_1} \qquad (4)$$

where c_2 is a kinetic constant and n_1 is a time exponent (assumed constant and equal to 0.5 under the prevailing circumstances).

The rate of particle dissolution will gradually decline with increasing values of τ as a result of impingement of diffusion fields from neighbouring precipitates, which reduces α. In practice, this is seen as a continuos decrease in the slope of the f/f_0-τ curves in Figure 6 ($n_1 < 0.5$). In such cases equation (4) will only be valid within small increments of τ.
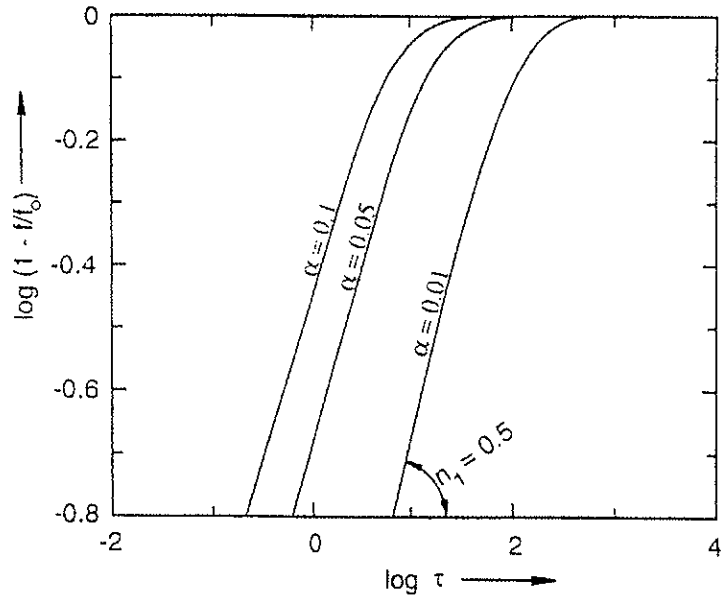
Figure 6 Dissolution kinetics of rod-shaped particles in a finite, depleted matrix. Data from Myhr and Grong /18/.

Myhr and Grong /18/ have shown how this model can be applied to a specific alloy system. From equation (4) we have:

$$f/f_0 = 1 - c_2 \alpha(\tau)^{n_1} = 1 - c_2 \left[\frac{C_i - C_m}{C_p - C_i} \right]\left[\frac{D_m t}{r_0^2} \right]^{n_1} \qquad (5)$$

where $n_1 \leq 0.5$.

This equation can further be simplified if we assume that $C_i >> C_m$ and $C_p >> C_i$:

$$f/f_0 = 1 - c_2 \frac{C_i}{C_p}\left[\frac{D_m t}{r_0^2} \right]^{n_1} \qquad (6)$$

For isothermal heat treatment at a chosen reference temperature (T_{r_1}), the rate of particle dissolution is determined by the retention time t_{r_1}. Let $t_{r_1}^*$ denote the

maximum hold time requried for complete dissolution of the precipitates. It follows that equation (6) can be written in a general form by normalising t_{r_1} with respect to $t_{r_1}^*$. The parameter $t_{r_1}^*$ is obtained by setting $f/f_0=0$:

$$t_{r_1}^* = c_3 \left[D_m \left(T_{r_1} \right) \right]^{-1} \left[C_i \left(T_{r_1} \right) \right]^{-1/n_1} \qquad (7)$$

where c_3 is a new kinetic constant.

If heat treatment is carried out at a different temperature $(T \neq T_{r_1})$, the maximum hold time t_1^* is simply given by:

$$t_1^* = t_{r_1}^* \frac{D_m \left(T_{r_1} \right)}{D_m (T)} \left[\frac{C_i \left(T_{r_1} \right)}{C_i (T)} \right]^{-1/n_1} \qquad (8)$$

By inserting the approximate expression for C_i and D_m into equation (8), and rearranging equation (6), we obtain:

$$t_1^* = t_{r_1}^* \exp \left[\left(\frac{Q_{app}'}{n_1 R} + \frac{Q_s}{R} \right) \left(\frac{1}{T} - \frac{1}{T_{r_1}} \right) \right] \qquad (9)$$

and

$$f/f_0 = 1 - \left[t/t_1^* \right]^{n_1} \qquad (10)$$

where Q'_{app} is the apparent (metastable) solvus boundary enthalpy and Q_s is the activation energy for diffusion of the less mobile constitutive atom of the precipitates.

Equations (9) and (10) exploit some good modelling techniques. For example, the use of a dimensionless time eliminates an unknown kinetic constant which premultiplies t and t_1^* in the derivation of equation (10). Moreover, by raising the dimensionless time to a power n_1 means that the premultiplying constant, here unity, is independent of the value of n_1, and is itself also dimensionless. Finally, the form of equation (9) eliminates further unknown kinetic constants, and may readily be calibrated using an experimental time $t_{r_1}^*$ at a reference temperature.

Figure 7 shows the variation in f/f_0 with time (on log axes), for a range of isothermal experiments carried out on 6082-T6 aluminium alloys, using hardness (or electrical conductivity) measurements to evaluate f/f_0, /18/. The curve (equation (10)) extrapolates back to a slope of 0.5 (the exponent n_l) for the case of the early stages of dissolution before impingement of diffusion fields. The exponent n_l is seen to fall to lower values when the proportion dissolved is higher, in agreement with theoretical curves in Figure 6.
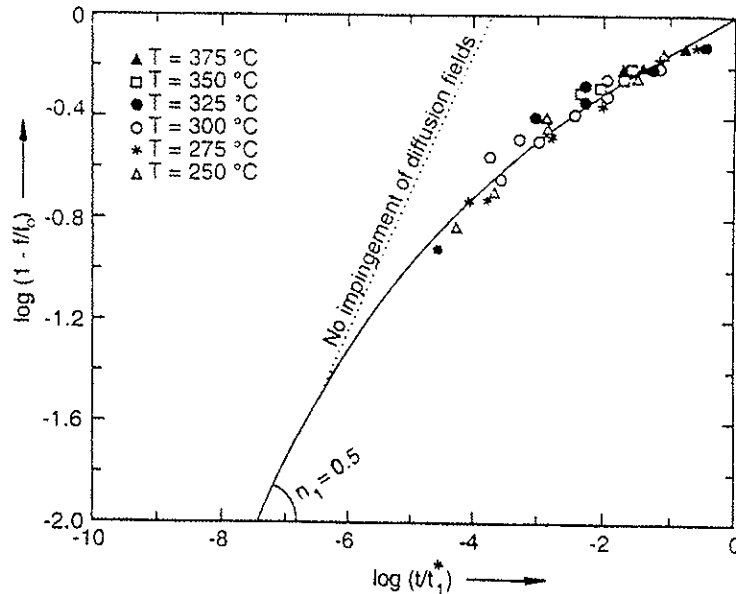
Figure 7 'Master-curve' for dissolution of hardening β''(Mg_2Si)-precipitates in 6082-T6 aluminium alloys. Data from Myhr and Grong /18/.

1.5.2.2 Strength loss following particle dissolution

Due to the lack of experimental evidence of coherency strains around β''(Mg_2Si)-precipitates in Al-Mg-Si alloys, /19/ it has been suggested that the increased resistance to dislocation motion accompanying the presence of these structures arises from the high energy required to break Mg-Si bonds in the particles as dislocations shear through them. Assuming that this strengthening effect is associated with order hardening, the net precipitation strength increment, $\Delta\sigma_p$, can be calculated from the equation originally derived by Kelly and Nicholson /20/:

$$\Delta\sigma_p = \frac{\gamma_i}{b} f = c_3 f \qquad (11)$$

where γ_i is the internal interface (or antiphase) boundary energy, b is the Burgers vector, f is the particle volume fraction and c_3 is a kinetic constant.

By introducing the relative particle volume fraction, f/f_0, we obtain:

$$\Delta\sigma_p = c_4 f/f_0 \qquad (12)$$

where f_0 is the initial volume fraction of $\beta''(Mg_2Si)$-precipitates in the alloy, and c_4 is a new kinetic constant (equal to $c_3 f_0$).

It is evident from equation (12) that $\Delta\sigma_p = \Delta\sigma_p(\max) = c_4$ when $f/f_0 = 1$. Hence, this equation can be rewritten as:

$$\alpha_1 = \frac{\sigma - \sigma_{\min}}{\sigma_{\max} - \sigma_{\min}} = \frac{\Delta\sigma_p}{\Delta\sigma_p(\max)} = f/f_0 \qquad (13)$$

Here σ_{min} denotes the intrinsic matrix strength after complete particle dissolution, while σ_{max} is the original base metal strength in the artificially aged (T6) condition.

In practice, exact measurements of the volume fraction and size distribution of hardening β''-precipitates remaining in the matrix after welding involves the use of time consuming high-resolution electron microscopy. An indirect method based on hardness measurements, described in /18/, is considered more feasible, assuming that a linear relationship exists between yield strength and hardness. According to this procedure, the relative volume fraction of particles, f/f_0, can be related to a dimensionless strength parameter α_1 as follows:

$$\alpha_1 = \frac{HV - HV_{\min}}{HV_{\max} - HV_{\min}} = \frac{f}{f_0} \qquad (14)$$

where HV_{max} and HV_{min} refer to the hardness in the temper and fully reverted condition, respectively.

1.5.2.3 Strength recovery during natural ageing

In general, the fraction of hardening precipitates which form during natural ageing (i.e. ageing at room temperature) depends on the amount of remnant solute present in the matrix material after cooling of the weld. By considering the form of the C-curve for precipitation of essentially non-hardening β'(Mg$_2$Si)-particles at dispersoids during the weld cooling cycle, Myhr and Grong /18/ arrived at the following relationship for f^*/f_0, where f^* is the volume fraction of hardening precipitates which form during natural ageing:

$$\frac{f^*}{f_0} = \Phi\left[(1 - X_C)^{I_1} - \alpha_1\right]^2 \tag{15}$$

The integral in (15) is defined as:

$$I_1 = \left[\int dt/t_2^*\right]^{n_2} \tag{16}$$

Moreover, the parameter Φ is a proportionality constant equal to 0.56, while t_2^* denotes the time taken to precipitate a certain fraction ($X=X_c$) of β'at an arbitrary temperature T. The variation of t_2^* with temperature is given by the following equation /18/:

$$t_2^* = t_{r2}^* \exp\left[\frac{A_0}{R}\left(\frac{1}{T(T_{eq}-T)^2} - \frac{1}{T_r(T_{eq}^*-T_r)^2}\right) + \frac{Q_d}{R}\left(\frac{1}{T} - \frac{1}{T_r}\right)\right] \tag{17}$$

where t_{r2}^* is the critical hold time required to precipitate a certain fraction of β'(Mg$_2$Si) at T_r, T_s is the phase boundary solvus temperature, A_0 is a material constant related to the nucleation potency of the dispersoids with respect to β'(Mg$_2$Si), and Q_d is the activation energy for diffusion of magnesium in aluminium.

A combination of equation (13) and (15) then leads to the following expression for the net precipitation increment following natural ageing, α_2 can therefore be written as:

$$\alpha_2 = \frac{HV - HV_{min}}{HV_{max} - HV_{min}} = \frac{f^*}{f_0} \tag{18}$$

1.5.2.4 Coupling of models

Since the resulting strength level in the partly reversed region depends on the interplay between two competing processes (i.e., dissolution and reprecipitation), it is convenient to define the "boundary" between the two models on the basis of the intersection point in Figure 8 where $\alpha_1=\alpha_2$, i.e.:

$$HV=HV_{min}+(HV_{max}-HV_{min})\ \alpha_2 \qquad \text{when } \alpha_2 > \alpha_1 \qquad\qquad (19)$$

and

$$HV=HV_{min}+(HV_{max}-HV_{min})\ \alpha_1 \qquad \text{when } \alpha_1 \geq \alpha_2 \qquad\qquad (20)$$

It follows that this locus also defines the minimum HAZ strength level, which is an important parameter in engineering design. This is illustrated in Figure 8
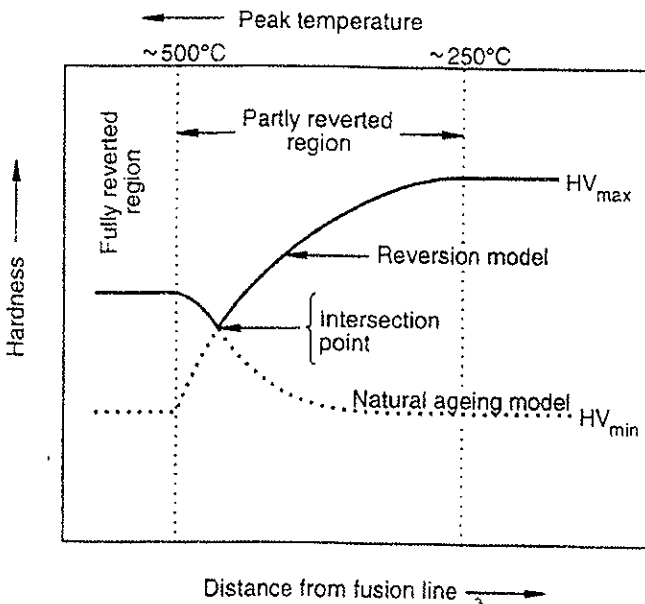
Figure 8 Coupling of reversion and natural ageing model /17/.

1.5.3 Welding of Al-Zn-Mg alloys

Information about phase relations and solubility limits within the Al-Zn-Mg system can be obtained from well-established sources /21/. The alloys of interest here are variants of the AA 7108 type, which contain Zr for control of the base metal subgrain structure. The important equilibrium phase within this alloy system are $Mg_3(Zn,Al)_5$ (the so-called T-phase) and $Mg(Zn,Al,Cu)_2$ (the so-called η phase), the latter being the most dominant one.

1.5.3.1 Stable precipitates

Figure 9 (a) shows the calculated solvus boundary for the equilibrium η phase in the AA 7108.70 variant, where the matrix concentration is assumed to follow the stoichiometric line for decomposition of pure $MgZn_2$ in Figure 9 (b). It is evident that the Al-Zn-Mg alloy system is characterised by a large solid solubility of zinc and magnesium. The eutectic temperature T_{eut} is first reached when the matrix concentration exceeds 15 wt% Zn and 3 wt% Mg, respectively. Mathematically, the variation in the Zn concentration with temperature can be described as:

$$C = C^* \exp\left(-\frac{\Delta H_{app}}{RT}\right)$$

(21)

where ΔH_{app} is the apparent solvus boundary enthalpy for the reversible dissolution/precipitation reaction. The other symbols have their usual meaning and are defined in Appendix 1.1.

Based on the above relationship it is possible to calculate the equilibrium solvus temperature T_{eq} as a function of composition. By substituting the appropriate values for C^* and ΔH_{app} into equation (21) with respect to T, we obtain:

$$T_{eq}(°C) \approx \frac{-32000}{R\ln(C/2590)} - 273$$

(22)

(a)
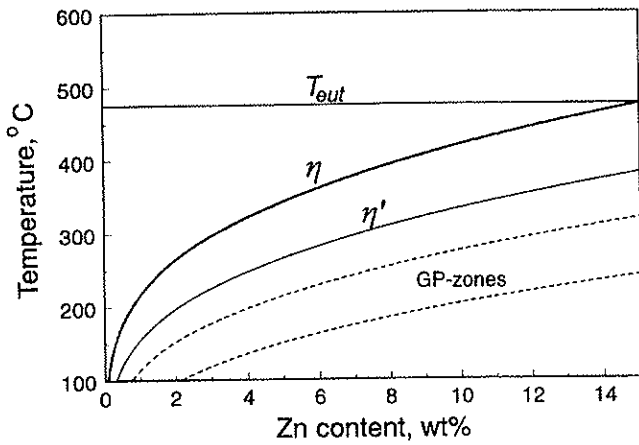
(b)
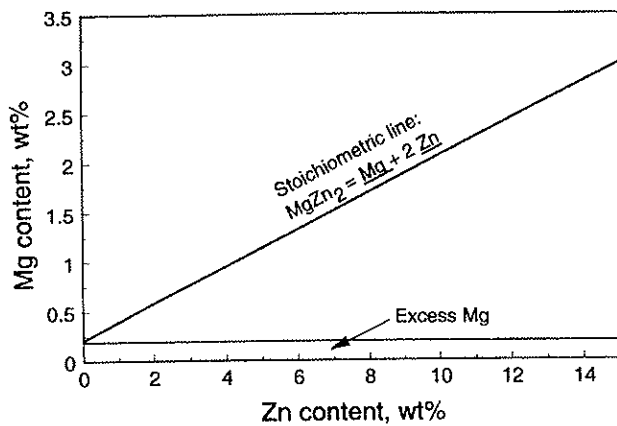
Figure 9 Phase relations within the AA 7108.70 alloy system; (a) Predicted stable and metastable solvus boundaries, (b) Resulting change in matrix concentrations during phase decomposition /22/.

1.5.3.2 Metastable precipitates

In its simplest form, the precipitation sequence in the Al-Zn-Mg alloy system during ageing can be written as /23/:

$$ss \rightarrow GP\text{-}zones \rightarrow \eta' \rightarrow \eta \qquad\qquad (23)$$

The GP-zones typically form at low and medium ageing temperatures, and are the dominant hardening precipitates at room temperature and up to, say, 120-130 °C. In the T6 temper condition the observed peak strength can mainly be attributed to the η' phase, which tend to nucleate and grow from existing GP-zones during two step ageing /23/. From a thermodynamic standpoint these hardening precipitates will be less stable than the equilibrium η phase at elevated temperatures. Their dissolution temperature can, in turn, be estimated by considering the influence of particle curvature on the solid solubility through the Gibbs-Thompson equation /17/. This method has shown to work well for different aluminium alloys within the 6XXX and 2XXX series, where the results can be checked against outputs from Thermo-Calc™ and electrical conductivity measurements /24/. According to the assumptions, the metastable solvus temperature T_{eq} is related to the real equilibrium temperature T_{eq} trough the following equation /17/:

$$T_{eq} = T_{eq} \frac{\Delta H_{app} - \Omega}{\Delta H_{app}} \qquad (24)$$

In equation (24) Ω denotes the contribution of the interface curvature to the reaction ethalpy, and is defined as:

$$\Omega = \frac{2\gamma V_m}{r_0} \qquad (25)$$

where γ is the particle/matrix interface anergy, V_m is the molar volume of the precipitates, and r_0 is the initial (mean) particle radius. From this we see that large solubility differences can arise for particles in the range from $r_0 = 1$ to 10 nm.

By combining equation (22) with equation (24), it is possible to express T_{eq} solely in terms of measurable (or known) quantities:

$$T_{eq}(°C) \approx \left(\frac{32000 - \Omega}{32000} \right)\left(\frac{-32000}{R \ln(C/2590)} \right) - 273 \qquad (26)$$

Equation (26) provides a means for estimating metastable solvus boundaries for the different hardening phases in commercial Al-Zn-Mg alloys. Examples of computed solvus boundaries for the GP-zones and the η' phase are included in Figure 9 (a). In both cases it is assumed that a single value of Ω holds for each type of precipitates rather than allowing for spatial variations in the particle size of a given type. During welding the reduced thermal stability of these hardening phases will lead to the formation of a wide soft zone adjacent to the fusion boundary because of reactions occurring within the low peak temperature region of the weld.

1.5.3.3 Kinetics of particle dissolution

If the transient part of the diffusion field around the particles is neglected, the dissolution rate (here defined negative) can be described by the following differential equation /25/:

$$\frac{dr}{dt} = -\frac{C_i - C_m}{C_p - C_i} \frac{D}{r} \qquad (27)$$

where C_i is the equilibrium concentration at the particle/matrix interface (given by equation (26)), C_m is the mean solute concentration in the matrix, C_p is the solute concentration within the particle, D is the diffusion coefficient, and r is the particle radius. This evolution equation is essentially the same as the one used for diffusion-controlled growth /26/, although growth and dissolution, from a kinetic standpoint, cannot be regarded as conjugate processes.

It follows that the particles will start to dissolve when C_i exceeds C_m. The mean matrix concentration will, in turn, depend on the volume fraction of hardening particles f in the material. If the particle distribution in the dissolution model is represented by a monodispersive system of spheres, f will fall from its initial value f_0 as:

$$f = f_0 \left(\frac{r}{r_0} \right)^3 \qquad (28)$$

The mean concentration in the matrix can then be obtained from the lever rule /17/:

$$C_m = C_0 \left(1 - \frac{f_0 (r/r_0)^3}{f_m} \right) \qquad \qquad (29)$$

where C_0 is the total zinc content in the alloy, and f_m is the maximum possible volume fraction of precipitates that can form in the alloy at absolute zero assuming stoichiometric compound formation.

Based on equation (27) and (29) it is possible to quantify the extend of particle dissolution that occurs during welding Al-Zn-Mg alloys for different starting conditions. Because of the direct coupling between the particle radius r and the matrix concentration C_m, the differential evolution equation is not separable. Hence, a closed isokinetic solution based on the Scheil formulation can not be achieved /27/, which means that that the integration must be carried out stepwise with time over the actual thermal cycle. Note that if C_m exceeds C_i the sign of the derivative dr/dt changes from negative to positive. This occurs typically towards the end of the cooling cycle because of accumulation of solute in the adjacent matrix following reversion at higher temperatures, and defines the onset of the transient growth period.

1.5.3.4 Strength loss following particle dissolution

The next step is to develop a model for the precipitation strength loss in Al-Zn-Mg weldments. For simplicity, particle shearing is assumed to be the dominating strengthening mechanism both in the base material and within the weld HAZ. Under such conditions, the net precipitation strength increment after an arbitrary reheating cycle is given as /28/:

$$\Delta \sigma_p = k_1 \left((f)^{1/2} (r)^{1/2} \right) \qquad \qquad (30)$$

where k_1 is a constant.

Similarly, for the unaffected base material, where $f = f_0$ and $r = r_0$, we may write by analogy:

$$\Delta \sigma_{p,m} = k_1 \left((f_0)^{1/2} (r_0)^{1/2} \right) \qquad \qquad (31)$$

from which

$$\alpha_1 = \frac{S_1 - S_{\min}^0}{S_{max}^0 - S_{\min}^0} = \left(\frac{\Delta\sigma_p}{\Delta\sigma_{p,m}}\right) = \left(\frac{f}{f_0}\right)^{1/2}\left(\frac{r}{r_0}\right)^{1/2} = \left(\frac{f}{f_0}\right)^{2/3} = \left(\frac{r}{r_0}\right)^2 \qquad (32)$$

In the following α_1 is referred to as the dimensionless strength parameter, while S_1 denotes a specific mechanical property such as hardness (HV) and strength. The maximum and minimum values S_{max}^0 and $S_{\min}^0$ represents the hardness or strength in the aged hardened and fully reverted condition, respectively.

1.5.3.5 Contribution from natural ageing

In Al-Zn-Mg weldments most of the strength will be recovered during subsequent natural ageing. From a kinetic standpoint natural ageing is an extremely difficult process to model because of the interaction between quenched-in vacancies and the GP-zone formation. However, purely on deterministic grounds the relationship between the matrix solute content C and the maximum fraction of hardening precipitates that forms during natural ageing Δf_p can be obtained from a simple 3-D kinetic (cell) model, assuming site saturation and that reaction is interface-controlled /17,18/. Since we are only interested in the terminal value of r after a fixed holding time at room temperature, the expression for r reduces to /17,18/:

$$r = k_2\left(C_m - C_i\right) \approx k_2\left(C_m - C_m^0\right) \qquad (33)$$

where k_2 is a constant, and C_m^0 is the matrix solute content in the stabilised base material.

If the distribution of the precipitates is approximated by that of a regular 3-D space lattice, the resulting volume fraction is simply given as /17,18/:

$$\Delta f_p = k_3 r^3 = k_4\left(C_m - C_m^0\right)^3 \qquad (34)$$

This leads to the following expression for the net precipitation strength increment during natural ageing:

$$S_2 - S_1 = k_5 \left(C_m - C_m^0 \right)^2 \qquad \qquad (35)$$

Within the fully reverted region, where the matrix concentration C_m reaches C_0, the precipitation is highest. Here the different parameters entering the strength model attain their limiting values, i.e. $S_2 = S_{max}$, $S_1 = S_{min}^0$, $r = r_m$ and $\Delta f_p = \Delta f_{p,m}$ from which:

$$S_{max} - S_{min}^0 = k_5 \left(C_0 - C_m^0 \right)^2 \qquad (36)$$

A combination of equation (35) and (36) then gives:

$$\alpha_2 = \frac{S_1 - S_2}{S_{max} - S_{min}^0} = \left(\frac{\Delta \sigma_p}{\Delta \sigma_{p,m}} \right) = \left(\frac{f_p}{f_{p,m}} \right)^{1/2} \left(\frac{r}{r_m} \right)^{1/2} = \left(\frac{C_m - C_m^0}{C_0 - C_m^0} \right)^2 \qquad (37)$$

Equation (37) predicts that the resulting HAZ hardness or strength following natural ageing will drop from $S_2 = S_{max}$ within the fully reverted region (where $C_m = C_0$) to some lower value $S_2 < S_{max}$ within the partly reverted HAZ because of the reduced solute content available for GP-zone formation. The increase in S_{max} with time can, in turn, be read from an experimental ageing curve of the type shown in Figure 10.
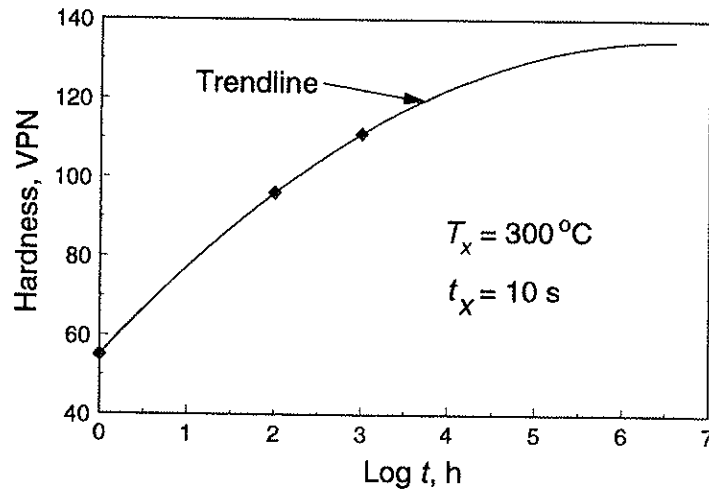
Figure 10 Experimental natural ageing curve for fully reverted base material /22/.

An important consequence of equation (37) is that the ultimate HAZ strength level depends on the interplay between two competing processes that occur during and after welding, respectively, i.e. dissolution and re-precipitation. Mathematically, this relationship can be expressed as:

$$S_2 = S_{min}^0 + \alpha_1 \left(S_{max}^0 - S_{min}^0\right) + \left(S_{max} - S_{min}^0\right)\left(\frac{C_m - C_m^0}{C_0 - C_m^0}\right) \qquad (38)$$

As shown in Figure 11, the combined model also defines the locus of the minimum HAZ strength level, which is an important parameter in engineering design.
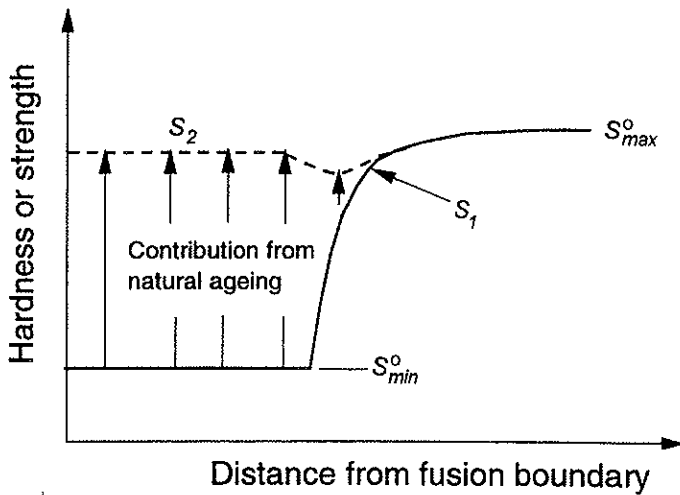
Figure 11 Schematic diagram showing the coupling between the different strength models /22/.

1.6 Summary of current knowledge

The following main conclusions can be drawn from the present literature review:

- In general, the HAZ hardness distribution following welding of age hardening aluminium alloys depends on the interplay between competing processes, i.e. dissolution and reprecipitation. These reactions can be captured mathematically by means of process modelling techniques.

- Because of the analytical origin of the existing microstructure models, they can easily be coupled with an appropriate heat flow model for FSW and implemented in a dedicated numerical code. The combination of a microstructure model with a heat flow model, provides a powerful tool for optimisation of process parameters and joint properties during FSW of age hardening aluminium alloys, and an illustration of this will be given in the present thesis.

1.7 REFERENCES

1. M.F. Ashby and D.R.H. Jones: Engineering materials 2, Pergamon Press, 1988.

2. Thomas W M et al "Friction Stir Butt Welding", International Patent Application No. PCT/GB92/02203 and GB Patent Application No.9125978.8, 6 Dec 1991.

3. C.J. Dawes and W.M. Thomas: Welding Journal, March 1996.

4. O.T. Midling, The Aluminium Conference, 24-25. September 1997, Essen, Germany.

5. A.O. Kluken and B. Bjørneklett, Welding Journal 76, 1997, 39-40.

6. D.H. Bratland, Ø. Grong, H.R. Shercliff, O.R. Myhr and S. Tjøtta:'Modelling of Precipitation Reactions in Industrial Processing', Acta Metall Mater. (in press).

7. O.T. Midling, Ph.D. thesis, Norwegian Institute of Science and Technology, 1993.

8. O.T. Midling: "Friction stir sveising miljøvennlig sammenføyning av aluminiumprofiler", Sveiseaktuelt, 1.kvartal, 1996.

9. P.J. Haagensen, O.T. Midling and M, Ranes: Fatigue Performance of Friction Stir Butt Welds in a 6000 Series Aluminium Alloy, the 2nd International Conference on Surface Treatment 95, Milan, Italy, 7-9 June 1995.

10. Aluminium: Properties and Physical Metallurgy, American Society for Metals, pp.145, 1984.

11. G. Thomas: The Ageing Characteristics of Aluminium Alloys- TEM Studies of Al-Mg-Si Alloys, J. Inst. of Metals, 90, pp. 57-63, 1961/62.

12. M.H. Jacobs: The Structure of the Metastable Precipitates Formed During Ageing of an Al-Mg-Si Alloy, Phil. Mag., 26, pp. 1-13, 1972.

13. J.P. Lynch, L.M. Brown and M.H. Jacobs: Microanalysis of Age- Hardening Precipitates in Aluminium Alloys, Acta metall., 30, pp. 1389-1395, 1982.

14. H. Westengen and N. Ryum: Precipitation Reactions in an Aluminium 1 wt% Mg2Si Alloy, Z. Metallkde., 70, pp. 528-535, 1979.

15. R.A. Tanzilli and R.W. Heckel, Trans. Met. Soc. AIME 242, 2313 (1968)

16. S. Suzuki, G.C. Weatherly and D.C. Houghton, Acta Metall. 35, 341 (1987).

17. Ø. Grong: Metallurgical Modelling of Welding, Second Edition, The Institute of Materials, pp. 393, 1997.

18. O.R. Myhr and Ø. Grong: Acta Metall. Mater., 1991, 39, 2693-2702; ibid.,2703-2708.

19. J.E. Hatch (Ed.): Aluminium-Properties and Physical Metallurgy, 1984, Ohio (USA), American Society of Metals.

20. A. Kelly and R.B. Nicholson: progr. Mat. Sci., 1963, 10, 151-156.

21. H. W. L. Phillips, "Annotated Equilibrium Diagrams of Some Aluminium Alloys", 1959, London (UK), The Institute of Metals.

22. Børge Bjørneklett, Ph.D thesis, Norwegian University of Science and Technology, 1998.

23. J. E. Hatch, "Aluminum, Properties and Physical Metallurgy", 1984, Ohio (USA), American Soc. for Metals.

24. P. Òlafsson, PhD Thesis, 1997, Department of Science and Engineering, Royal Institute of Technology, Stockholm, Sweden.

25. M. J. Whelan, Met. Sci., 1969, 5, 95-97.

26. H. B. Aaron, D. Fainstein and G. R. Kotler, J. Appl. Phys. 1970, 41, 4404-4410.

27. E. Scheil: Arch. Eisenhuttenwes., 1934-1935, 8, 565-571.

28. G. E. Dieter, "Mechanical Metallurgy", 3ed Ed., 1988, New York (USA), McGraw-Hill Book Company.

Appendix 1.1 – Nomenclature

A_0	material constant related to the potency of the heterogeneous nucleation cites in actual alloy (J/mol)
α	dimensionless supersaturation
α_1, α_2	dimensionless strength parameters
b	Burgers vector (m, nm)
c_2, c_3, c_4	kinetic constants
C	concentration (wt%)
C^*	constant in equation describing the solvus boundary (wt%)
C_o	total alloy content (wt%)
C_i	particle/matrix interface concentration (wt%)
C_m	mean solute concentration in the matrix (wt%)
C_p	solute concentration within the particle (wt%)
C_m^o	matrix solute content in stabilised base material (wt%)
D	diffusion coefficient (m^{2}s^{-1})
D_m	matrix diffusion coefficient (m^{2}s^{-1})
f	volume fraction of precipitates
f_m	maximum possible volume fraction of hardening precipitates that can form at absolute zero
f_0	initial volume fraction of precipitates in base material.
f^*	volume fraction of precipitates formed during natural ageing
Δf_p	fraction of hardening precipitates which forms during natural ageing
$\Delta f_{p,m}$	maximum fraction of hardening precipitates which forms during natural ageing
HV_{max}	hardness in the temper condition (VPN)
HV_{min}	hardness in the fully reverted condition (VPN)
ΔH_{app}	apparent solvus boundary enthalpy (J mol^{-1})
I_1	kinetic strength of thermal cycle
$k_1..k_5$	constants in strength models (variable units)
n_1	time exponent
Q_{app}	apparent solvus boundary enthalpy (J/mol)
Q_d	activation energy for diffusion of Mg in Al(J/mol)
Q_s	metastable solvus boundary enthalpy (J/mol)
R	universal gas constant (8.314 J/mol K)
r	particle radius (m)
r_0	initial particle radius (m)

r_m	maximum size of GP-zones (m)
S_1	hardness or strength following particle dissolution (VPN or Pa)
S_2	hardness or strength following reheating and natural ageing (VPN or Pa)
S^o_{max}	hardness or strength in age hardened base material (VPN or Pa)
S_{max}	maximum hardness or strength following natural ageing (VPN or Pa)
S^o_{min}	hardness or strength in fully reverted condition (VPN or Pa)
σ_{min}	intrinsic matrix strength after complete particle dissolution (Mpa)
σ_{max}	original base metal strength in the artificially aged (T6) condition (MPa)
T	chosen reference temperature (°C, K)
T_r, T_{r_1}	chosen reference temperature (°C, K)
T_s	phase boundary solvus temperature
T_{eq}	equilibrium solvus temperature of actual alloy (°C, K)
T^*_{eq}	equilibrium solvus temperature of reference alloy (°C, K)
T'_{eq}	metastable solvus temperature (°C or K)
t	time (s)
t_{r_1}	retention time (s)
t^*_1	maximum holding time for complete dissolution (s)
t^*_2	time taken to precipitate a certain fraction, defined by the C-curve (s)
$t^*_{r_1}$	maximum hold time for complete dissolution at reference temperature (s)
t^*_{r2}	time taken to precipitate a certain fraction of β'-Mg$_2$Si at a chosen reference temperature (s)
τ	dimensionless time
X_c	fraction transformed
Φ	proportionality constant
Ω	contribution of the interface curvature to the reaction enthalpy (J mol^{-1})
$\Delta\sigma_p$	net precipitation strength increment (Pa)
$\Delta\sigma_{p,m}$	net precipitation strength increment in base material (Pa)
γ_i	internal interface boundary energy

Part II: A 2-D HEAT FLOW MODEL FOR FRICTION STIR WELDING

2.1 Introduction

The interest in friction stir welding (FSW) has gained considerable momentum over the past few years /1/. This is because the process has made it possible to implement the advantage of solid state bonding to plate and profile joints, thus leading to new product design previously not feasible /2/. In FSW the heat is generated by rotating movement of the shoulder and the pin. The frictional heating contributes to the formation of a plasticized layer of soft metal beneath the tool shoulder and about the pin. The material is then transported to the flow side of the tool due to the imposed mechanical stirring and forging action before it cools and forms a solid state joint /3/.

In order to take full advantage of the FSW process, it is necessary to understand and predict the microstructure evolution during welding. All welding techniques applied to heat treatable alloys represent local reheating of a material that has previously undergone a tight temperature control to achieve the desired mechanical properties. Hence, great attention must be given to the HAZ (heat affected zone) temperature-time pattern during welding in order to select welding parameters suitable for the given application /4,5/.

In Part II of the thesis, attempts have been made to model the temperature distribution during FSW of aluminium alloys, based on the finite difference approach. The algorithm reported here solves the differential heat flow equation for the appropriate boundary conditions in two dimensions, and provides an overall indication of the effect of process variables on the resulting temperature-time pattern. A full 3-D heat flow model for FSW is presented in Part III.

2.2 Heat flow modelling

In FSW the heat generation takes place under the tool shoulder and in the plasticized region of the weld. In the case of thin plate welding a uniform temperature can be expected throughout the plate thickness. The temperature distribution can then be described using a 2-D heat flow model. If the thermal diffusivity, λ, is assumed constant and independent of temperature the following heat flow equation applies /6/:

$$\rho c \frac{\partial T}{\partial t} = \lambda \left(\frac{\partial^2 T}{\partial x^2} + \frac{\partial^2 T}{\partial y^2} \right) + \frac{q_0}{V} \qquad (1)$$

The other symbols have their usual meaning and are defined in Appendix 2.1.

2.2.1 Analytical solutions

In the limiting case FSW may be represented by a line source model. The following two extremes are considered:

1. The instantaneous line source model.
2. The moving line source model.

2.2.1.1 The instantaneous line source model

The concept of an instantaneous heat source is widely used in the theory of heat conduction /7/. It is seen from Figure 1 that the solution is based on the assumption that the heat is released instantaneously at time $t=0$ in an infinite medium of initial temperature T_0 along a line. The material outside the heat source is assumed to extend to $r=\pm\infty$.
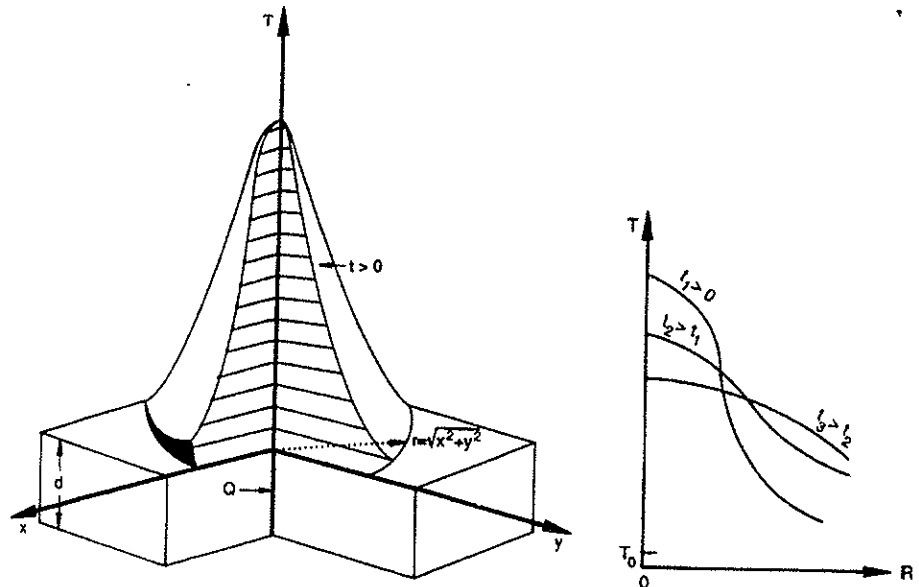
Figure 1 Schematic representation of an instantaneous line source in a wide plate /8/.

The initial and boundary conditions can be summarised as follows:

$T-T_0 = \infty$ for $t=0$ and $r=0$
$T-T_0 = 0$ for $t=0$ and $r>0$
$T-T_0 = 0$ for $0<t<\infty$ and $r=\infty$

It is easy to verify that the following solution satisfy equation (1), and the boundary conditions listed above:

$$T - T_0 = \frac{Q/d}{\rho c(4\pi at)} \exp\left(-r^2/4at\right) \qquad (2)$$

where d is the plate thickness.

This instantaneous line source solution will later be used to check the accuracy of the numerical heat flow model.

2.2.1.2 The moving line source model

As shown in Figure 2, the moving line source model considers a wide sheet of thickness d which has an initial temperature T_0. At time $t=0$ the source starts to move at a constant speed v in the positive x-direction. The rise of temperature $T-T_0$ in point P at time t is sought. According to equation (2) the elementary source $dQ=q_0 dt'$ released at position vt' will cause a small rise of temperature dT in point P at time t:
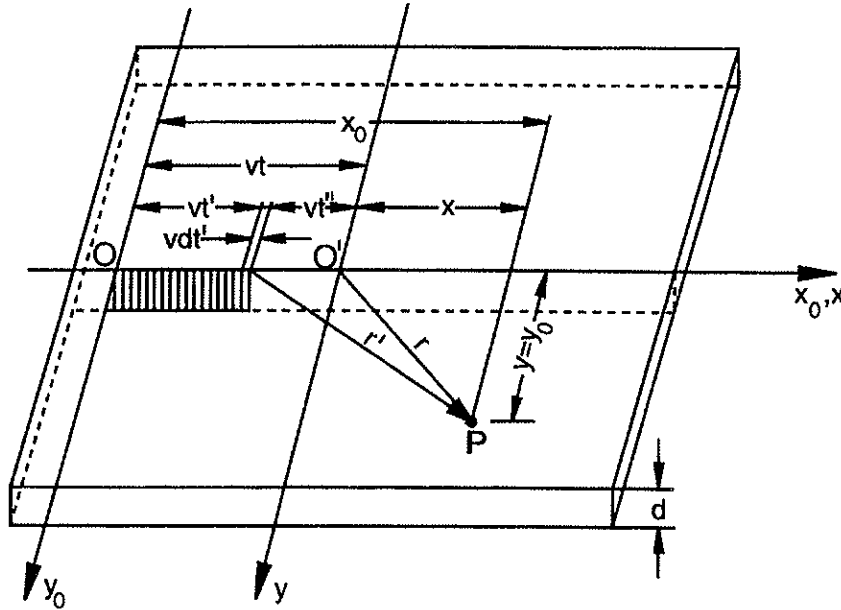
Figure 2 Moving line source in a thin sheet /8/.

$$dT = \frac{q_0 dt'}{dpc[4\pi a(t-t')]} \exp\left[-\frac{(r')^2}{4a(t-t')}\right] = \frac{q_0 dt''}{dpc(4\pi a t'')} \exp\left[-\frac{(r')^2}{4a t''}\right] \qquad (3)$$

where $t''= t - t'$ is the time available for conduction of heat over the distance $r'= \sqrt{(x_0 - vt')^2 + y_0^2}$ to point P.

If we refer the position P to that of the heat source at time t, we shall expect a solution independent of time at pseudo steady state. This is achieved by changing the co-ordinate system from O to O':

$$y=y_0, \quad x=x_0-vt, \quad x_0-vt'=x+vt-vt'=x+vt''$$

Hence we may write:

$$dT = \frac{-q_0 dt''}{d\rho c(4\pi a t'')} \exp\left[-\frac{(x+vt'')^2+y^2}{4at''}\right] \tag{4}$$

$$= \frac{-q_0 dt''}{d\rho c(4\pi a t'')} \exp\left[-\frac{vx}{2a}-\frac{r^2}{4at''}-\frac{v^2 t''}{4a}\right]$$

where $r = \sqrt{x^2 + y^2}$

For integration of all contributions from $t''=t$ $(t'=0)$ to $t''=0$ $(t'=t)$, we introduce:

$$(\sigma)^2 = \frac{v^2 r^2}{4a^2}, \quad w = \frac{v^2 t''}{4a}$$

from which:

$$t'' = \frac{4a}{v^2} w, \quad dt'' = \frac{4a}{v^2} dw, \quad \frac{r^2}{4at''} = \frac{(\sigma)^2}{4w}$$

Substituting these parameters into equation (4) give:

$$T - T_0 = \frac{q_0/d}{4\pi\lambda} \exp\left[-\frac{vx}{2a}\right]\int_{w=0}^{w} \exp\left[-\frac{(\sigma)^2}{4w}-w\right]\frac{dw}{w} \tag{5}$$

It is well known that:

$$\int_0^{\infty} \exp\left[-\frac{(\sigma)^2}{4w}-w\right]\frac{dw}{w} = 2K_0(\sigma) = 2K_0\left(\frac{vr}{2a}\right)$$

where $K_0(\sigma)$ is the modified Bessel function of the second kind and zero order. Hence, the general thin plate solution can be written as:

$$T - T_0 = \frac{q_0/d}{2\pi\lambda} \exp\left(-\frac{vx}{2a}\right) \times \left[K_0\left(\frac{vr}{2a}\right) - \frac{1}{2}\int_w \exp\left[-\frac{(\sigma)^2}{4w}-w\right]\frac{dw}{w}\right] \tag{6}$$

When w is sufficiently large (i.e. when welding has been performed over a sufficient period), we obtain the pseudo-steady state temperature distribution:

$$T - T_0 = \frac{q_0 / d}{2\pi\lambda} \exp\left(-\frac{vx}{2a}\right) K_0\left(\frac{vr}{2a}\right)$$

(7)

Equation (7) is often referred to as the Rosenthal thin plate solution. It follows that this model is applicable to all types of welding processes where heat flow in the through-thickness direction can be disregarded and loss of heat from the plate surface is negligible.

2.2.2 Numerical heat flow model

Equation (1) is the fundamental mathematical expression describing heat transfer in two dimensions. Obtaining exact analytical solutions for any boundary condition would lead to expressions containing infinite series, special functions, transcendental equations etc.. Thus for many problems of industrial importance the numerical approach is more realistic. The finite difference solution to a 2D-thermal problem consists of changing the derivatives in equation (1) with finite differences /9/:

$$\frac{df}{dx} \approx \frac{1}{k}[f(x+k) - f(x)]$$

(8)

$$\frac{d^2 f}{dx^2} \approx \frac{1}{h^2}[f(x+h) - 2f(x) + f(x-h)]$$

(9)

By using the same length h in x and y direction, we obtain the expression:

$$\frac{1}{k}[u(x,y,t+k) - u(x,y,t)] =$$

(10)

$$a\frac{1}{h^2}[u(x+h,y,t) - 2u(x,y,t) + u(x-h,y,t)] +$$

$$a\frac{1}{h^2}[u(x,y+h,t) - 2u(x,y,t) + u(x,y-h,t)]$$

If the boundary conditions are known, equation (10) can be used to obtain a solution of the given heat flow by advancing the solution step by step in the t

variable evaluating the solution $t=t_0+k$. This is obtained by rewriting equation (10) in the form:

$$u(x,y,t+k)=u(x,y,t)+a\frac{k}{h^2}\begin{bmatrix} u(x+h,y,t)+u(x-h,y,t) \\ -4u(x,y,t)+u(x,y+h,t)+u(x,y-h,t) \end{bmatrix} \quad (11)$$

The solutions obtained by the finite difference approach are only approximate because equation (11) represents the finite difference analogy of equation (1). Still if the solution is advanced using small time steps, k, the solution of the discretization equations is expected to approach the exact solution of the corresponding differential equation. The best way of testing the reliability of the solution with respect to choice of descretization, hence h and k, is to compare the output with an exact analytical solution /10/ (here the Rosenthal thin plate solution). This will be done in the subsequent sections.

2.2.2.1 Implementation in MatLab 5.2

The numerical code for FSW has been implemented in MatLab 5.2, which is a high performance language for technical computing. Typical use includes:

- Math and computation
- Algorithm development
- Modelling, simulation and prototyping
- Data analysis, exploration and visualisation
- Scientific and engineering graphics
- Application development, including graphical user interface building

Separate post-processing routines have also been developed in order to present the output from the computations graphically. A full listing of the different MatLab programmes is given in Appendix 2.2.

2.2.2.2 Finite difference model for an instantaneous line source in a thin plate

Figure 3 shows the instantaneous heat source model represented by the finite difference model. The model considers a heat input, Q [J], in the volume of one grid point at $t=0$. Adiabatic surfaces are assumed as boundary conditions,

which means that the isotherms meet the surface at a straight angel. When comparing the numerical and analytical solutions it should be noted that the latter considers a line source where the temperature in the centre reaches infinite, whereas the numerical solution considers a volume element of fixed temperature. This leads to a deviation close to the heat source, as shown in Figure 4. The five grid points involved in equation (11) for calculating the new temperature in the centre after one time step k are marked ($\bullet$).
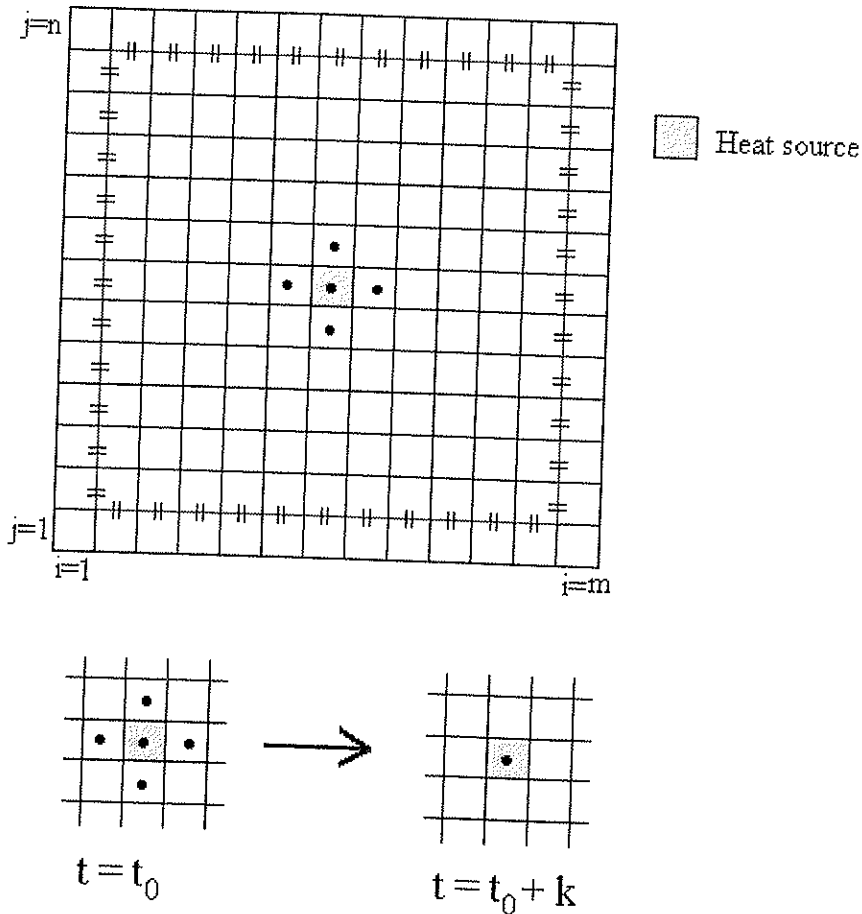
Figure 3 Finite difference model for an instantaneous line source in a thin plate.

It follows that the numerical solution converges towards the analytical solution when $h=1$ [mm] and $k<5 \cdot 10^{-4}$ [s].
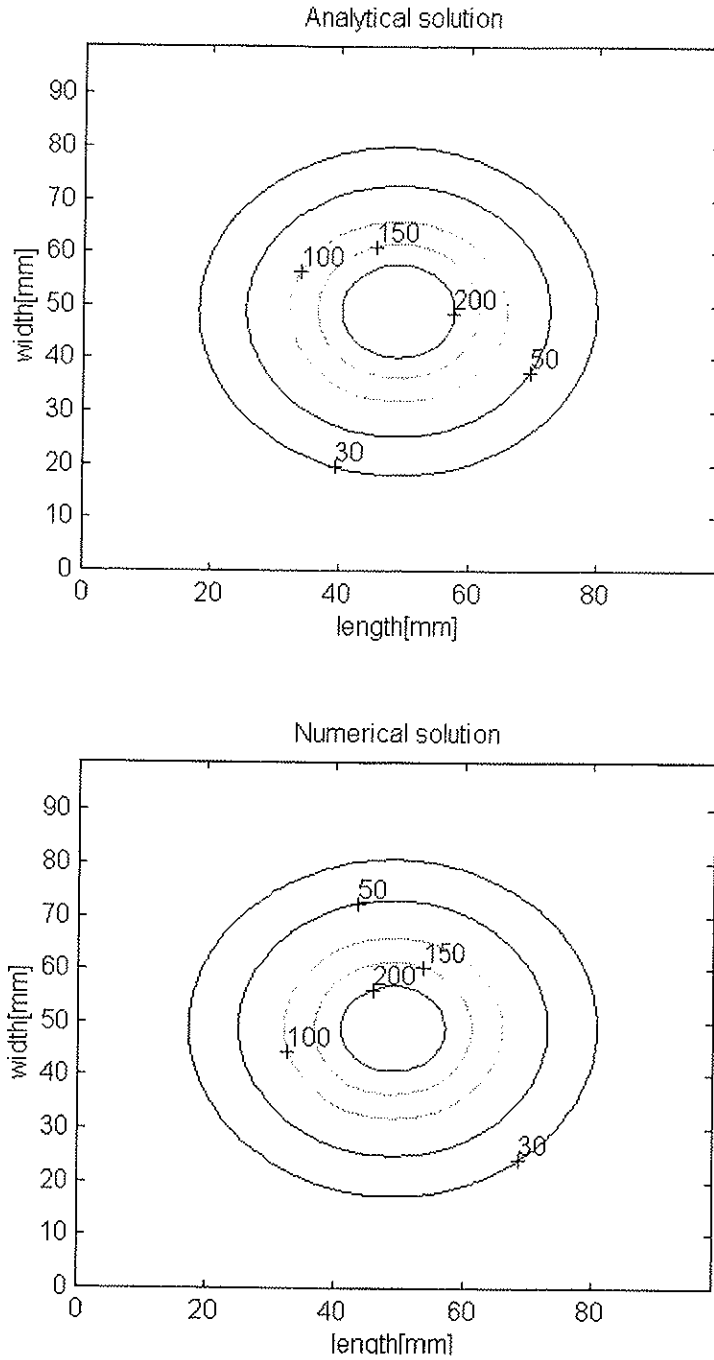
Figure 4 Comparison between analytical and numerical solutions for an instantaneous line source in a thin plate , $Q=1500$ [J], $t=1$ [s].

2.2.2.3 Finite difference model for a moving line source in a thin plate

Figure 5 shows the finite difference model for a moving line source in a thin plate. The source is assumed to move at a constant speed, v, in the positive x-direction. In order to reduce the calculation time only half the plate is considered due to symmetry. The algorithm used is the same as the line source model illustrated in Figure 3. The moving heat source is obtained by calculating the energy input for each time step k, by allowing the heat source to move one grid length h after $(h/v)/k$ interations.
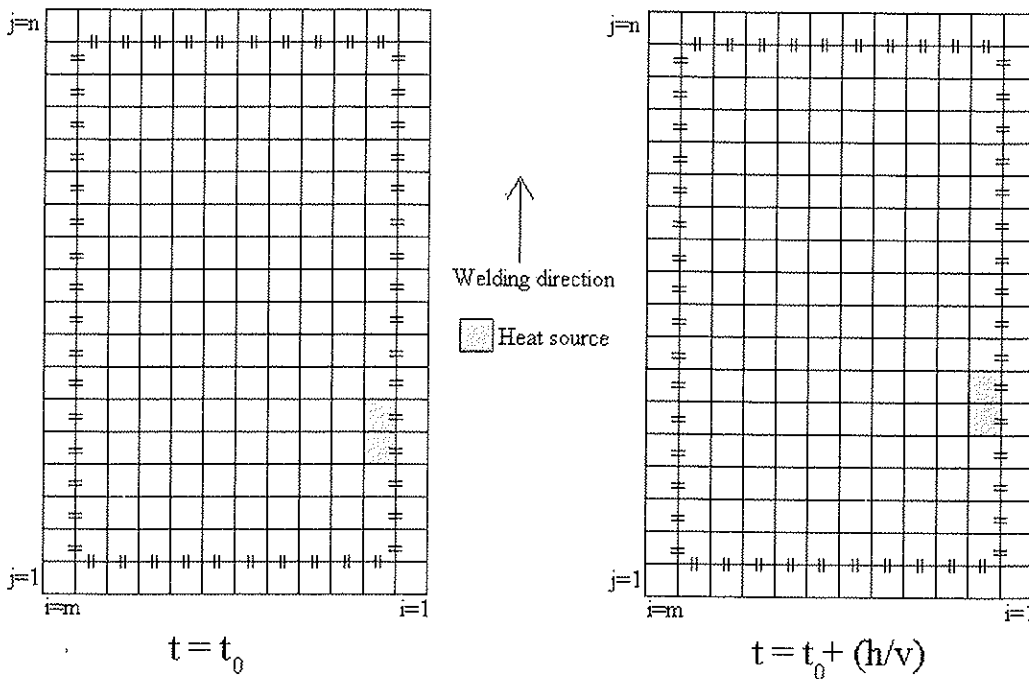
Figure 5 Finite difference model for a moving line source in a thin plate;(a) calculation after time $t=t_0$, (b) situation after time $t=t_0+(h/v)$.

Figure 6 shows that the numerical solution converges towards the analytical solution when $h=1$ and $k=5\cdot10^{-4}$ [s]. In this case the convergence criterion is that the instantaneous heat source solution converges for the same values of k and h. This is due to the fact that the moving heat source model consists of a series of elementary instantaneous heat sources.
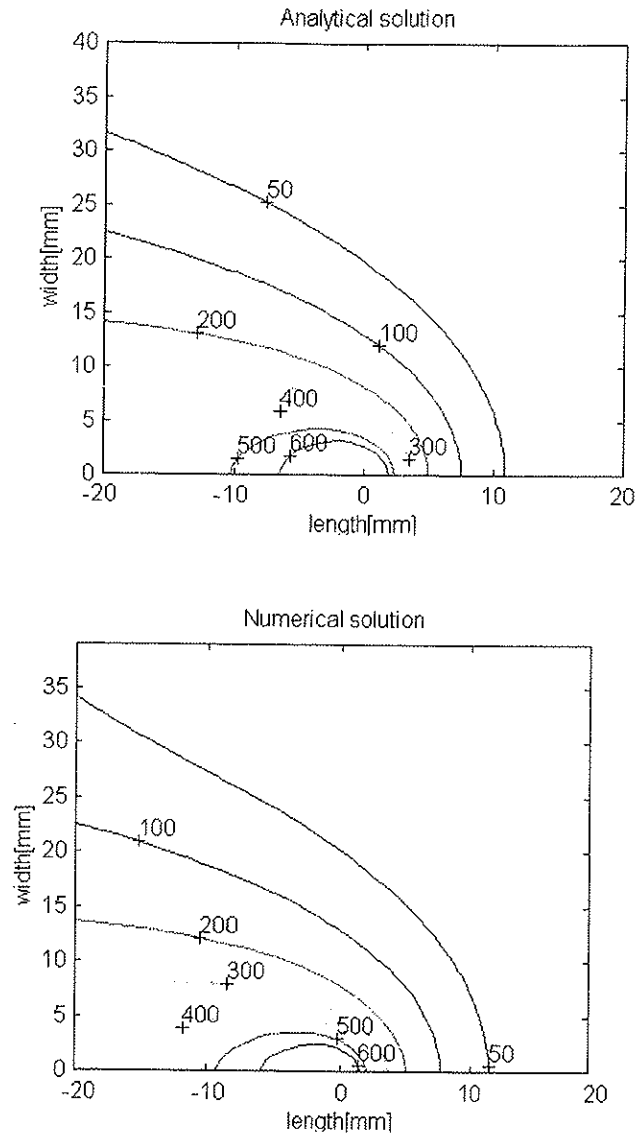
Figure 6 Comparison between the analytical and numerical solutions for a moving line source in a thin plate; (a) analytical solution (b) numerical solution. Operational conditions: q_0=1500 [W], h=1[mm], k=5·10^{-4} [s].

2.3 Heat generation

A major problem in modelling of heat flow phenomena in friction stir welding is to obtain an adequate description of the energy input. This is because the friction coefficient, μ, is changing continuously during welding from about one at the dry sliding start, towards zero when the temperature for local melting is reached at the interface /11/.

2.3.1 Constitutive equations

For the ideal case considered in Figure 7, the torque required to rotate a circular shaft relative to the plate surface under the action of an axial load is given by /12/:
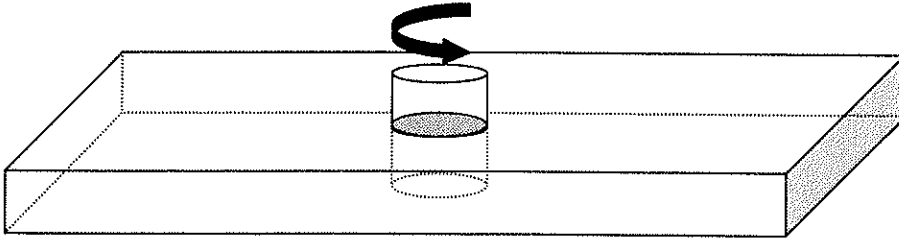
Figure 7. Rotation of the shaft relative to the plate surface (schematic).

$$M = \int_0^{M_R} dM = \int_0^{R} \mu P(r) 2\pi r^2 dr = \frac{2}{3} \mu \pi P R^3 \qquad (12)$$

where M is the interfacial torque, μ is the friction coefficient, R is the surface radius, and $P(r)$ is the pressure distribution across the interface (here assumed constant and equal to P [Pa]).

If all the shearing work at the interface is converted into frictional heat, the average heat input per unit area and time becomes /13/:

$$q_0 = \int_0^{M_R} \omega \; dM = \int_0^R \omega 2\pi\mu P r^2 dr \qquad \text{'}(\, 13 \,)$$

where q_0 is the net power (in [W]) and ω is the angular velocity (in [rad/s]).

The next step is to express the angular velocity in terms of the rotational speed N (in [rot/s]). By substituting $\omega = 2\pi N$ into equation (13), we get:

$$q_0 = \int_0^R 4\pi^2 \mu P N r^2 dr = \frac{4}{3}\pi^2 \mu P N R^3 \qquad (\, 14 \,)$$

From equation (14) it is obvious that the heat input depends both on rotational speed and the shoulder radius, leading to a non-uniform heat generation during welding. These parameters are the main process variables in FSW, since the pressure P cannot exceed the actual flow stress of the material at the operating temperature.

In order to describe the heat source in the numerical model it is more convenient to express the heat generation as a sum of individual contributions (15):

$$q_0 = \frac{4}{3}\pi^2 \mu P N \sum_{i=1}^n \left(R_i^3 - R_{i-1}^3 \right) \qquad (\, 15 \,)$$

where R_{i-1} and R_i are defined in Figure 8.

$$\sum_{i=1}^{n} q(R_i) = q_0$$
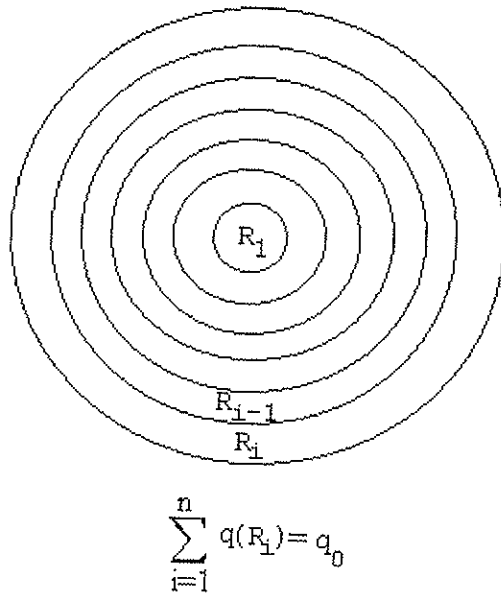
Figure 8 Subdivision of the tool shoulder into a series of volume elements of varying strength.

Hence, the energy generated from position R_{i-1} to R_i is equal to:

$$\Delta q_0 = \frac{4}{3} \pi^2 \mu P N \left(R_i^3 - R_{i-1}^3 \right) \tag{16}$$

2.3.2 Heat distribution beneath the shoulder

Based on equation (16) the heat generation in different positions can be calculated. Here the strength of each grid point is obtained by dividing the heat input with the total number of grid points involved.

As shown in Figure 9 the heat source is approximated by a fixed number of square grid points. This is a reasonable approximation, and does not lead to large inherent errors in the calculations.

Heat input under tool shoulder
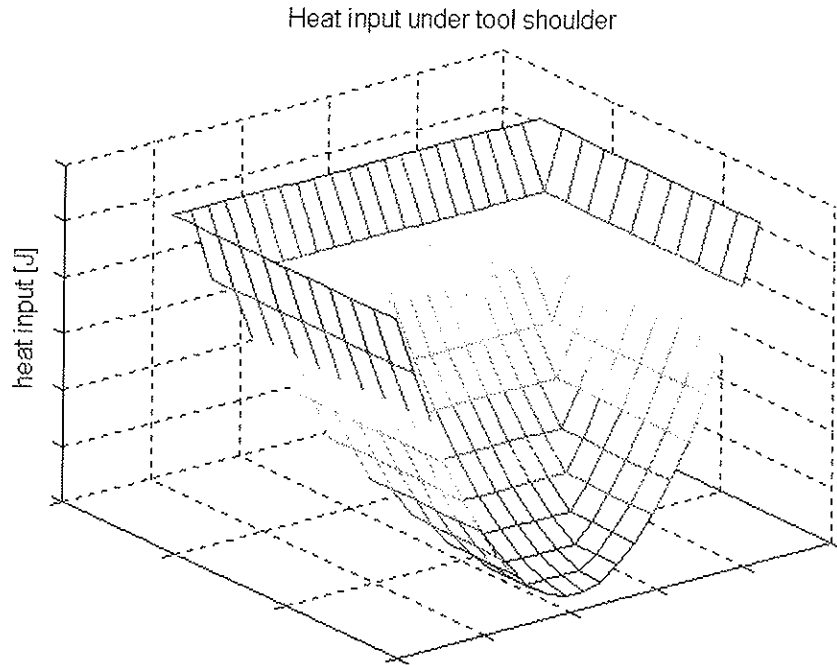
Figure 9 Schematic representation of the heat source used in the numerical model. Because of symmetry only one half of the tool is shown.

2.3.3 Restrictions in heat generation

In thermal processing of aluminium alloys it is generally accepted that local melting will occur if the material is heated above the eutectic temperature at a rate which does not allow the eutectic phase to fully dissolve into the matrix /8/. During FSW the eutectic melt will act as a lubricant and decrease the friction coefficient. Therefore, the maximum temperature under the tool shoulder should be close to the eutectic temperature of the alloy. This, in turn, limits the heat generation during welding.

2.4 Case studies

In the following a series of case studies will be presented to illustrate the basic features of the finite difference model and the specific thermal conditions existing in friction stir welding. The case studies consider but welding of 3mm thick, 200mm long and 100mm wide plates. Table 1 contains a summary of the welding parameters used in the different modelling exercises.

Table 1. Summary of welding parameters used in modelling exercises.

Case No.	T_{max}* [°C]	v [mm/s]	R [mm]	P [MPa]	rotational speed [rot/min]
case 1	550	16.7	10	40	1500
case 2	550	20	8	20	2500
case 3	550	12.5	8	20	2500
case 4	500	2.2-15.8	8	20	2500
case 5	550	20	10	20	2500

*Assumed maximum temperature beneath the tool shoulder.

2.4.1 Transient effects

Referring to Figure 10 the welding cycle can be divided into the following four stages:

- The stationary heating period: where the material beneath the shoulder is preheated to a certain temperature to accommodate the plastic deformation during welding.
- The transient heating period: where the heat starts to build up around the shoulder as the tool moves until saturation occurs.
- The pseudo steady state period: where the thermal field around the tool remains essentially constant during the welding operation.
- The post steady state period: where reflection of heat from the end plate surface leads to additional build-up of heat around the tool shoulder.

These results show that transient effects play an important role in FSW, and must be included in the heat flow analysis.
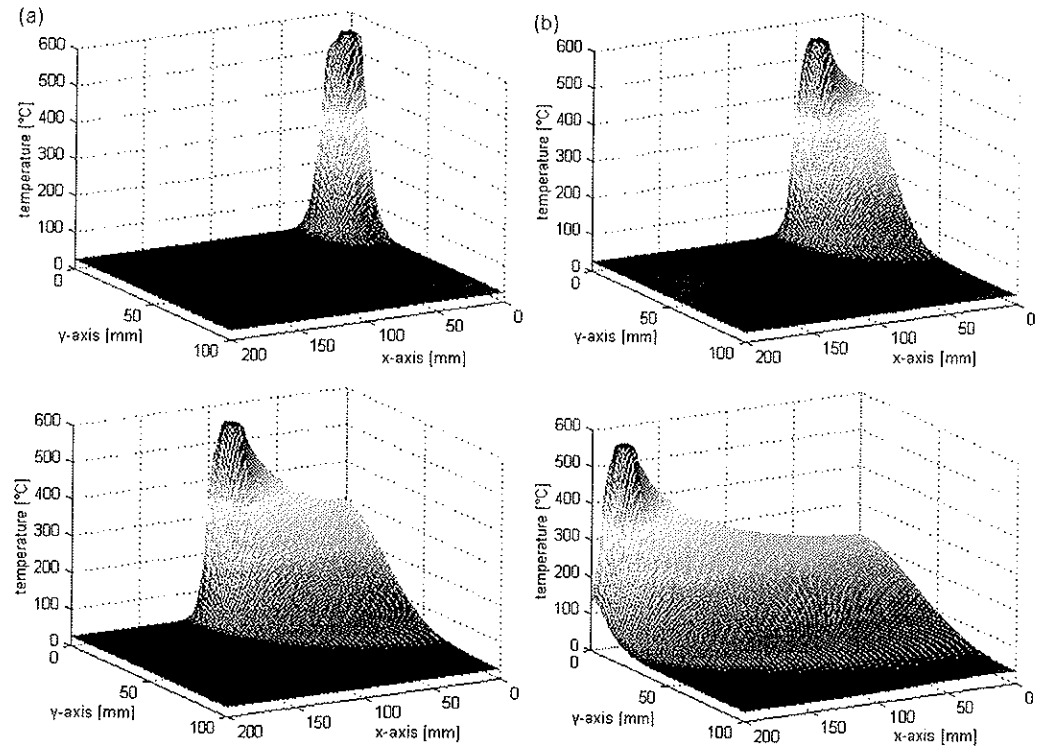
Figure 10 The four different stages in FSW; (a) The stationary heating period
(0.2 seconds after start of welding), (b) The transient heating period (about 50
mm from starting point) (c), The pseudo steady state period (50-170 mm from
starting point), (d) The post steady state period (170-200 mm from starting
point). Operational conditions as in Table 1, case 1.

2.4.2 Temperature in front of the tool

In order to obtain a sound weld the material in the front of the tool must be pre-
heated to a certain temperature to accommodate the plastic deformation during
welding. In a real welding situation the temperature in front of the tool is most
critical. This point is illustrated in Figure 11 where the temperature in a fixed
position 1mm in front of the heat source is shown for two different welding
speeds (i.e. 12.5 and 20 mm/s, respectively). After the stationary heating period
the temperature is 400 °C before the heat source starts to move. At the lowest
speed of welding (i.e. 12.5 mm/s) the temperature reaches a saturation level of
about 450 °C, whereas it drops to approximate 320 °C at 20 mm/s. In order to

reach 450 °C in the latter case the heat input per unit length of the weld must be increased by raising the net power, q_0. This can be done by increasing the radius R of the shoulder or the rotational speed N.
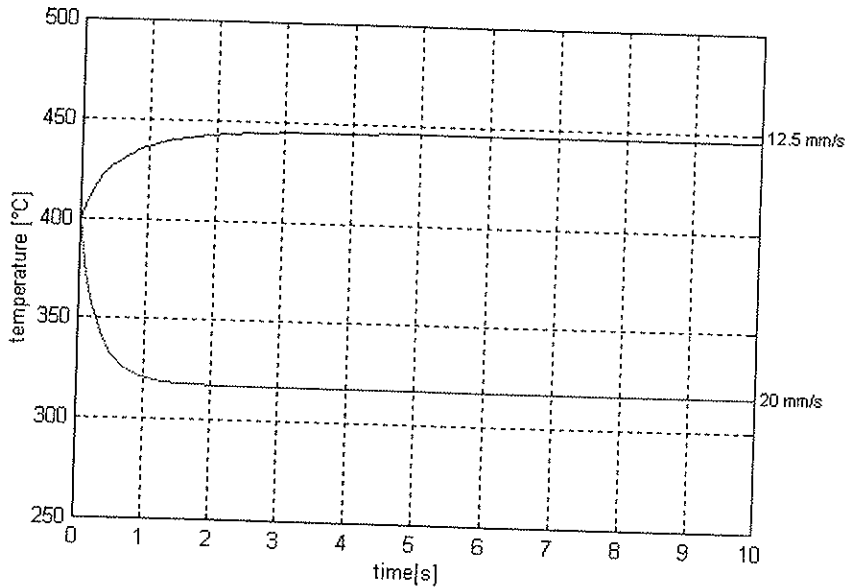
Figure 11 Calculated temperatures 1mm in front of the tool at two different welding speeds. Operational conditions as in Table 1, case 2 and case 3.

At pseudo-steady state the temperature distribution in thin plate welding is determined by the parameter, q_0/vd [kJ/mm^2], where v is the welding speed and d is the plate thickness. It follows that the temperature in front of the tool will decrease if the welding speed increases and q_0 remains constant. This point is more clearly illustrated in Figure 12, which shows a plot of the temperature 1mm ahead of the tool for a constant heat input (i.e. fixed q_0). A closer inspection of the figure reveals that an increase in the welding speed is always accompanied by a corresponding decrease in the temperature. In a real welding situation this eventually leads to pin fracture and formation of weld defects as the material becomes less formable.
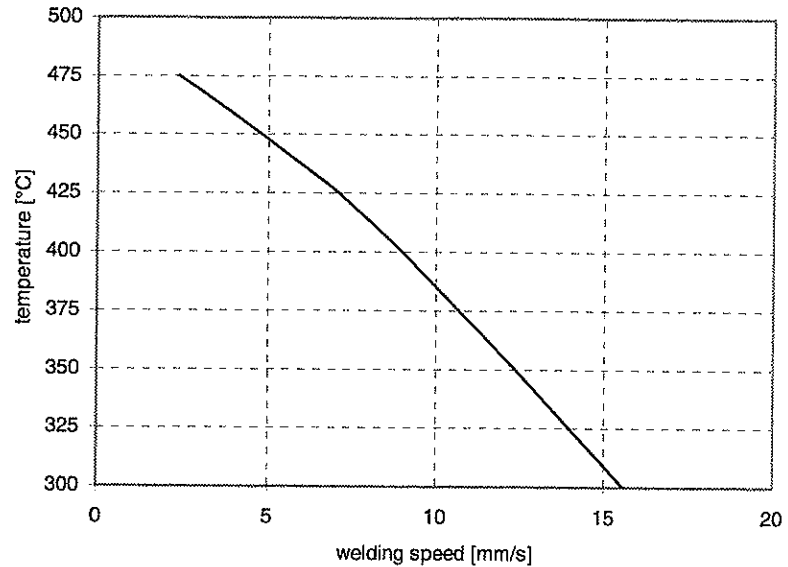
Figure 12 Effect of welding speed on the temperature 1 mm in front of the tool as, predicted from the model. Operational conditions as in Table 1, case 4.

2.4.3 Thermal cycles

The model can also be used to predict the HAZ thermal cycles in the transverse direction of the weld at different positions along the plate, as shown in Figure 13. In the present example it is seen that pseudo-steady state is attained after a total weld length of about 50 mm. When three quarter of the weld is completed reflection of heat from the end plate surface will start to influence the HAZ thermal program. In practice, this means that the thermal cycles at fixed positions within the HAZ become shifted towards higher peak temperatures.
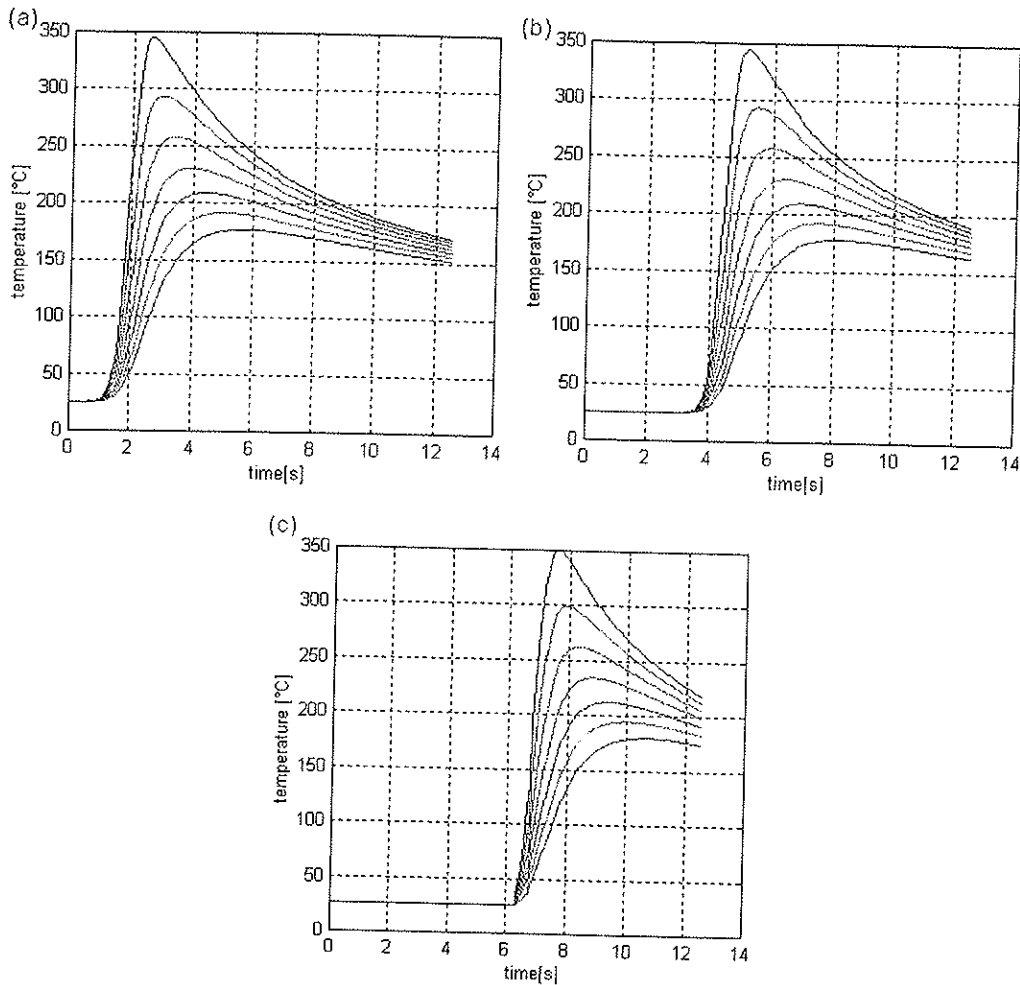
Figure 13 Examples of predicted HAZ thermal cycles in the transverse direction of the weld at different positions along the plate; (a) 50 mm from starting point, (b) 100 mm from starting point, and (c)150 mm from starting point. The thermal cycles refer to the following positions within the HAZ: 11, 13, 15, 17, 19, 21 and 23 mm. Operational conditions as in Table 1, case 5.

2.4.4 Isothermal zone widths

In a contour plot the peak temperature of the thermal cycle corresponds to the point where the isotherm reaches its maximum width, see Figure 14(a). Consequently, such diagrams can be used to read-off the total width of the HAZ. For example, if the temperature for incipient dissolution of the hardening β''-Mg_2Si phase in Al-Mg-Si alloys is taken equal to 250°C /8/, the total width of the HAZ is about 15mm when the tool shoulder radius is 8 mm. This value increases to approximately 19 mm if the tool shoulder radius is increased to 10 mm, as shown in Figure 14(b). Restrictions in the applied heat input are therefore required to avoid excessive HAZ softening during FSW of aluminium alloys.
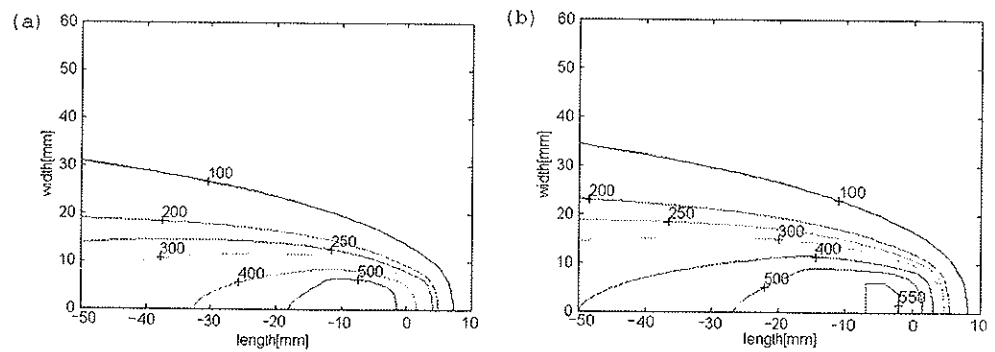
Figure 14 Examples of isothermal contour plots for two different tool sizes (a) R=8 mm (b) R=10 mm. The position of the heat source (i.e. x=0) is 140 mm from the starting point. Operational conditions as in Table 1; a: case 2, b: case 5.

2.5 References

1. C. J. Dawes and W. M. Thomas, Welding Journal, March 1996.

2. O.T. Midling and H.G. Johansen, Presentation at the 6th International Aluminium Technology Seminar & Exposition, ET96, Chicago, Illinois14.-17. May 1996.

3. O.T. Midling, Proceedings of the Aluminium 97 Conference, 24.-25. September 1997, Essen, Germany.

4. A.O. Kluken and B. Bjørneklett, A study of Mechanical Properties for Aluminium GMA Weldments. Welding Journal, February 1997.

5. O.R. Myhr and Ø. Grong: Acta Metall. Mater., 1991, 39, 2693-2702; ibid.,2703-2708.

6. H.S. Carslaw and J.C. Jaeger: Conduction of Heat in Solids; 1959, Oxford, Oxford University Press.

7. R.W.K. Honeycombe: Steel-Microstructure and Properties, 1980, London, Edward Arnold (Publishers) Ltd.

8. Ø. Grong: Metallurgical Modelling of Welding, The Institute of Materials, Second Ed., London, 1997, pp. 46.

9. W. Cheney and D. Kincaid, Numerical Mathematics and Computing, 3. Ed. , Brooks/Cole Publishing Company, California.

10. Suhas V. Patankar, Numerical heat transfer and fluid flow, Hemisphere Publishing Corporation, 1980.

11. O.T. Midling, Ph.D. thesis, University of Trondheim, The Norwegian Institute of Technology, Department of Metallurgy, 1993.

12. B. Crossland, Friction Welding, Cont. Phys., 1971, vol.12, (6), pp. 559-574.

13. Kong, H.S. and Ashby M.F., Case studies in the application of temperature maps for dry sliding, Engineering Dept. report, Cambridge University, 1991, pp. 4.

Appendix 2.1 - Nomenclature

a	thermal diffusivity (mm^2s^{-1})
A	cross section (mm^2)
d	plate thickness (mm)
k	discretization parameter in time (s)
K_0	modified Bessel function of second kind and zero order
h	discretization parameter in x and y direction (mm)
M	interfacial torque (Nm)
N	rotational speed (rot/s)
O	reference point in stationary co-ordinate system
O'	reference point in moving co-ordinate system
P	arbitrary point of observation (in 2.2 Heat flow modelling)
P	pressure (Nmm^{-2}) (in 2.3 Heat generation)
$P(r)$	pressure distribution across the interface (MPa)
q_0	net power (W)
Q	net heat input (J)
R	tool radius (mm)
r	two dimensional radius vector (mm)
r'	distance from infinitesimal heat source to point P in x-y plane (mm)
T	temperature (°C)
T_0	ambient temperature (°C)
t	time (s)
t', t''	time variables (s)
v	welding speed (mms^{-1})
V	unit volume (mm^3)
w	integration parameter
x	x-axis/welding direction (mm)
x_0	welding direction in stationary co-ordinate system (mm)
y	y-axis/transverse direction (mm)
y_0	transverse direction in stationary co-ordinate system (mm)
σ	dimensionless r-vector
ρc	volume heat capacity ($Jmm^{-3}°C^{-1}$)
λ	thermal conductivity ($Wmm^{-1}°C^{-1}$)
μ	friction coefficient
ω	angular velocity (rad/s)

Appendix 2.2 - MatLab code

This appendix contains the listing of the developed MatLab-programs.

Testing of algorithm

thinplQ.m

%Thin plate solution, analytical.

clear;

%material constants

```
a=62;           %thermal diffusivity [mm^2/s]
thc=0.167;      %thermal conductivity.[W/mm°C]
gc=0.0027;       %[J/mm^3°C]
Tmin=25;        %minimum temperature [°C]
tk=3;           %plate thickness [mm]
```

%step definition

```
dx=1;  %[mm]
dy=dx;  %[mm]
t=1; %[s]

Q=1500;     %[J]

xa=-50;
xb=51;
ya=-50;
yb=51;

for x=xa:1:xb
for y=ya:1:yb
cx=x*dx;
cy=y*dy;
T(x-(xa-1),y-(ya-1))=Tmin+(Q/tk)/(gc*4*pi*a*t)*exp(-
(cx*cx+cy*cy)/(4*a*t));
```

```
end
end

for x=xa:1:xb
X(x-(xa-1))=x*dx;   %[mm]
end
for y=ya:1:yb
Y(y-(ya-1))=y*dx;     %[mm]
end
```

T1=T'; %Ploting the transpose of the matrix (equal plot as num.solution).

```
V=[30,50,100,150,200,300,500,600];
contour(X,Y,T1,V)
cs = contour(X,Y,T1,V);
clabel(cs);
grid;
title('Thin plate solution');
ylabel('width[mm]');
xlabel('length[mm]');
zlabel('temperature [°C]');
```

fdQ.m

%This function calculates new temperature distribution
%after one time step, stationary heat source!

```
function I=fd(I,m,n,dt,dx,a);
```

% Boundary conditions.

```
for i=2:(m-1)
for j=2:(n-1)
if i==2        % (1,j)=(2,j): hence symmetry
I(1,j)=I(i,j);
end
if (i+1)==m     % no heat transfer from plate
I(m,j)=I(i,j);
end
if (j-1)==1     % no heat transfer from plate
```

```
I(i,1)=I(i,j);
end
if (j+1)==n     % no heat transfer from plate
I(i,n)=I(i,j);
end
end
end
```

% Calculating new temperature distribution.

```
for i=2:(m-1)
for j=2:(n-1)
I(i,j)=I(i,j)+(a*dt)/(dx*dx)*(I(i+1,j)+I(i-1,j)-4*I(i,j)+I(i,j+1)+I(i,j-1));
end
end
```

thinpl.m
%Thin plate solution, analytical.

clear;

%material constants

```
a=62;           %thermal diffusivity [mm^2/s]
thc=0.167;      %thermal conductivity.[W/mm°C]


v=1;            %welding speed [m/min]

Tmin=25;        %minimum temperature [°C]
tk=3;           %plate thickness [mm]
```

%step definition

```
dx=1;  %[mm]
dy=dx;  %[mm]

%q0=(my*F*pi^2*d*(d/2)^2*w*2/3*1/60000)*100; %[W]
```

```
q0=1500;     %[W]

v=1000/60*v;
xa=-20;
xb=20;
ya=0;
yb=40;

for x=xa:1:xb
for y=ya:1:yb
cx=x*dx;
cy=y*dy;
K=besselk(0,(v*(cx*cx+cy*cy)^0.5)/(2*a));
T(x-(xa-1),y+1)=Tmin+(q0/tk)/(2*pi*thc)*exp(-(v*cx)/(2*a))*K;
end
end


for x=xa:1:xb
X(x-(xa-1))=x*dx;   %[cm]
end

for y=ya:1:yb
Y(y+1)=y*dx;     %[cm]
end

T1=T'; %Ploting the transpose of the matrix (equal plot as num.solution).

V=[50,100,200,300,400,500,600];
contour(X,Y,T1,V)
cs = contour(X,Y,T1,V);
clabel(cs);
grid;
title('Thin plate solution');
ylabel('width[mm]');
xlabel('length[mm]');
zlabel('temperature [°C]');
```

fsw2d1.m

```
% 2-D model FSW, Finite difference, Explicit Method. Test analytical solution
comparison.

clear;

%material constants
gc=2.7e6;    %[J/m3°C]
a=62;               %thermal diffusivity [mm^2/s]

Tmin=25;     %plate temperature at time=0 [°C]
width=80;        %plate width  [mm]
length=200;  %plate length [mm]
tk=3;               %plate thickness [mm]
pos=0;

%step and matrix definition

dx=1; %[mm]
dy=dx;   %[mm]
dt=0.0005; %[s]
m=width/(2*dy)+2;
n=length/dx+2;
I=zeros(m,n); %defines the matrix

v=1;   %welding speed [m/min].

q0=1500;     %total energy input [W]

%source=4 grid.points.
dT=dt*q0/(gc*tk/1000*(2*dx/1000)^2); %Temperature increase [°C]

%values at t=0

for i=1:m
for j=1:n
I(i,j)=Tmin;
end
end
```

```
pos=10/dx;   %starting at position 10 [mm]

% Moving heat source.
ttot=length/(v*1000)*60;
dtp=dx/(v*1000)*60;
grid=round(dtp/dt);
t=0;
while pos<152
t=t+dtp;
pos=pos+1; %changing tool location one grid-length
I(1,1)=pos;
for teller=1:grid
I=fd1(I,m,n,pos,dt,dx,dT,a);
end
end
```

fd1.m

```
%This function calculates new temperature distribution
%after one time step.

function I=fd(I,m,n,pos,dt,dx,dT,a);


% Boundary conditions.

for i=2:(m-1)
for j=2:(n-1)
if i==2       % (1,j)=(2,j): hence symmetry
I(1,j)=I(i,j);
end
if (i+1)==m     % no heat transfer from plate
I(m,j)=I(i,j);
end
if (j-1)==1     % no heat transfer from plate
I(i,1)=I(i,j);
end
if (j+1)==n     % no heat transfer from plate
I(i,n)=I(i,j);
```

```
end
end
end
```

`%source=4 grid-points.`

```
I(2,pos)=I(2,pos)+dT; %Adding dT to source position.
I(2,pos+1)=I(2,pos+1)+dT;
I(1,pos)=I(1,pos)+dT; %Adding dT to source position.
I(1,pos+1)=I(1,pos+1)+dT;
```

`% Calculating new temperature distribution.`

```
for i=2:(m-1)
for j=2:(n-1)
I(i,j)=I(i,j)+(a*dt)/(dx*dx)*(I(i+1,j)+I(i-1,j)-4*I(i,j)+I(i,j+1)+I(i,j-1));
end
end
```

Numerical model

fsw2d.m

`% 2-D model FSW, Finite difference, Explicit Method.`

`clear;`

```
%material constants
gc=2.7e6;       %[J/m^3°C]
my=0.5;         %friction coefficient
a=62;           %thermal diffusivity [mm^2/s]
```

```
%process parameters
P=10e6;         %normal force [N]
w=2500;         %tool rotation speed [rot/min]
d=16;           %tool shoulder [mm]
v=1.2;          %welding speed [m/min]
```

```
Tmin=25;        %minimum temperature [°C]
Tmax=550;       %maximum temperature [°C]
width=200;      %plate width  [mm]
length=200;     %plate length [mm]
tk=3;           %plate thickness [mm]
pos=0;

%step definition

dx=1;   %[mm]
dy=dx;  %[mm]
dt=0.0005; %[s]
by=(d/2)/dy;
bx=(d)/dx;
m=width/(2*dy)+2;
n=length/dx+2;

I=zeros(m,n); %defines the matrix
T=Tmin;         %tool temperature at t=0

dTtool=tempdist(d,tk,by,bx,dx,dt,P,w,gc,my,Tmax); %Calculating temp.
distribution.
%mesh(dTtool);
%pause;

%values at t=0

for i=1:m
for j=1:n
I(i,j)=Tmin;
end
end



%Transient heating period.

transtime=0;
pos=pos+bx;
```

```
pos2=1;
while I(2,pos+1)<400
I=fd(I,m,n,pos,by,bx,dt,dx,dTtool,a,Tmax);
transtime=transtime+dt;
end
transtime
%tplot(I,dx);
%pause
save c:\matlab\data\case41.mat


%Moving heat source.

ttot=length/(v*1000)*60;
dts=dx/(v*1000)*60;
grid=round(dts/dt);
t=0;
while pos<(n-1) | I(2,n-2)>250
t=t+dts;
I(1,1)=pos;  %I(1,1) storing tool location.
if pos<n+1
Tfront(1,pos2)=I(2,pos+1); %position two grids in front of tool.
end
Tpos1(1,pos2)=I(12,51);
Tpos2(1,pos2)=I(14,51);
Tpos3(1,pos2)=I(16,51);
Tpos4(1,pos2)=I(18,51);
Tpos5(1,pos2)=I(20,51);
Tpos6(1,pos2)=I(22,51);
Tpos7(1,pos2)=I(24,51);
Tpos8(1,pos2)=I(26,51);
Tpos9(1,pos2)=I(28,51);
Tpos10(1,pos2)=I(30,51);
if pos>80
Tpos21(1,pos2)=I(12,101);
Tpos22(1,pos2)=I(14,101);
Tpos23(1,pos2)=I(16,101);
Tpos24(1,pos2)=I(18,101);
Tpos25(1,pos2)=I(20,101);
Tpos26(1,pos2)=I(22,101);
Tpos27(1,pos2)=I(24,101);
```

```
Tpos28(1,pos2)=I(26,101);
Tpos29(1,pos2)=I(28,101);
Tpos210(1,pos2)=I(30,101);
end
if pos>141
Tpos31(1,pos2)=I(12,151);
Tpos32(1,pos2)=I(14,151);
Tpos33(1,pos2)=I(16,151);
Tpos34(1,pos2)=I(18,151);
Tpos35(1,pos2)=I(20,151);
Tpos36(1,pos2)=I(22,151);
Tpos37(1,pos2)=I(24,151);
Tpos38(1,pos2)=I(26,151);
Tpos39(1,pos2)=I(28,151);
Tpos310(1,pos2)=I(30,151);
end
pos=pos+1; %changing tool location one grid-length
pos2=pos2+1;
if pos>n-1
pos=n-1
dTtool=dTtool.*0;
end
for teller=1:grid
I=fd(I,m,n,pos,by,bx,dt,dx,dTtool,a,Tmax);
end
if pos==(n-50*dx)
save c:\matlab\data\case44.mat;
end
if pos==(n-100*dx)
save c:\matlab\data\case43.mat;
end
if pos==(n-150*dx)
save c:\matlab\data\case42.mat;
end
end
save c:\matlab\data\case45.mat;
tplot(I,dx);
```

tempdist.m

```
%This function calculates new temperature distribution
%under tool shoulder

function dTtool=tempdist(d,tk,by,bx,dx,dt,P,w,gc,my,Tmax);


dTtool=zeros(by,bx);

% distributing the heat increase under shoulder.
Xmaks=bx;
Xmin=1;
Y=by;

while Y>0
R1=(Y*dx/1000)^3-((Y-1)*dx/1000)^3; %calculating in [m]
R2=(Y*dx/1000)^2-((Y-1)*dx/1000)^2;   %calculating in [m]
dT=(4/3*pi*my*P*w/60*R1*dt)/(gc*tk/1000*R2);
if Y>1
for i=1:Y-1
dTtool(i,Xmin)=dTtool(i,Xmin)+dT;
if dTtool(i,Xmin)>Tmax    %Max. temp. under shoulder=Tmax
dTtool(i,Xmin)=Tmax;
end
dTtool(i,Xmaks)=dTtool(i,Xmaks)+dT;
if dTtool(i,Xmaks)>Tmax    %Max. temp. under shoulder=Tmax
dTtool(i,Xmaks)=Tmax;
end
end
end
for j=Xmin:Xmaks
dTtool(Y,j)=dTtool(Y,j)+dT;
if dTtool(Y,j)>Tmax    %Max. temp. under shoulder=Tmax
dTtool(Y,j)=Tmax;
end
end
Xmin=Xmin+1;
Xmaks=Xmaks-1;
Y=Y-1;
```

```
end
```

fd.m

```
%This function calculates new temperature distribution
%after one time step.

function I=fd(I,m,n,pos,by,bx,dt,dx,dTtool,a,Tmax);



% distributing the heat increase under shoulder.

% evaluating the heat flow.
for i=2:(m-1)        % no heat transfer from plate
I(i,1)=I(i,2);
I(i,n)=I(i,n-1);
end
for j=2:(n-1)        % no heat transfer from plate
I(1,j)=I(2,j);
I(m,j)=I(m-1,j);
end

coun1=0;
for k=(pos-bx+2):(pos+1)
coun1=coun1+1;
coun2=0;
for l=1:by
coun2=coun2+1;
I(l,k)=I(l,k)+dTtool(coun2,coun1);
if I(l,k)>Tmax
I(l,k)=Tmax;
end
end
end

for i=2:(m-1)
for j=2:(n-1)
I(i,j)=I(i,j)+(a*dt)/(dx*dx)*(I(i+1,j)+I(i-1,j)-4*I(i,j)+I(i,j+1)+I(i,j-1));
end
```

end

Graphics
tplot.m

%This procedure makes a 3-D plot of the plate based on the I matrix.

```
function tplot(I,h);
k=size(I);
m=k(1,1);
n=k(1,2);
P=zeros(m-2,n-2);
for j=2:(n-1)
for i=2:(m-1)
P(i-1,j-1)=I(i,j);
end
end
Y=zeros((m-2),1);
X=zeros((n-2),1);
X(1)=0;
Y(1)=0;
for c=2:(n-2)
X(c)=X(c-1)+h;
end

for c=2:(m-2)
Y(c)=Y(c-1)+h;
end
mesh(X,Y,P);
grid;
title('FSW');
ylabel('width[mm]');
xlabel('length[mm]');
zlabel('temperature [°C]')
```

tsurf.m

%This procedure makes a temperature contour plot of the plate based on the I matrix.

```
function tsurf(I,h);
k=size(I);
m=k(1,1);
n=k(1,2);
P=zeros(m-2,n-2);
for j=2:(n-1)
for i=2:(m-1)
P(i-1,j-1)=I(i,j);
end
end
Y=zeros((m-2),1);
X=zeros((n-2),1);
X(1)=0;
Y(1)=0;
for c=2:(n-2)
X(c)=X(c-1)+h;
end
for c=2:(m-2)
Y(c)=Y(c-1)+h;
end
V=[100,200,300,400,500,550];
contour(X,Y,P,V);
cs = contour(X,Y,P,V);
clabel(cs);
grid;
title('FSW');
ylabel('width[mm]');
xlabel('length[mm]');
zlabel('temperature [°C]');
```

tposplot.m

%Gives a plot of temperature history of spec. point.

function Tplot=Tposplot(dts,Tpos1,Tpos2,Tpos3,Tpos4,Tpos5,Tpos6,Tpos7);

```
time=zeros(size(Tpos1));
[i,j]=size(Tpos1);
time(1,1)=0;
for dtime=2:j
time(1,dtime)=time(1,dtime-1)+dts;
end
%plot(time,Tpos1,'r',time,Tpos2,'b');
plot(time,Tpos1,time,Tpos2,time,Tpos3,time,Tpos4,time,Tpos5,time,Tpos6,tim
e,Tpos7)
grid;
title('FSW thermal history');
xlabel('time[s]');
ylabel('temperature [°C]');
```

kplot.m

%This procedure makes a contour of the heat source.
%I(1,1) referes to the tool position.

```
function kplot(I,h);
k=size(I);
m=k(1,1);
n=k(1,2);
test=1;
P=zeros(m-2,m-2);
for j=1:m-2
for i=2:(m-1)
a=round(I(1,1)-m/2+j-1); %pos. Y direction.
if a<1 | test==0 | n<I(1,1)+m/2
test=0;
a=j;
end
P(i-1,j)=I(i,a);
```

```
end
end
Y=zeros((m-2),1);
X=zeros((m-2),1);
X(1)=0;
Y(1)=0;
for c=2:(m-2)
X(c)=X(c-1)+h;
end

for c=2:(m-2)
Y(c)=Y(c-1)+h;
end
V=[100,200,250,300,400,500,550];

contour(X,Y,P,V);
cs = contour(X,Y,P,V);
clabel(cs);
grid;
title('FSW');
ylabel('width[mm]');
xlabel('length[mm]');
zlabel('temperature [°C]')
```

Part III: A 3-D HEAT FLOW MODEL FOR FRICTION STIR WELDING

3.1 Introduction

The interest in friction stir welding (FSW) has gained considerable momentum over the past few years /1/. This is because the process has made it possible to implement the advantage of solid state bonding to plate and profile joints, thus leading to new product design previously not feasible /2/. In FSW the heat is generated by rotating movement of the shoulder and the pin. The frictional heating contributes to the formation of a plasticized layer of soft metal beneath the tool shoulder and about the pin. The material is then transported to the shear side of the tool due to the imposed mechanical stirring and forging action before it cools and forms a solid state joint /3/.

In order to take full advantage of the FSW process, it is necessary to understand and predict the microstructure evolution during welding. All welding techniques applied to heat treatable alloys represent local reheating of a material that has previously undergone a tight temperature control to achieve the desired mechanical properties. Hence, great attention must be given to the HAZ (heat affected zone) temperature-time pattern during welding in order to select welding parameters suitable for the given application /4,5/.

In Part III of the thesis, attempts have been made to model the full temperature distribution during FSW of aluminium alloys, based on the finite difference approach. The algorithm reported here solves the differential heat flow equation for the appropriate boundary conditions in three dimensions. Because the assumption of straight isotherms in the through thickness direction of the plate is relaxed, this model is believed to yield a temperature-time pattern that is more in accordance with experimental observations.

3.2 Heat flow modelling

The symbols and units used throughout the chapter are defined in Appendix 3.1.

In FSW the heat generation takes place mainly under the tool. This leads to variable thermal gradients in the through thickness direction of the plate. The temperature distribution is in this case described using a 3-D heat flow model. If the thermal diffusivity, λ, is assumed constant and independent of temperature the following heat flow equation applies /6/:

$$\rho c \frac{\partial T}{\partial t} = \lambda \left(\frac{\partial^2 T}{\partial x^2} + \frac{\partial^2 T}{\partial y^2} + \frac{\partial^2 T}{\partial z^2} \right) + \frac{q_0}{V} \qquad (1)$$

The other symbols have their usual meaning and are defined in Appendix 3.1.

3.2.1 Analytical medium thick plate solution

In a real welding situation the assumption of three-dimensional or two-dimensional heat flow inherent in the Rosental equations is not always met because of variable temperature gradients in the through thickness z direction of the plate.

The general medium thick plate model considers a point heat source moving at constant speed across a wide plate of finite thickness d. With the exception of certain special cases (e.g. water-cooling of the back side of plate), it is a reasonable approximation to assume that plate surfaces are impermeable to heat. Thus in order to maintain the net flux of heat through both boundaries equal to zero, it is necessary to account for mirror reflections of the source with respect to the planes of $z=0$ and $z=d$. This can be done on the basis of the 'method of images', as illustrated in Figure 1. By including all contributions from the imaginary sources $...2q_{-2}, 2q_{-1}, 2q_1, 2q_2,...$ located symmetrically at distances $\pm 2id$ below and above the upper surface of the plate, the pseudo-steady state temperature distribution is obtained in the form of a convergent series /7,8/:

$$T - T_0 = \frac{q_0}{2\pi\lambda} \exp\left(-\frac{vx}{2a}\right) \times \left[\sum_{l=-\infty}^{l=\infty} (1/R_l) \exp\left(-\frac{v}{2a} R_l\right)\right]$$ (2)

where $R_l = \sqrt{x^2 + y^2 + (z - 2id)^2}$

Note that equation (2) is simply the general Rosental thick plate solution summed for each source.

It follows from equation (2) that the thermal conditions will be similar to those in a thick plate close to the centre of the weld. Moreover, Rosenthal /7,8/, has shown on the basis of a Fourier series expansion that equation (2) converges to the general thin plate solution for points located sufficiently far away from the source. However, at intermediate distances from the heat source, the pseudo-steady state temperature distribution will deviate significantly from that observed in thick plate or thin plate welding because of variable temperature gradients in the through-thickness direction of the plate. Within this 'transition region', the thermal programme is only defined by the medium thick plate solution.
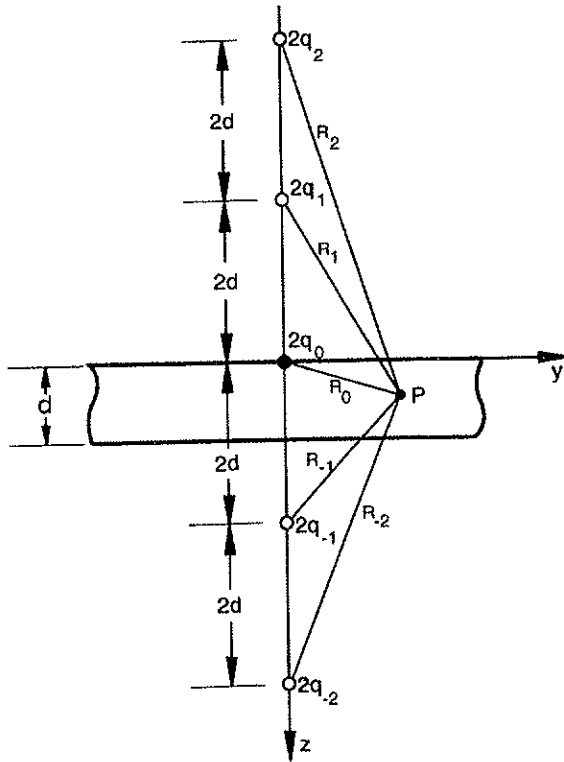
Figure 1 Real and imaginary point sources on a medium thick plate /9/.

3.2.1.1 Practical implications

The following section summarises a case study for aluminium welding described in Ref./9/. The case study is later used to validate the numerical model. Figure 2 shows computed peak temperature contours, using the welding parameters listed in Table 1. A comparison of the computed peak temperature contours reveals a strong influence of the welding speed on the shape and position of the cross-sectional isotherms at a constant gross heat input of 1.5 kJmm^{-1}. It is evident that the extension of the fusion zone and the neighbouring isotherms becomes considerably larger when the welding speed is increased from 2.5 to 5 mms^{-1}. This effect can be attributed to an associated shift from elliptical to more elongated isotherms at the plate surfaces, which reduces heat conduction in the welding direction. Because of the pertinent differences in the heat flow conditions, the temperature-time pattern will also vary significantly between the respective series.

Table 1 Operational conditions used in case study.

Series	q_0 (W)	v (mms^{-1})	d (mm)	E (kJmm^{-1})
A1	6000	5	12.5	1.5
A2	3000	2.5	12.5	1.5

(a)

(b)
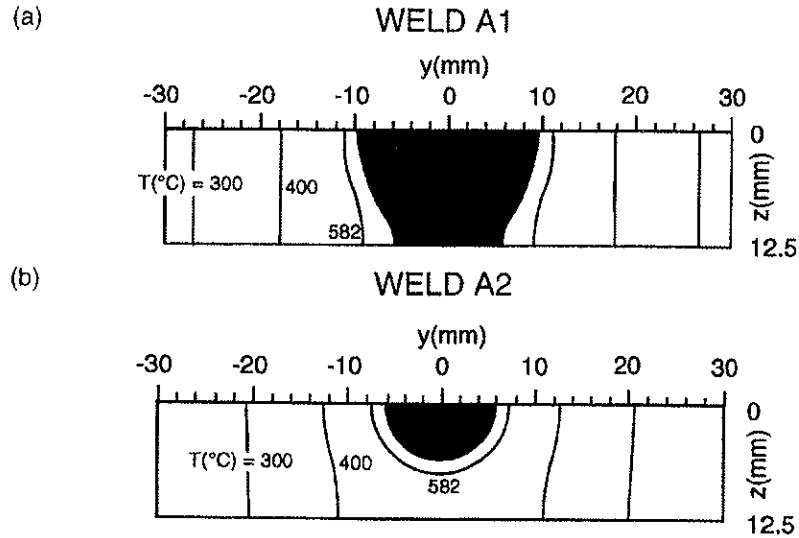
Figure 2 Computed peak temperature contours in aluminium welding at pseudo-steady state (a) Weld A1, (b) Weld A2. Black region indicate fusion zone. Operational conditions as in Table 1. From Ref. /9/.

3.2.2 Numerical heat flow model

Equation (1) is the fundamental mathematical relation describing heat conduction in solids. Obtaining exact analytical solutions for any boundary condition would lead to expressions containing infinite series, special functions, transcendental equations etc.. Thus for many problems of industrial importance the numerical approach is more realistic. The finite difference solution to this heat flow problem consists of changing the derivatives in equation (1) with finite differences /10/:

$$\frac{df}{dx} \approx \frac{1}{k}[f(x+k) - f(x)] \qquad (3)$$

$$\frac{d^2 f}{dx^2} \approx \frac{1}{h^2}[f(x+h) - 2f(x) + f(x-h)] \qquad (4)$$

By using a uniform grid, we arrive at the following expression if the solution is advanced in the t variable:

$$u(x,y,z,t+k) = u(x,y,z,t) + a\frac{k}{h^2}\begin{bmatrix} u(x+h,y,z,t) + u(x-h,y,z,t) + \\ u(x,y+h,z,t) + u(x,y-h,z,t) + \\ u(x,y,z+h,t) + u(x,y,z-h,t) - \\ 6u(x,y,z,t) \end{bmatrix} \qquad (5)$$

The solutions obtained by the finite difference approach are only approximate because equation (5) represents the finite difference analogy of equation (1). Still if the solution is advanced using small time steps, k, the solution of the discretization equations is expected to approach the exact solution of the corresponding differential equation. The best way of testing the reliability of the solution with respect to choice of descretization, hence h and k, is to compare the output with an exact analytical solution /11/. This will be done in the subsequent section.

3.2.2.1 Implementation of a non-uniform grid

The present model uses an explicit solution algorithm leading to very small k values. In order to decrease the calculation time a non-uniform grid is applied, as illustrated in Figure 3(a) for a 2-D discretization. In this case the number of grid points is reduced from 320 (corresponding to a uniform grid) to 128. This means that a reduction in calculation time of at least 50% can be expected if the non-uniform discretization is used.

(a)

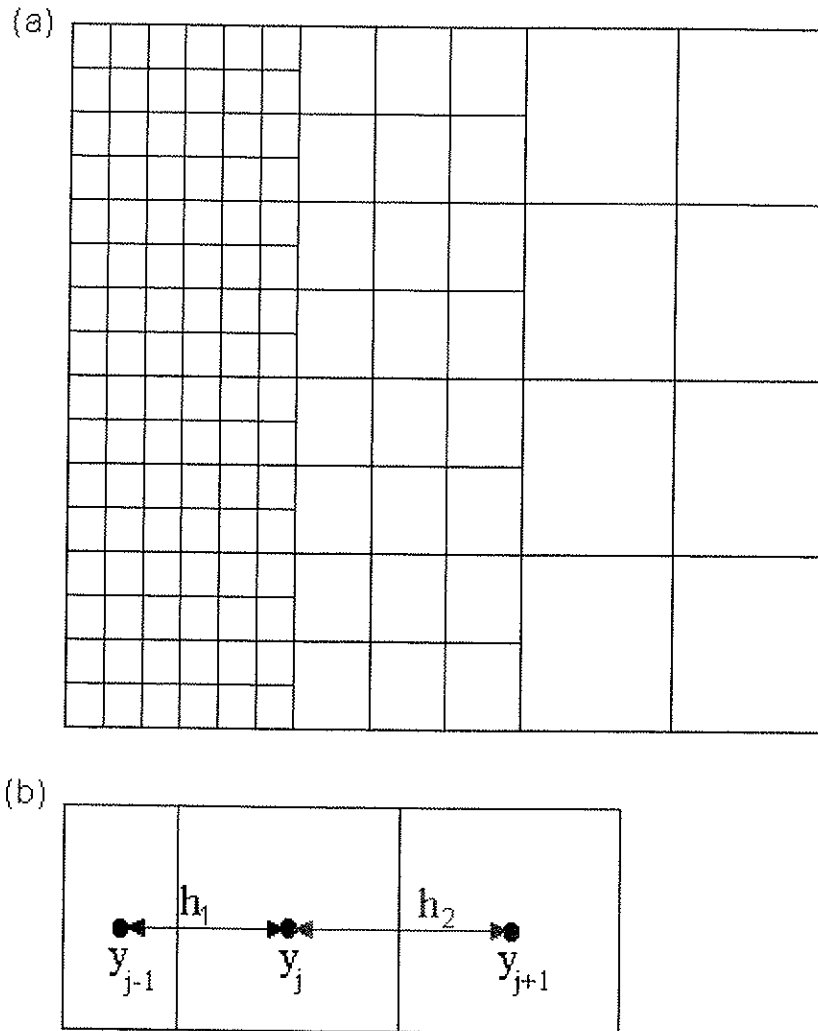
(b)

Figure 3 (a) Schematic illustration of a non-uniform grid for a 2-D discretization. (b) Change in step length at discretization boundary.

As illustrated in Figure 3(b), there are different step lengths from y_{j-1}, y_j compared to y_j, y_{j+1}. This means that equations (4) is not valid across the grid boundaries. By using Taylor's theorem the following equation is obtained:

$$\frac{d^2 f}{dy^2} \approx \frac{\frac{h_2}{h_1} f(y - h_1) - \left(1 + \frac{h_2}{h_1}\right) f(y) + f(y + h_2)}{\left(\frac{h_2^2}{2} + \frac{h_2 h_1}{2}\right)} \qquad (6)$$

By substituting equation (6) into equation (1) it is possible to advance the solution across the different discretizations.

Note that equation (6) correctly reduces to equation (4) when $h_1 = h_2 = h$.

3.2.2.2 Finite difference model for a medium thick plate

In the finite difference model the heat source is assumed to move on top of the plate at a constant speed, v, in the positive x-direction. The algorithm is the same as the one described for the 2-D model in Part II, but extended into three dimensions. In order to reduce the calculation time a non-uniform grid is adopted, and only half the plate is considered due to symmetry. The moving heat source is obtained by calculating the energy input for each time step k by allowing the heat source to move one grid length h after $(h/v)/k$ interations. A full listing of the MatLab code is given in Appendix 3.2.

Figure 4 shows computed cross sectional isotherms for fusion welding on 12 mm thick, 270 mm wide and 150 mm long plates, using the heat input and welding speeds listed in Table 1.
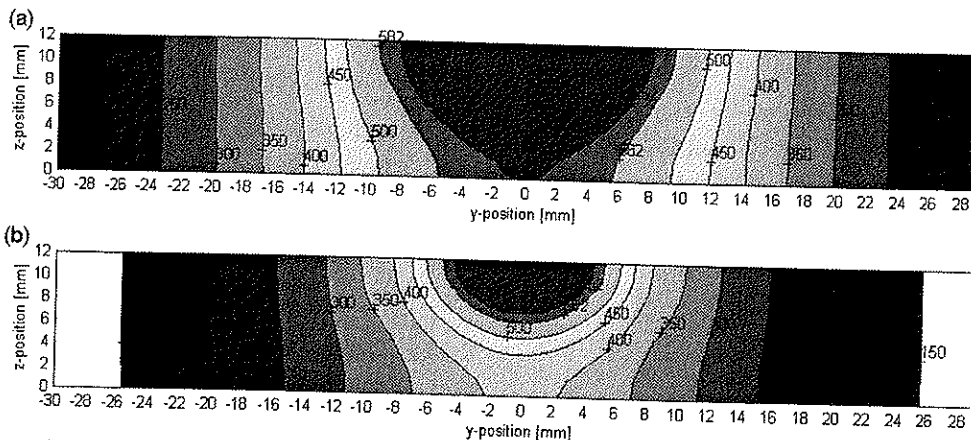

Figure 4 Computed cross sectional isotherms in aluminium welding, using the finite difference model (a) Weld A1, (b) Weld A2. Input data as in Table 1 and Table 2.

A comparison between Figure 2 and Figure 4 reveals a similar temperature-time pattern in both cases, which shows that the numerical solution is sound. However, a true pseudo-steady state is not obtained in the numerical calculations. This is due to the fact that the solution is advanced for a limited time to avoid reflections from the plate edges. The time taken to obtain pseudo-steady state can be read from Figure 5 for welding on thin plates. In Table 2 the actual welding time used in the computations, $t_{com.}$, is compared with the corresponding time required to reach pseudo-steady state, t_{ps}. It follows that $t_{ps} > t_{com}$, which means that the numerical solution should yield isotherms that fall on the inside of those calculated from the pseudo-steady state solution. This is also in agreement with the model predictions.
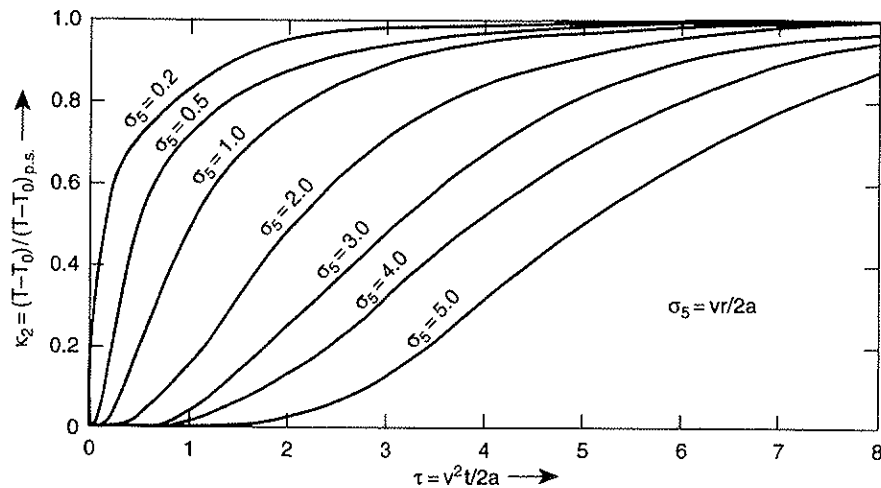
Figure 5 Ratio between real and pseudo-steady state temperature in thin plate welding for different combinations of σ_5 and τ /9/.

Table 2 Time to reach pseudo-steady state t_{ps} in position r=10mm during thin plate welding (t_{com} is the corresponding elapse time used in the numerical calculations).

Case	a $(mm^2 s^{-1})$	σ_5	τ	t_{ps} (s)	t_{com} (s)
A1	62	0.40	5	25	18
A2	62	0.20	3	60	32

3.3 Heat generation

As shown in Part II of the thesis, the heat generation in FSW can be described as:

$$q_0 = \int_0^R 4\pi^2 \mu P N r^2 dr = \frac{4}{3}\pi^2 \mu P N R^3 \qquad (7)$$

where μ is the friction coefficient, R is the surface radius, N is the rotational speed (in [rot/s]) and $P(r)$ is the pressure distribution across the interface (here assumed constant and equal to P [Pa]).

From equation (7) it is obvious that the heat input depends both on rotational speed, N, and the shoulder radius, R , leading to a non-uniform heat generation during welding. These parameters are the main process variables in FSW, since the pressure P cannot exceed the actual flow stress of the material at the operating temperature.

In order to describe the heat source in the numerical model it is more convenient to express the heat generation as a sum of individual contributions (8):

$$q_0 = \frac{4}{3}\pi^2 \mu P N \sum_{i=1}^{n} \left(R_i^3 - R_{i-1}^3 \right) \qquad (8)$$

where R_{i-1} and R_i are defined in Figure 6.

$$\sum_{i=1}^{n} q(R_i) = q_0$$
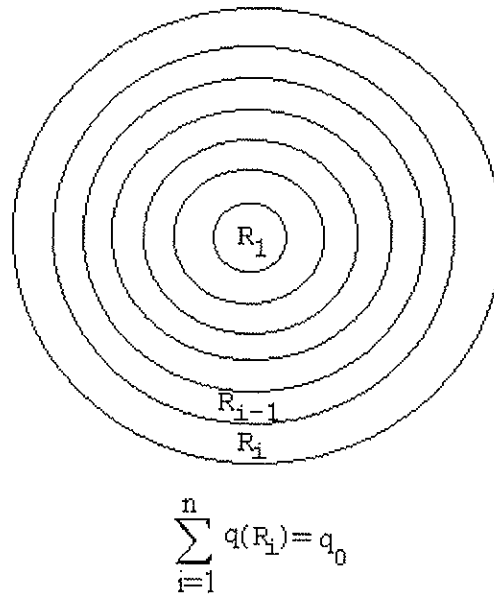
Figure 6. Subdivision of the tool shoulder into a series of volume elements of varying strength.

Hence, the energy generated from position R_{i-1} to R_i is equal to:

$$\Delta q_0 = \frac{4}{3}\pi^2 \mu P N \left(R_i^3 - R_{i-1}^3 \right) \tag{9}$$

In the 3-D numerical model due consideration is given to the heat generation both beneath the tool shoulder and around the rotating pin.

3.3.1 Heat distribution beneath the tool shoulder

Based on equation (9) the heat generation in different positions beneath the tool shoulder can be calculated. Here the strength of each grid point is obtained by dividing the heat input with the total number of grid points involved. As shown in Figure 7 in Part II of the thesis the heat source is approximated by a fixed number of square grid points. This is a reasonable approximation under

the prevailing circumstances, and does not lead to large inherent errors in the calculations.

3.3.2 Heat generation due to the rotating pin

In practice, the heat generation around the rotating tool pin is the result of the interplay between a number of contributions, which cannot readily be accounted for in a mathematical simulation of the process. In order to proceed, the heat generation is assumed to be described by equation (9), where the contribution from the plastic deformation is accounted for by the use of a reasonable average value for the friction coefficient, μ. The heat source itself is extended into the plate by adding square sources, as described in the previous section (3.3.1), in the z-direction. This is illustrated in Figure 7.
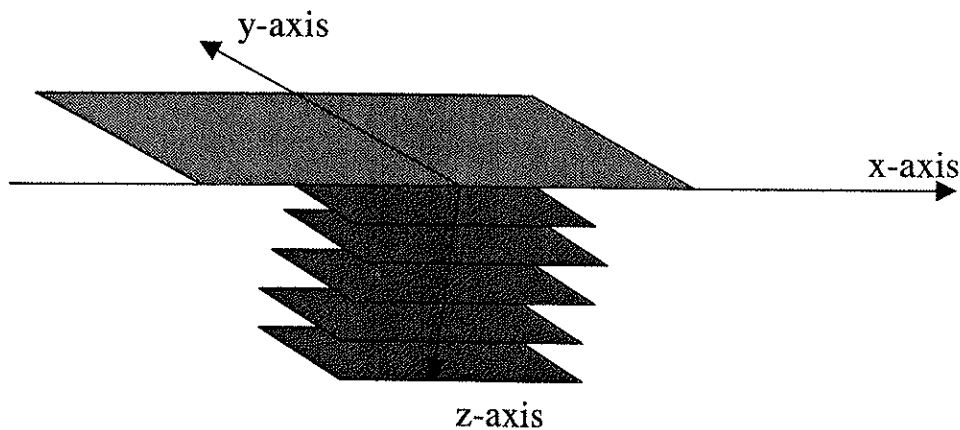
Figure 7 Schematic representation of the heat source used in the 3-D numerical simulations.

3.3.3 Restrictions in heat generation

In thermal processing of aluminium alloys it is generally accepted that local melting will occur if the material is heated above the eutectic temperature at a rate which does not allow the eutectic phase to fully dissolve into the matrix, as illustrated in Figure 8 /9/. If the conditions for local melting are met, the presence of a liquid film on the matrix/tool interface will lubricate the tool shoulder resulting in lack of friction. Consequently, the eutectic temperature

represent the lower limit for the temperature under the tool shoulder, and for Al-Zn-Mg alloys the lower value of T_{max} is close to 475°C, as illustrated in Figure 8(b). Otherwise, T_{max} will approach the solidus temperature of the alloy /12/.

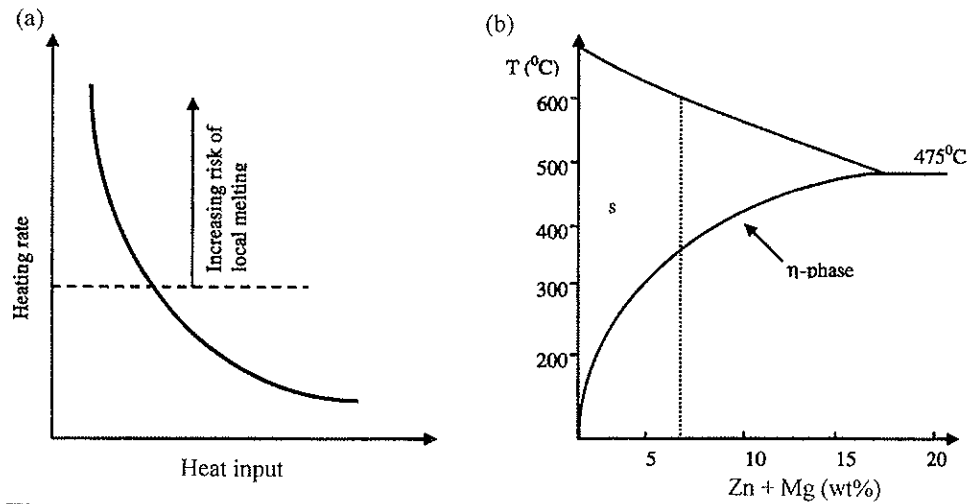Figure 8 Conditions for local melting during FSW of Al-Zn-Mg alloys (schematic); (a) Effect of heat input on the heating rate ahead of the tool shoulder, (b) Quasi-binary section of the Al-(Zn+Mg) phase diagram /13/.

3.4 Case studies

In the following, a series of case studies are presented to illustrate the basic features of the finite difference model and the specific thermal conditions existing in friction stir welding. The case studies consider butt welding of 6mm thick, 150mm long and 100mm wide plates. Table 3 contains a summary of the welding parameters used in the different modelling exercises.

Table 3. Summary of welding parameters used in modelling exercises.

Case No.	T_{max} * [°C]	welding speed [mm/s]	tool shoulder radius [mm]	tool pin radius [mm]	axial pressure [MPa]	rotational speed [rot/min]
Case 1	525	5	7	2	30	1500
Case 2	525	8	7	2	30	1500
Case 3	525	12.5	7	2	30	1500

*Assumed maximum temperature beneath the tool shoulder.

3.4.1 Thermal cycles

The present model can be used to predict the thermal cycle at any discretization point, as illustrated in Figure 9. This figure shows the thermal cycles for all positions in the trough thickness direction of the plate at $x=100$mm and $y=10$mm.
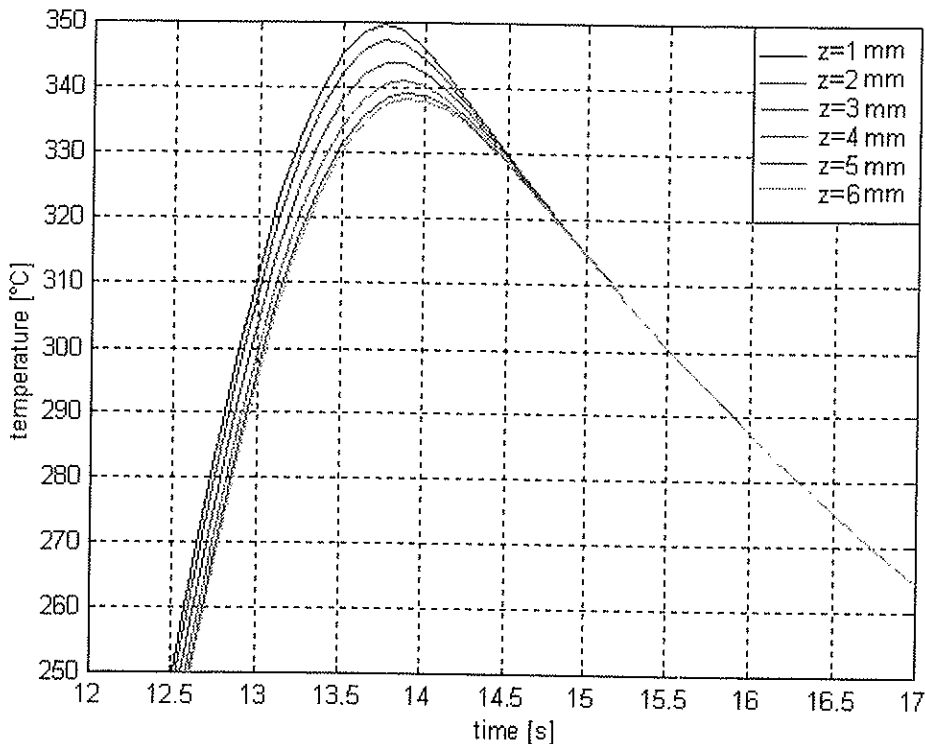
Figure 9 Example of predicted thermal cycles, showing the thermal histories in the through thickness direction of the plate at $x=100$mm and $y=10$mm. Operating conditions as in Table 3, Case2.

3.4.2 Temperatures in the front of the tool

In order to obtain a sound weld the material in the front of the tool must be pre-heated to a certain temperature to accommodate the plastic deformation during welding. This point is illustrated in Figure 10, where the peak temperature contours at the centre of the plate in the x-z plane at pseudo steady state are shown for different welding speeds. The centre of the heat source refers to

position $x=0$. It follows that the temperature in front of the tool will decrease if the welding speed increases for a constant q_0. If it is assumed that the material must be pre-heated to a temperature above, say 450°C in order to flow properly, this region is very narrow and close to the pin position, as shown by the orange shading in Figure 10(c) ($v=12.5$ mm/s). In a real welding situation this defines the conditions for a cold weld, which is characterised by pin fracture and formation of weld defects as the material becomes less formable. In order to reach the required pre-heat temperature the heat input per unit length of the weld must be increased. In practise this is done by increasing the radius R of the shoulder or the rotational speed N.

Figure 10 Calculated peak temperature contours in the length direction of the plate. Operational conditions as in Table 3, Case 1-3, (a) $v=5$ mm/s, (b) $v=8$mm/s and (c) $v=12.5$mm/s.

3.4.3 Cross sectional contours

Figure 11(a)-(c) shows calculated isothermal contours in the cross section of the plate. Such diagrams can be used to read-off the total width of the HAZ. For example, if the temperature for incipient dissolution of the hardening β''-Mg_2Si phase in Al-Mg-Si alloys is taken equal to 250°C /9/, the total width of the HAZ decreases from 19mm at a welding speed of 5 (mm/s), Figure 11(a), to

13 mm at a welding speed of 12.5 mm/s, Figure 11(c). This shows that the total width of the HAZ is sensitive to variations in the welding conditions.
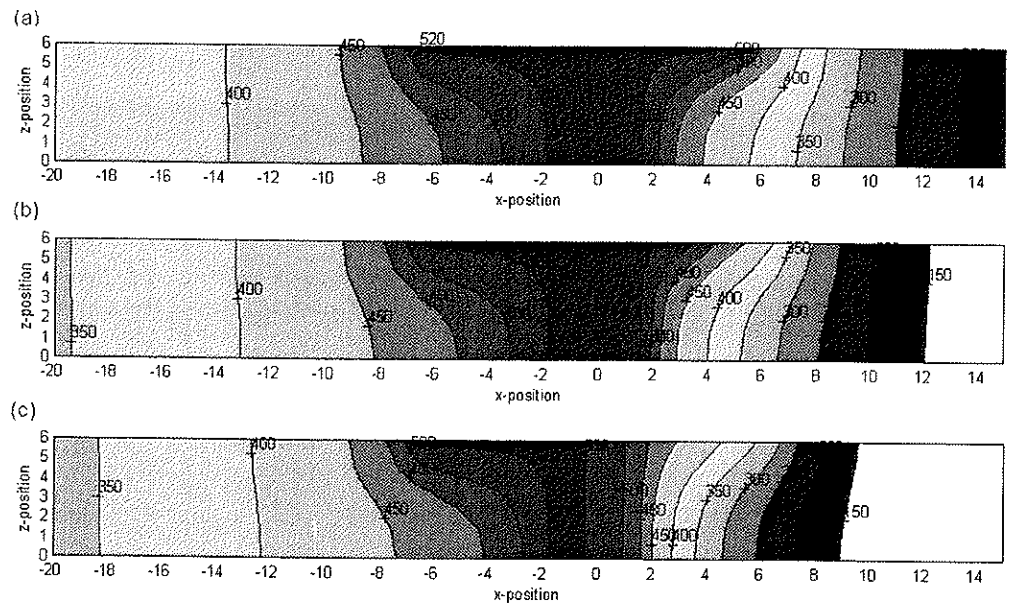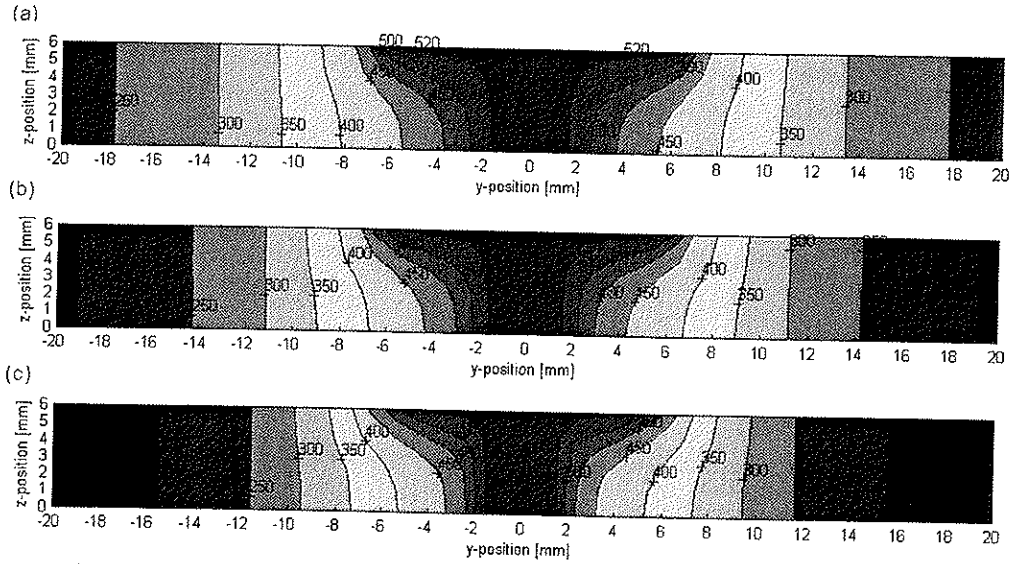

Figure 11 Calculated isothermal contours in the cross section of the plate. Operational conditions as in Table 3, Case 1-3, (a) v=5 mm/s, (b) v=8mm/s and (c) v=12.5mm/s.

3.5 References

1. C. J. Dawes and W. M. Thomas, Welding Journal, March 1996.
2. O.T. Midling and H.G. Johansen, Presentation at the 6th International Aluminium Technology Seminar & Exposition, ET96, Chicago, Illinois14.-17. May 1996.
3. O.T. Midling, Proceedings of the Aluminium 97 Conference, 24.-25. September 1997, Essen, Germany.
4. A.O. Kluken and B. Bjørneklett, A study of Mechanical Properties for Aluminium GMA Weldments. Welding Journal, February 1997.
5. O.R. Myhr and Ø. Grong: Acta Metall. Mater., 1991, 39, 2693-2702; ibid.,2703-2708.
6. H.S. Carslaw and J.C. Jaeger: Conduction of Heat in Solids; 1959, Oxford, Oxford University Press.
7. D. Rosental, Weld. J., 1941, 20, 220s-234s.
8. D. Rosental, Trans, ASME, 1946, 68, 849-866.
9. Ø. Grong: Metallurgical Modelling of Welding, 2. edition, The Institute of Materials, London, 1997, pp. 46.
10. W. Cheney and D. Kincaid, Numerical Mathematics and Computing, 3. ed. , Brooks/Cole Publishing Company, California.
11. Suhas V. Patankar, Numerical heat transfer and fluid flow, Hemisphere Publishing Corporation, 1980.
12. B.I. Bjørneklett, Ø. Frigaard, Ø. Grong, O.R. Myhr and O.T. Midling: Proc. 6th Int. Conf. on Aluminium Alloys- Their Physical and Mechanical Properties, Toyohashi, Japan, July 1998, Vol. III, pp. 1531-1536.
13. B.I. Bjørnekleett, Ph.D. Thesis, Norwegian University of Science and Technology, Trondheim, 1998.

Appendix 3.1 – Nomenclature

a	thermal diffusivity $(\text{mm}^2\text{s}^{-1})$
A	cross section (mm^2)
d	plate thickness (mm)
k	discretization parameter in time (s)
K_0	modified Bessel function of second kind and zero order
h	discretization parameter in x, y and z direction (mm)
h_1, h_2	discretization parameters for a non-uniform grid (mm)
N	rotational speed (rot/s)
P	arbitrary point of observation (in 3.2.1 Analytical medium thick plate solution)
P	pressure (Nmm^{-2}) (in 3.3 Heat generation)
$P(r)$	pressure distribution across the interface (MPa)
q_0	net power (W)
Q	net heat input (J)
R	tool radius (mm)
R_i	distance from real and imaginary heat source to point P in x-y-z space (mm)
r	two dimensional radius vector (mm)
r'	distance from infinitesimal heat source to point P in x-y plane (mm)
T	temperature (°C)
T_0	ambient temperature (°C)
t	time (s)
t_{ps}	time to reach pseudo steady state in thin plate welding (s)
t_{com}	elapsed time in numerical solutions (s)
v	welding speed (mms^{-1})
V	unit volume (mm^3)
x	x-axis/welding direction (mm)
x_0	welding direction in stationary co-ordinate system (mm)
y	y-axis/transverse direction (mm)
y_0	transverse direction in stationary co-ordinate system (mm)
σ_5	dimensionless r-vector
ρc	volume heat capacity $(\text{Jmm}^{-3}{}^{\circ}\text{C}^{-1})$

λ	thermal conductivity ($Wmm^{-1}{}^{\circ}C^{-1}$)
τ	dimensionless time
μ	friction coefficient
ω	angular velocity (rad/s)

Appendix 3.2 - MatLab Code

main program

% Thermal 3D-model FSW, Finite difference, Explicit method. Using pin-source.

```
clear;
global I1 I2 I3 I4;
%plate dimensions
length=150;    %plate length [mm]
width=102;     %plate width  [mm]
thickness=6;       %plate thickness [mm]


%grid (note dx=dy)


dx1=1;   dx2=2;  dx3=2; dx4=6;
dz1=1;   dz2=1;  dz3=2; dz4=6;
dt=0.0005; %[s] (tested for dx>=1)


%size of matrix y-direction (note: x-welding direction, z-thickness)
%NB! matrix sizes must consist with the plate dimensions above!
my1=11; my2=12; my3=16; my4=12; %[mm]


%process parameters
w=1500;    %tool rotation speed [rot/min].
d=20;       %tool shoulder [mm].
pinr=2;    %tool pin radius.
v=0.3;      %welding speed [m/min].
P=2.9842e+007;    %normal pressure [Pa].
Tmax=555;    %defined by the actual alloy [°C].
Tmin=25;      %minimum temperature [°C] (i.e. plate temperature before
welding).
Tstart=450; %temperature required in front of tool to start welding [°C].
THAZ=200;   %minimum temperature affecting HAZ properties [°C].
Tinf=25;   %temperature of backing [°C];
my=0.4;    %friction coefficient.
```

dback=50 %[mm] half diameter of backing plate.
tkb=25 %[mm] thickness of backing
%material constants
gc=2.4e6;   %[J/m^3°C]
a=58.3;   %thermal diffusivity [mm^2/s] (Al-Mg-Si a=62, Al-Mg a=55)
kal=0.167;   %thermal conductivity for Al [W/mm°C]
%kb=0.040;   %thermal conductivity for steel backing plate[W/mm°C]
kb=0;   %Insulated backing.
kbal=(2*kal*kb)/(kal+kb); %thermal conductivity used for calculating heat
%transfer to backing plate [W/mm°C]

% Defining matrix
%NB! all numbers must be integers, else fatal error
I1=ones(length/dx1+2,my1/dx1+1,thickness/dz1+2).*Tmin;
I2=ones(length/dx2+2,my2/dx2,thickness/dz2+2).*Tmin;
I3=ones(length/dx3+2,my3/dx3,thickness/dz3+2).*Tmin;
I4=ones(length/dx4+2,my4/dx4+1).*Tmin; %2D!! i.e. plate thickness=dz4; else
%fatal error.

%source described by grids
dy1=dx1;
by=(d/2)/dy1;
bx=(d)/dx1;

m=length/dx1+2; %number of grid-points in welding direction.

dTtool=tempdist(d,dz1,by,bx,dx1,dt,P,w,gc,my,Tmax); %Calculating temp.
%distribution.

%Transient heating period.
num=1; ; %heat source position at t=0
pos=0;
transtime=0; %time taken to reach starting temperature.
pos=pos+bx;
dts=dx1/(v*1000)*60 %time taken to move one grid point.
grid=dts/dt   %round(dts/dt); Number of iterations before moving NB! integer
%value else fatal error!

```
grid=round(dts/dt)
dts=grid*dt

pos2=0; %variabel used to get temperature history.
teller=0; %counting to check number of iterations during heating.
while I1(pos+1,2,2)<Tstart
histories;   %obtaining thermal histories and saving data.

I1=fd31(I1,I2,pos,by,bx,dt,dx1,dx2,dz1,dTtool,a,Tmax,pinr,thickness,kbal,dback,
Tinf,gc,tkb);
I2=fd32(I2,I3,I1,dt,dx1,dx2,dx3,dz2,a,kbal,Tinf,dback,gc,tkb);
I3=fd33(I2,I3,I4,dt,dx2,dx3,dx4,dz3,a,kbal,my1,dback,Tinf,gc,tkb);
I4=fd34(I3,I4,dt,dx3,dx4,a,my1,my2,dback,Tinf,kbal,thickness,gc,tkb);
transtime=transtime+dt;
teller=teller+1;
if teller>grid
   teller=0;
end
end


transtime %total preheating time
pos2=1; %variable used to get temperature history.

%Moving heat source.

t=0; %time heat-source moves.
while pos<(m-1) | I1(m-1,2,2)>THAZ
t=t+dts;
I1(1,1,1)=pos;  %I1(1,1,1) storing tool location.
Tfront(1,pos2)=I1(pos+1,2,7); %position two grids in front of tool.

histories;   %obtaining thermal histories and saving data.
pos=pos+1    %changing tool location one grid-length
pos2=pos2+1; %parameter used in histories.
if pos>(m-1)  %testing if heat-source has reached end of plate.
   pos=m-1;
   dTtool=dTtool.*0; %heat-source is set off.
```

```
end

for teller=1:grid %calculating temperature distribution before moving heat-source
%one grid point.

I1=fd31(I1,I2,pos,by,bx,dt,dx1,dx2,dz1,dTtool,a,Tmax,pinr,thickness,kbal,dback,
Tinf,gc,tkb);
  I2=fd32(I2,I3,I1,dt,dx1,dx2,dx3,dz2,a,kbal,Tinf,dback,gc,tkb);
  I3=fd33(I2,I3,I4,dt,dx2,dx3,dx4,dz3,a,kbal,my1,dback,Tinf,gc,tkb);
  I4=fd34(I3,I4,dt,dx3,dx4,a,my1,my2,dback,Tinf,kbal,thickness,gc,tkb);
  end
end
```

Procedures used in main program.

```
%This function calculates the temperature distribution
%under the tool shoulder

function dTtool=tempdist(d,tk,by,bx,dx,dt,P,w,gc,my,Tmax);


dTtool=zeros(bx,by);

% Distributing the heat increase under shoulder.
Xmaks=bx;
Xmin=1;
Y=by;

while Y>0
R1=(Y*dx/1000)^3-((Y-1)*dx/1000)^3; %calculating in [m]
q=(4/3*pi*pi*my*P*w/60*R1*dt)/2; %considering half plate due to symmetry.
dT=(q/(Y*2+(Y-1)*2))/(gc*(dx/1000)^3);
if Y>1
 for j=1:Y-1
  dTtool(Xmin,j)=dT;
  dTtool(Xmaks,j)=dT;
```

```
   end
  end
  for i=Xmin:Xmaks
   dTtool(i,Y)=dT;
  end
  Xmin=Xmin+1;
  Xmaks=Xmaks-1;
  Y=Y-1;
 end


%This function calculates new temperature distribution
%after one time step for matrix I1.
%NOTE!! dx1=dy1=dz1=1 dx2=dx2y=2 and dz2=1; else fatal error when
%connecting I1 with I2

function
I1=fd31(I1,I2,pos,by,bx,dt,dx1,dx2,dz1,dTtool,a,Tmax,pinr,tk,kbal,dback,Tinf,gc,
kb);

[m,n,o]=size(I1);

% distributing the heat increase under shoulder.

coun1=0;
for k=(pos-bx+2):(pos+1)
 coun1=coun1+1;
 coun2=0;
 for l=1:by
  coun2=coun2+1;
  I1(k,l+1,2)=I1(k,l+1,2)+dTtool(coun1,coun2);
  if I1(k,l,2)>Tmax
   I1(k,l,2)=Tmax;
  end
 end
end

for z=3:tk+1
```

```
coun1=0;
for k=(pos-pinr-round(bx/2)+2):(pos-round(bx/2)+pinr+1)
 coun1=coun1+1;
 coun2=0;
 for l=1:pinr
  coun2=coun2+1;
  I1(k,l+1,z)=I1(k,l+1,2)+dTtool(bx/2-pinr+coun1,coun2);
  if I1(k,l+1,z)>Tmax
   I1(k,l+1,z)=Tmax;
  end
 end
end
end

%Evaluating the heat flow.

%Heat loss to backing. Considering 1-D heat transfer,
%2x5mm grid, grid1=I1(i,j,o-1), grid2=Tinf.
if dback>1
 if n<dback
  counter=n;
 else
  counter=dback;
 end

 for i=1:m
  for j=1:counter
    I1(i,j,o-1)=I1(i,j,o-1)-(kbal*(I1(i,j,o-1)-
Tinf)/(dz1/2+tkb)*dx1^2*dt)/(gc/1e9*dx1^2*dz1);
  end
 end
end
%setting boundary values.
for k=1:o
 for j=2:n
  I1(1,j,k)=I1(2,j,k);
  I1(m,j,k)=I1(m-1,j,k);
```

```
      end
    end
    for k=1:o
     for i=2:m-1
       I1(i,1,k)=I1(i,2,k);
     end
    end
    for i=1:m
      for j=1:n
        I1(i,j,1)=I1(i,j,2);
        I1(i,j,o)=I1(i,j,o-1);
      end
    end


    for i=2:(m-1)
      for j=2:(n-1)
        for k=2:(o-1)
          I1(i,j,k)=I1(i,j,k)+(a*dt)/(dx1*dx1)*(I1(i+1,j,k)+I1(i-1,j,k)-
4*I1(i,j,k)+I1(i,j+1,k)+I1(i,j-1,k))+(a*dt)/(dz1*dz1)*(I1(i,j,k+1)+I1(i,j,k-1)-
2*I1(i,j,k));
        end
      end
    end


    % connecting I1 with I2
    dy1=dx1;
    dy2=(dx1/2+dx2/2);


    for i=2:(m-1)
      for k=2:(o-1)
        I1(i,n,k)=I1(i,n,k)+(a*dt)/(dz1*dz1)*(I1(i,n,k+1)+I1(i,n,k-1)-
2*I1(i,n,k))+(a*dt)/(dx1*dx1)*(I1(i+1,n,k)+I1(i-1,n,k)-
2*I1(i,n,k))+(a*dt)*((dy2/dy1*I1(i,n-1,k)-(1+dy2/dy1)*I1(i,n,k)+I2(round((i-
1)/2)+1,1,k))/(dy2*dy2/2+dy1*dy2/2));
      end
    end
```

```
%This function calculates new temperature distribution
%after one time step for matrix I2.
%NOTE!! dx1=dy1=dz1=1 dx2=dx2y=2 dz2=1 dx3=dy3=2 dz3=2; else fatal error
%when connecting I2 with I2 and I3
function I2=fd32(I2,I3,I1,dt,dx1,dx2,dx3,dz2,a,kbal,Tinf,dback,gc,tkb);

[m,n,o]=size(I2);
[m1,n1,o1]=size(I1);


% evaluating the heat flow.

%Heat loss to backing. Considering 1-D heat transfer,
%2x5mm grid, grid1=I1(i,j,o-1), grid2=Tinf.
if dback>n1
  if n<(dback-n1)/2
    counter=n;
  else
    counter=round((dback-n1)/2);
  end

  for i=1:m
    for j=1:counter
      I2(i,j,o-1)=I2(i,j,o-1)-(kbal*(I2(i,j,o-1)-
Tinf)/(dz2/2+tkb)*dx2^2*dt)/(gc/1e9*dx2^2*dz2);
    end
  end
end

%setting boundary values.
for k=1:o
 for j=1:n
 I2(1,j,k)=I2(2,j,k);
 I2(m,j,k)=I2(m-1,j,k);
 end
end
```

```
for i=1:m
  for j=1:n
  I2(i,j,o)=I2(i,j,o-1);
  I2(i,j,1)=I2(i,j,2);
  end
end


%connecting I1 and I2
dy1=dx1/2+dx2/2;
dy2=dx2;
for i=2:(m-1)
  for k=2:o-1
    I2(i,1,k)=I2(i,1,k)+(a*dt)/(dx2*dx2)*(I2(i+1,1,k)+I2(i-1,1,k)-
2*I2(i,1,k))+(a*dt)/(dz2*dz2)*(I2(i,1,k+1)+I2(i,1,k-1)-
2*I2(i,1,k))+(a*dt)*((dy2/dy1*(I1(i*2-2,n1,k)+I1(i*2-1,n1,k))/2-
(1+dy2/dy1)*I2(i,1,k)+I2(i,2,k))/(dy2*dy2/2+dy2*dy1/2));
  end
end


%main matrix
for i=2:(m-1)
  for j=2:(n-1)
    for k=2:(o-1)
      I2(i,j,k)=I2(i,j,k)+(a*dt)/(dx2*dx2)*(I2(i+1,j,k)+I2(i-1,j,k)-
4*I2(i,j,k)+I2(i,j+1,k)+I2(i,j-1,k))+(a*dt)/(dz2*dz2)*(I2(i,j,k+1)+I2(i,j,k-1)-
2*I2(i,j,k));
    end
  end
end


%connecting I2 and I3
for i=2:(m-1)
 for k=2:(o-1)
```

```
I2(i,n,k)=I2(i,n,k)+(a*dt)/(dx2*dx2)*(I2(i+1,n,k)+I2(i-1,n,k)-
2*I2(i,n,k))+(a*dt)/(dz2*dz2)*(I2(i,n,k+1)+I2(i,n,k-1)-
2*I2(i,n,k))+(a*dt)/(dx2*dx2)*(I2(i,n-1,k)+I3(i,1,floor(k/2)+1)-2*I2(i,n,k));
 end
end


%This function calculates new temperature distribution
%after one time step for matrix I2.
%NOTE!! dx2=dx2y=2 dz2=1 dx3=dy3=dz3=2 dx4=dy4=dz4=6 else fatal error
%when connecting I3 with I2 and I4
function I3=fd33(I2,I3,I4,dt,dx2,dx3,dx4,dz3,a,kbal,my1,dback,Tinf,gc,tkb);


[m,n,o]=size(I3);
[m1,n1,o1]=size(I2);


% evaluating the heat flow.


%Heat loss to backing. Considering 1-D heat transfer,
%2x5mm grid, grid1=I1(i,j,o-1), grid2=Tinf.
if dback>(my1+2*n1)
 if n<(dback-n1-my1)/2
   counter=n;
 else
   counter=round((dback-n1-my1)/2);
 end


 for i=1:m
   for j=1:counter
     I3(i,j,o-1)=I3(i,j,o-1)-(kbal*(I3(i,j,o-1)-
Tinf)/(dz3/2+tkb)*dx3^2*dt)/(gc/1e9*dx3^2*dz3);
   end
 end
end


%setting boundary values.
for k=1:o
 for j=1:n
```

```
I3(1,j,k)=I3(2,j,k);
I3(m,j,k)=I3(m-1,j,k);
 end
end

for i=1:m
 for j=1:n
 I3(i,j,o)=I3(i,j,o-1);
 I3(i,j,1)=I3(i,j,2);
 end
end

%conecting I2 and I3
dy1=dx2/2+dx3/2;
dy2=dx3;
for i=2:(m-1)
 for k=2:o-1
 I3(i,1,k)=I3(i,1,k)+(a*dt)/(dx3*dx3)*(I3(i+1,1,k)+I3(i-1,1,k)-
2*I3(i,1,k))+(a*dt)/(dz3*dz3)*(I3(i,1,k+1)+I3(i,1,k+1)-
2*I3(i,1,k))+(a*dt)*((dy2/dy1*((I2(i,n1,k*2-1)+I2(i,n1,k*2-2))/2)-
(1+dy2/dy1)*I3(i,1,k)+I3(i,2,k))/(dy2*dy2/2+dy1*dy2/2));
 end
end

%main matrix
for i=2:(m-1)
  for j=2:(n-1)
    for k=2:(o-1)
    I3(i,j,k)=I3(i,j,k)+(a*dt)/(dx3*dx3)*(I3(i+1,j,k)+I3(i-1,j,k)-
4*I3(i,j,k)+I3(i,j+1,k)+I3(i,j-1,k))+(a*dt)/(dz3*dz3)*(I3(i,j,k+1)+I3(i,j,k-1)-
2*I3(i,j,k));
    end
  end
end
```

```
%connecting I3 and I4
for i=2:(m-1)
 for k=2:(o-1)
  I3(i,n,k)=I3(i,n,k)+(a*dt)/(dx3*dx3)*(I3(i+1,n,k)+I3(i-1,n,k)-
2*I3(i,n,k))+(a*dt)/(dz3*dz3)*(I3(i,n,k+1)+I3(i,n,k-1)-
2*I3(i,n,k))+(a*dt)/(dx3*dx3)*(I3(i,n-1,k)+I4(floor((i+1)/3)+1,1)-2*I3(i,n,k));
 end
end
```

%This function calculates new temperature distribution
%after one time step for matrix I4.

```
function I4=fd34(I3,I4,dt,dx3,dx4,a,my1,my2,dback,Tinf,kbal,thickness,gc,tkb);

[m,n]=size(I4);
[m1,n1,o1]=size(I3);
```

% evaluating the heat flow.

%Heat loss to backing. Considering 1-D heat transfer,
%2x5mm grid, grid1=I1(i,j,o-1), grid2=Tinf.

```
if dback>(my1+my2*2+2*n1)
 if n<(dback-n1-my1)/6
   counter=n;
 else
   counter=round((dback-n1-my1)/6);
   if counter>n
     counter=n;
   end
 end

 for i=1:m
   for j=1:counter
     I4(i,j)=I4(i,j)+-(kbal*(I4(i,j)-
Tinf)/(thickness/2+tkb)*dx4^2*dt)/(gc/1e9*dx4^2*thickness);
   end
 end
end
```

%setting boundary values.

```
for j=1:(n-1)
  I4(1,j)=I4(2,j);
  I4(m,j)=I4(m-1,j);
end
for i=1:m
  I4(i,n)=I4(i,n-1);
end


%connecting I3 and I4
dy1=dx3/2+dx4/2;
dy2=dx4;
for i=2:(m-1)
  Tsum=0;
  for p=1:3
    Tsum=Tsum+I3((i-1)*3-1,n1,p+1)+I3((i-1)*3,n1,p+1)+I3((i-1)*3+1,n1,p+1);
  end
  I4(i,1)=I4(i,1)+(dt*a)/(dx4*dx4)*(I4(i-1,1)-
2*I4(i,1)+I4(i+1,1))+(dt*a)*((dy2/dy1*Tsum/9-
(1+dy2/dy1)*I4(i,1)+I4(i,2))/(dy2*dy2/2+dy1*dy2/2));
end


for i=2:(m-1)
 for j=2:(n-1)
 I4(i,j)=I4(i,j)+(a*dt)/(dx4*dx4)*(I4(i+1,j)+I4(i-1,j)-4*I4(i,j)+I4(i,j+1)+I4(i,j-1));
 end
end
```

%Program used in the main program for saving data at the positions specified.

```
if pos2==0 & teller==grid
  rootname = 'c:\data\v5d20case\v5d20case';
% Root filename
  extension = '.mat';    % Extension for the files
  filename = [rootname, int2str(num), extension];
```

```
  eval(['save ', filename]);
  num=num+1;
end

if pos2>0
  rootname = 'c:\data\v5d20case\v5d20case';    % Root filename
  extension = '.mat';    % Extension for the files
  filename = [rootname, int2str(num), extension];
  eval(['save ', filename]);
  num=num+1;
end
```

Additional programs/functions/procedures

```
%make3di.m
%Makes the variable "I", a 3D matrix of plate obtained by connecting I1-I4, here
%dx=dy=dz=1, no boundary values.
%NOTE! dx1=dy1=dz1=1, dx2=dy2=2 dz2=1, dx3=dy3=dz3=2, dx4=dy4=6 else
%fatal error.

clear newI1;
clear newI2;
clear newI3;
clear newI4;
clear I;
[l1,w1,t1]=size(I1);
[l2,w2,t2]=size(I2);
[l3,w3,t3]=size(I3);
[l4,w4]=size(I4);

newI1=zeros(l1-2,w1-1,t1-2);
newI2=zeros((l2-2)*2,w2*2,t2-2);
newI3=zeros((l3-2)*2,w3*2,(t3-2)*2);
newI4=zeros((l4-2)*6,(w4-1)*6,thickness);

[l1,w1,t1]=size(newI1);
[l2,w2,t2]=size(newI2);
```

```
[l3,w3,t3]=size(newI3);
[l4,w4,t4]=size(newI4);

for i=1:l1
  for j=1:w1
    for k=1:t1
      newI1(i,j,k)=I1(i+1,j+1,k+1);
    end
  end
end

for i=1:l2
  for j=1:w2
    for k=1:t2
      newI2(i,j,k)=I2(round(i/2)+1,round(j/2),k+1);
    end
  end
end

for i=1:l3
  for j=1:w3
    for k=1:t3
      newI3(i,j,k)=I3(round(i/2)+1,round(j/2),round(k/2)+1);
    end
  end
end

for i=1:l4
  for j=1:w4
    for k=1:thickness
      newI4(i,j,k)=I4(floor((i-1)/6)+2,floor((j-1)/6)+1);
    end
  end
end

I=zeros(length,width/2,thickness);
```

```
for i=1:l1
  for j=1:w1
    for k=1:t1
      I(i,j,k)=newI1(i,j,k);
    end
  end
end

for i=1:l2
  for j=1:w2
    for k=1:t2
      I(i,j+w1,k)=newI2(i,j,k);
    end
  end
end

for i=1:l3
  for j=1:w3
    for k=1:t3
      I(i,j+w1+w2,k)=newI3(i,j,k);
    end
  end
end

for i=1:l4
  for j=1:w4
    for k=1:t4
      I(i,j+w1+w2+w3,k)=newI4(i,j,k);
    end
  end
end
```

% Smoothening of matrix I, through I1,I2 and I3.

```
function Iglatt=glatt3d(I,my1,my2,my3,my4,length);
Iglatt=I;
[l,w,t]=size(I);

for i=1:l
  for j=1:my2/2
    for k=1:t
      Iglatt(i,j*2+my1,k)=(Iglatt(i,j*2+my1-1,k)+Iglatt(i,j*2+my1+1,k))/2;
    end
  end
end

for i=1:l
  for j=1:my3/2
    for k=1:t
      Iglatt(i,j*2+my1+my2,k)=(Iglatt(i,j*2+my1-
1+my2,k)+Iglatt(i,j*2+my1+1+my2,k))/2;
    end
  end
end

for i=1:length/2-1
  for j=my1:my1+my2+my3
    for k=1:t
      Iglatt(i*2,j,k)=(Iglatt(i*2-1,j,k)+Iglatt(i*2+1,j,k))/2;
    end
  end
end
```

% This function makes a variable containing all the thermal data calculated for one
%case.

```
function Ttot=Thisttot(files,sti,my1,my2,my3,my4,length);
%Load data from generated files.
%Ttot=Thisttot(files,sti,my1,my2,my3,my4,length);
extension = '.mat';    % Extension of the files
for data = 1:files
  variable = [sti, int2str(data)];
  filename = [variable, extension];
  eval(['load ', filename]);
  make3di;
  Ttot{1,data}=glatt3d(I,my1,my2,my3,my4,length);
end


function [sycle,time]=Tsycle(Thist,xpos,ypos,zpos,dts);
%This function collects thermal history on the basis of a Ttot variabel.
%[sycle,time]=Tsycle(Thist,xpos,ypos,zpos,dts);

[m,n]=size(Thist);

sycle=zeros(1,n);
time=zeros(1,n);
for i=1:n
  sycle(i)=Thist{1,i}(xpos,ypos,zpos);
  time(i)=(i-1)*dts;
end
plot(time,sycle);
```

%This function makes a contour plot of the matrix in the x-y plane.

```
function xyplot(Ttot,pos,d,ux,uy,plan,V)
[x,y,z]=size(matr);
test=zeros(ux,uy);
for i=1:ux
   for j=1:uy
      test(i,j)=matr(i+pos-d/2-round(ux*2/3),j,plan);
   end
end
tester=zeros(ux,2*uy);

for i=1:ux
   for j=1:uy
      tester(i,j)=test(i,uy-j+1);
      tester(i,j+uy)=test(i,j);
   end
end


for i=1:ux
   X(i)=-1*round(ux*2/3)+i;
end

for i=1:2*uy
   Y(i)=-uy+i;
end

C=contourf(X,Y,tester',V);
contourf(X,Y,tester',V);
clabel(C);
xlabel('x-position');
ylabel('y-position');
grid;
```

```
%This function makes a contour plot of the matrix in the x-z plane.
function xzplot(Iglatt,pos,d,V)
%input : Iglatt- smoothened matrix, heat source front position (pos), tool
%diameter (d).

[x,y,z]=size(Iglatt);
tester=zeros(x,z);
for i=1:x
   for j=1:z
      tester(i,j)=Iglatt(i,1,j);
      %tester(i,j)=Ttot{1,110}(i,1,j);
   end
end

plot=zeros(z,x);

for i=1:x
   for j=1:z
      plot(j,i)=tester(i,z-j+1)';
   end
end

for i=1:x
   X(i)=-1*pos+d/2+i;
end
Xaks=-20:2:14;

Y=[0 1.5 2.5 3.5 4.5 6];
C=contourf(X,Y,plot,V);
contourf(X,Y,plot,V);
clabel(C);
axis([-20 15 0 35]);
set(gca,'ytick',[1 2 3 4 5 6]);
set(gca,'xtick',Xaks);
xlabel('x-position');
ylabel('z-position');
grid;
```

%This function makes a plot of the y-z plane at the %specified x pos.

```
function yzplot(matrix,pos,V,valg)
[x,y,z]=size(matrix);
Mplot=zeros(z,y);


 for j=1:y
   for k=1:z
     Mplot(z-k+1,j)=matrix(pos,j,k);
   end
 end

if valg==1
 Z(1)=0;
 Z(2)=Z(1)+1.5;
 for i=3:z-1
   Z(i)=Z(i-1)+1;
 end
 Z(z)=Z(z-1)+1.5;

 Y(1)=0;
 Y(2)=1.5;
 for j=3:y
   Y(j)=Y(j-1)+1;
 end
 contourf(Y,Z,Mplot);
 cs = contourf(Y,Z,Mplot);
 clabel(cs);
 grid;
 title('FSW');
 ylabel('z-position [mm]');
 xlabel('y-position [mm]');
 axis([0 20 0 20]);
end
```

```
if valg==2
  M2plot=zeros(z,2*y);
  for i=1:z
    for j=1:y
      M2plot(i,j)=Mplot(i,y-j+1);
    end
  end
  for i=1:z
    for j=y+1:2*y
      M2plot(i,j)=Mplot(i,j-y);
    end
  end
  X(1)=0;
  X(2)=X(1)+1.5;
  for i=3:z-1
    X(i)=X(i-1)+1;
  end
  X(z)=X(z-1)+1.5;

  Y(1)=-1*y+0.5;
  for j=2:2*y
    Y(j)=Y(j-1)+1;
  end

  for j=1:2*y
    Mlin(j)=M2plot(2,j);
  end
  plot(Y,Mlin)
  pause

  xt=-20:2:20;
  contourf(Y,X,M2plot,V);
  cs = contourf(Y,X,M2plot,V);
  clabel(cs);
  axis([-20 20 -20 20]);
  set(gca,'ytick',[0 2 4 6]);
  set(gca,'xtick',xt);
```

```
  grid;
  ylabel('z-position [mm]');
  xlabel('y-position [mm]');
end


%This function makes a peak temperature contour plot, and stores the isotherm
%widths in the 'isoplot' variable.
function isoplot=isow(Iglatt,valg);

%valg=1, plot of matrix
%valg=2, plot of double matrix

[m,n,o]=size(Iglatt);
clear plottemp;
clear isowidth;
clear isoplot;

%Temperatures contoured.
plottemp(1)=550;
plottemp(2)=500;
plottemp(3)=450;
plottemp(4)=400;
plottemp(5)=350;
plottemp(6)=300;
plottemp(7)=250;
plottemp(8)=200;
plottemp(9)=150;
plottemp(10)=100;


isowidth=zeros(o,10);
isoplot=zeros(o,n);

for i=1:m
  for k=1:o
    for j=1:n
```

```
        if isoplot(o+1-k,j)<Iglatt(i,j,k)
            isoplot(o+1-k,j)=Iglatt(i,j,k);  %Estimates %max.values in x-direction.
        end
      end
    end
end


if valg==1
   Y(1)=0;
   Y(2)=1.5
   for k=3:o-1
     Y(k)=Y(k-1)+1;
   end
   Y(o)=Y(o-1)+1.5;
   X(1)=0;
   X(2)=1.5
   for j=3:n
     X(j)=X(j-1)+1;
   end
   V=plottemp;
   contourf(X,Y,isoplot,V);
   cs = contourf(X,Y,isoplot,V);
   clabel(cs);
   grid;
   title('FSW');
   ylabel('depth[mm]');
   xlabel('length[mm]');
end

if valg==2
  [x,y]=size(isoplot);
  isoplot2=zeros(x,y*2);

  for i=1:x
    for j=1:y
    isoplot2(i,j)=isoplot(i,y-j+1);
```

```
      end
    end

  for i=1:x
    for j=y+1:2*y
      isoplot2(i,j)=isoplot(i,j-y);
    end
  end

  X(1)=0;
  X(2)=X(1)+1.5;
  for i=3:x-1
    X(i)=X(i-1)+1;
  end
  X(x)=X(x-1)+1.5;

  Y(1)=-1*y+0.5;
  for j=2:2*y
    Y(j)=Y(j-1)+1;
  end

  xt=-20:2:20;
  V=plottemp;
  contourf(Y,X,isoplot2,V);
  cs = contourf(Y,X,isoplot2,V);
  clabel(cs);
  axis([-20 20 0 40]);
  set(gca,'ytick',[0 1 2 3 4 5 6]);
  set(gca,'xtick',xt);
  grid;
  title('FSW');
  ylabel('z-position [mm]');
  xlabel('y-position [mm]');
end
```

Part IV: IN-SITU THERMOCOUPLE MEASURMENTS OF THE TEMPERATURE DISTRIBUTION IN FSW

4.1 Introduction

In order to obtain quantitative information about the HAZ thermal program during friction stir welding, bead on plate welds were made on 7108-T79 and 6082-T6 plates under different operating conditions. The experimental work was carried out at Hydro Aluminium, R&D Materials Technology, Karmøy, Norway.

4.2 Experimental Programme

The welds were made using a dedicated FSW machine at Hydro Aluminium. The thermal data were obtained using Campell Scientific 21X data logger with a capacity of eight type K (Chromel-Alumel) thermocouples. The data logger was controlled by a portable PC. After welding the plates were sectioned to determine the exact position of the thermocouples referred to the centre-line of the tool shoulder. At the same time the hardness profiles across the HAZ were measured at specific time intervals on both sides of the weld to quantify the response of the materials to the imposed thermal cycles. The Vickers hardness measurements were carried out with a Matsuzawa DVK-1S instrument operating at a constant load of 1 kg.

4.2.1 HAZ thermal histories

Eight holes, each of 3 mm depth, were drilled from the top side of the 6 mm thick plates. The thermocouples were inserted into the holes at the positions illustrated in Figure 1, using a copper paste to improve the contact between the thermocouple and the plate. The operating conditions used in the friction stir welding experiments are summarised in Table 1.

The data were recorded using an execution interval of 0.6 seconds for the data logger. Comments on each experiment are summarised in Appendix 4.1.
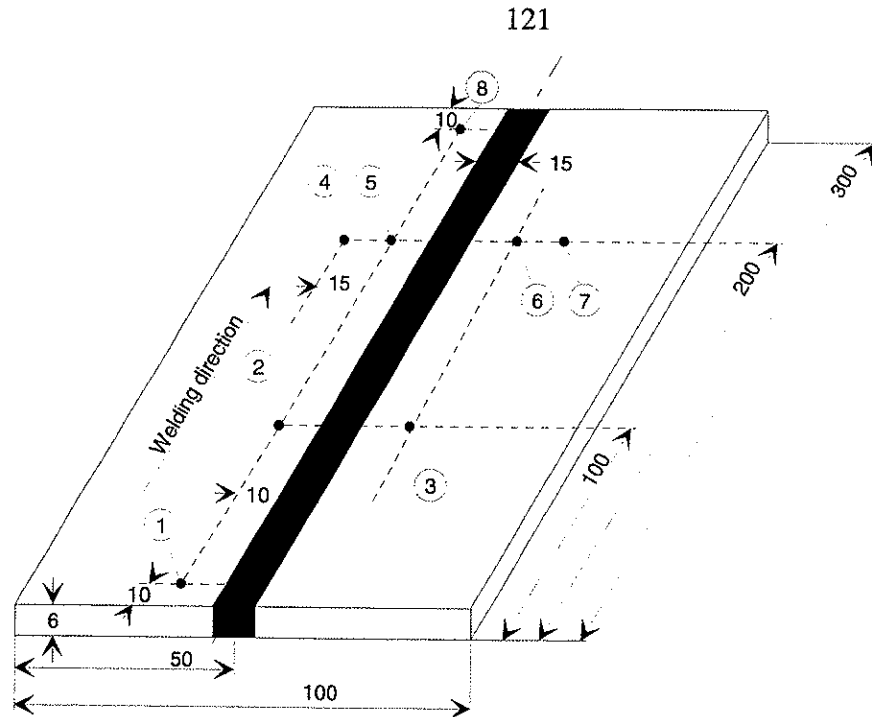
Figure 1 Positions of the thermocouples in the plate.

Table 1 Operating conditions used in the HAZ thermal measurements.

Series No	Alloy	Welding force [N]	Rotational speed [RPM]	Welding speed [mm/s]
1	6082-T6	6000	1500	5
2	6082-T6	6000	1500	8
3	6082-T6	6000	1500	8
4	6082-T6	6000	1500	12
5	7108-T79	6000	1500	5
6	7108-T79	6000	1500	8
7	7108-T79	6000	1500	8
8	7108-T79	6000	1500	12

4.2.2 Thermal conditions close to the deformed material

Separate sets of experiments were also carried out to obtain quantitative information about the thermal conditions close to the deformed material. Eight holes with depths varying from 4.5-5.75 mm were drilled from the backside of

the plate. The thermocouples were inserted at the positions illustrated in Figure 2, and a special copper paste was used to improve the contact between thermocouple and plate. Data was recorded using an execution interval of 0.1 seconds for the data logger. The operating conditions are summarised in Table 2. Comments on each experiment are summarised in Appendix 4.2.

Table 2 Operating conditions used in the supplementary FSW experiments.

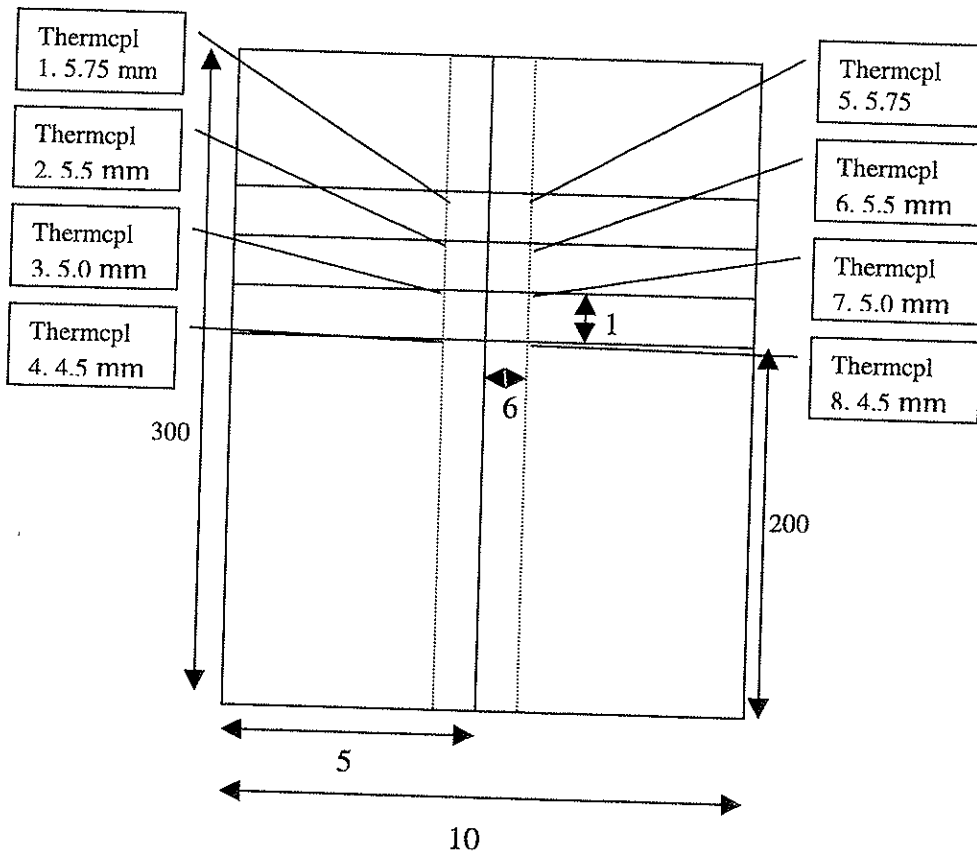| Series No	Alloy	Welding force [N]	Rotational speed [RPM]	Welding speed [mm/s]
9	6082-T6	6000	1500	8
10	7108-T79	6000	1500	8
11	6082-T6	6000	1500	8
12	7108-T79	6000	1500	8

Figure 2 Mounting of thermocouples from the backside of plate.

4.3 Results

4.3.1 HAZ Thermal Histories

In the following, plots of the recorded HAZ thermal cycles are shown for the positions indicated in Figure 1. Figure 3 shows a picture at site, where a plate is mounted with thermocouples ready for bead on plate welding. The plots in Figure 4 throughout Figure 19 contain the thermal histories for the combination of experimental conditions given in Table 1. Due to the force acting on the tool during welding, the position of the weld centre line is shifted towards the shear side of the weld. This leads to a corresponding displacement of the location of the thermocouples, which needs to be corrected for in the subsequent evaluation of the experimental data (see data in Table 3).
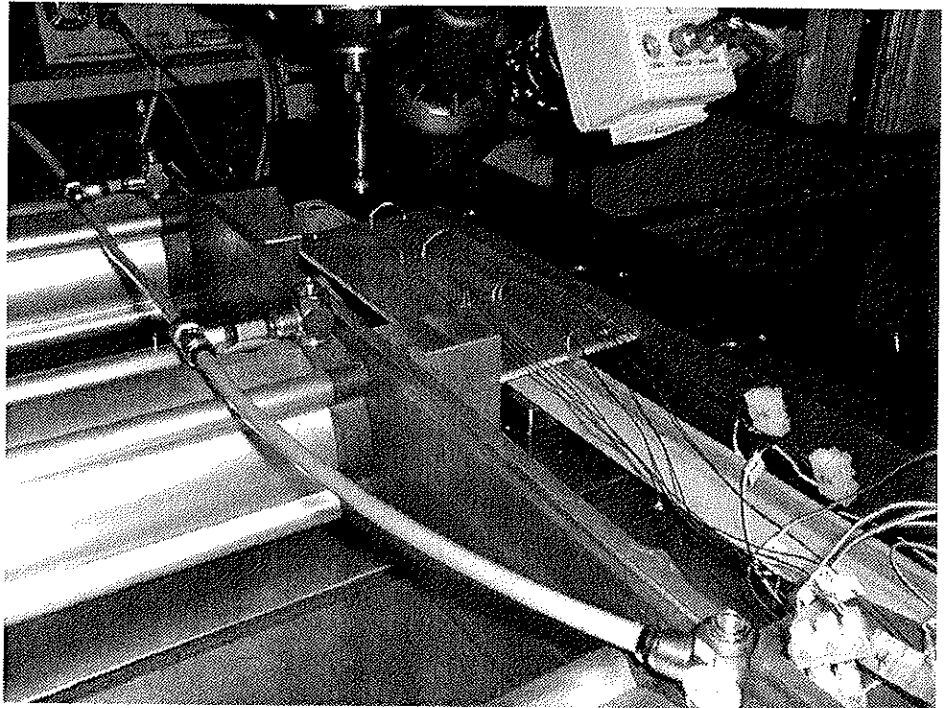

Figure 3 Photograph of the experimental set-up at Karmøy.

Table 3 Position of thermocouples referred to the centre of the plastic deformed material, (y-direction).

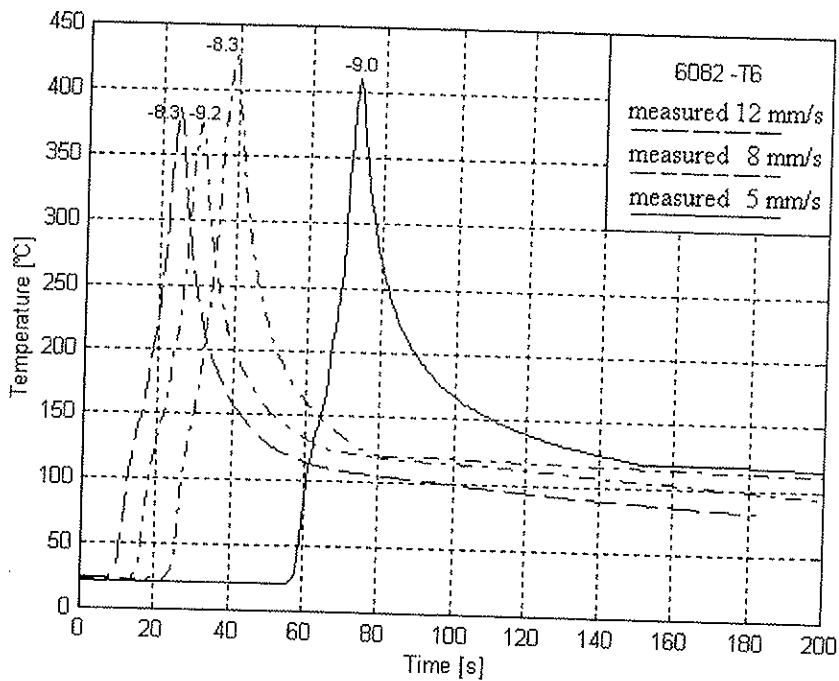| Position	plate1	plate2	plate3	plate4	plate5	plate6	plate7
1	-9.0	-9.2	-8.3	-8.3	-8.6	-8.6	-8.
2	-9.3	-10.0	-8.2	-9.3	-8.9	-9.0	-9.
3	11.4	11.3	11.9	11.2	9.8	11.3	10.
4	-14.9	-14.3	-16.6	-14.6	-14.1	-14.4	-14.
5	-9.3	-9.5	-11.3	-9.2	-8.9	-8.8	-9
6	11.0	10.9	8.2	10.9	11.0	10.6	10
7	15.5	15.6	13.3	16.3	15.7	16.0	15
8	-8.1	-9.0	-8.6	-9.3	-8.7	-9.3	-8

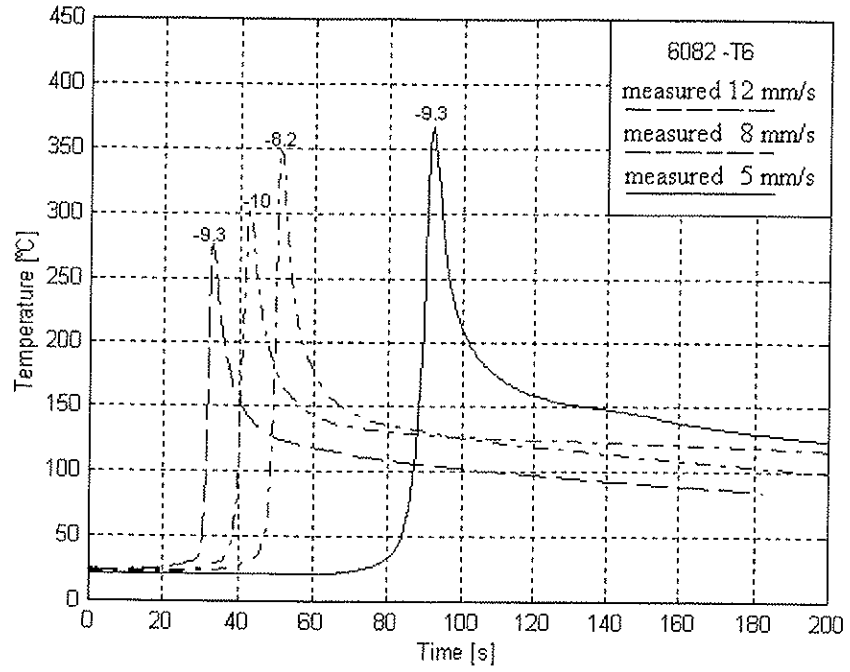Figure 4 Thermal histories in position 1, 6082-T6 plate 1-4, Appendix 4.1.

Figure 5 Thermal histories in position 2, 6082-T6 plate 1-4, Appendix 4.1.
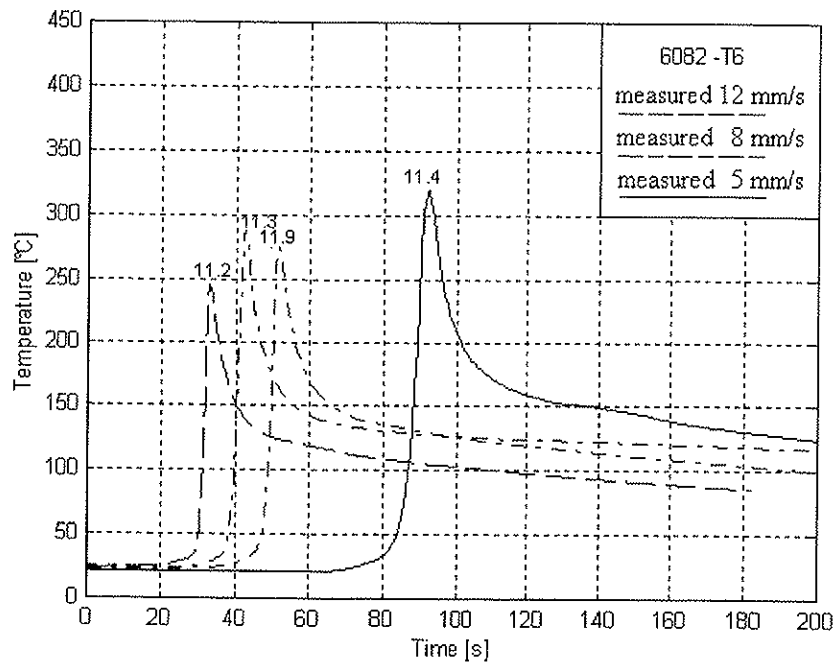

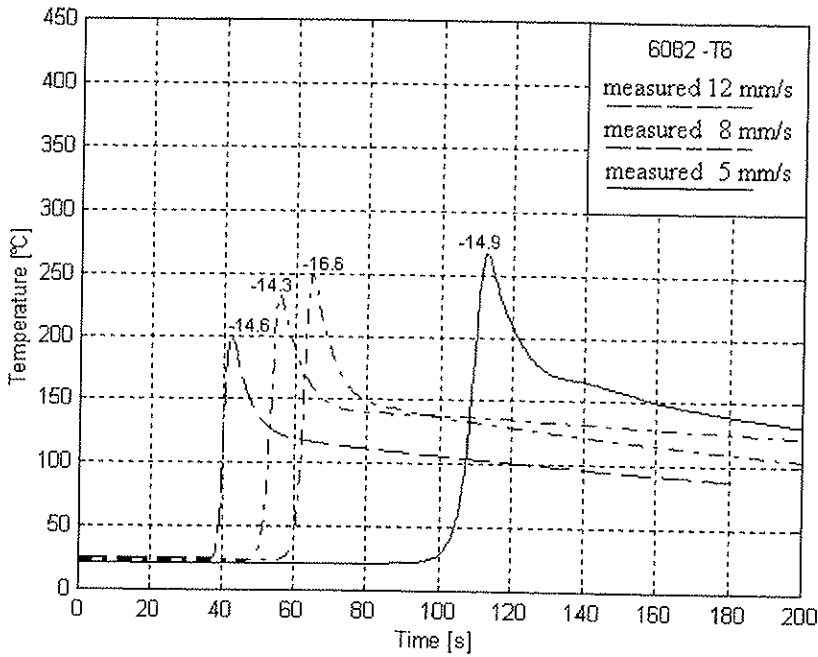Figure 6 Thermal histories in position 3, 6082-T6 plate 1-4, Appendix 4.1.

Figure 7 Thermal histories in position 4, 6082-T6 plate 1-4, Appendix 4.1.

Figure 8 Thermal histories in position 5, 6082-T6 plate1-4, Appendix 4.1, plate11 Appendix 4.2 (-9.5 $T_{max} \cong 300$).

Figure 9 Thermal histories in position 6, 6082-T6 plate1-4, Appendix 4.1.

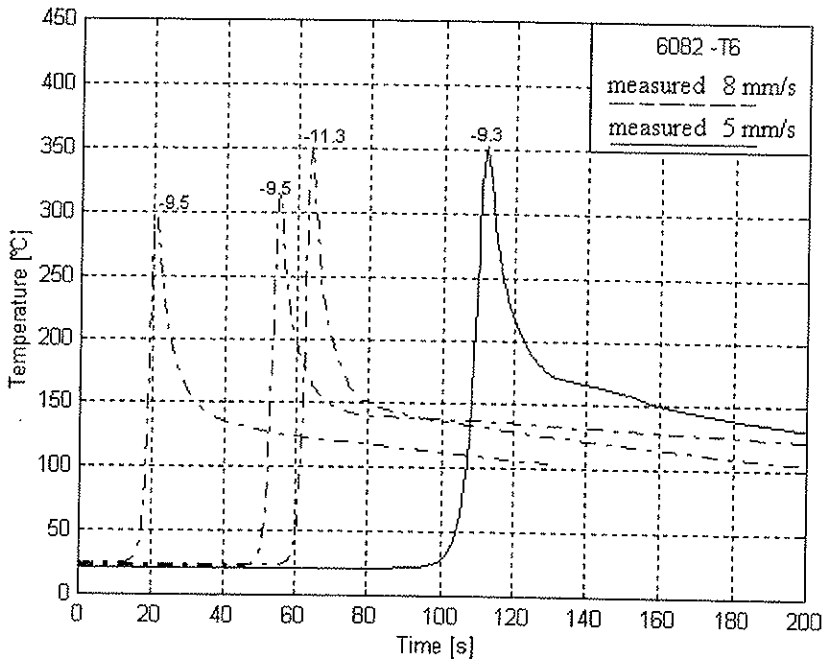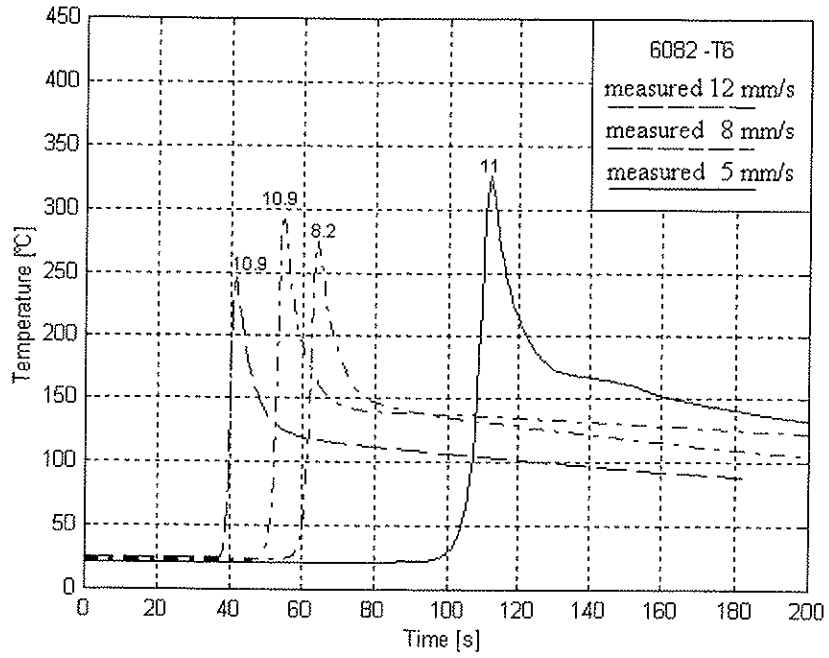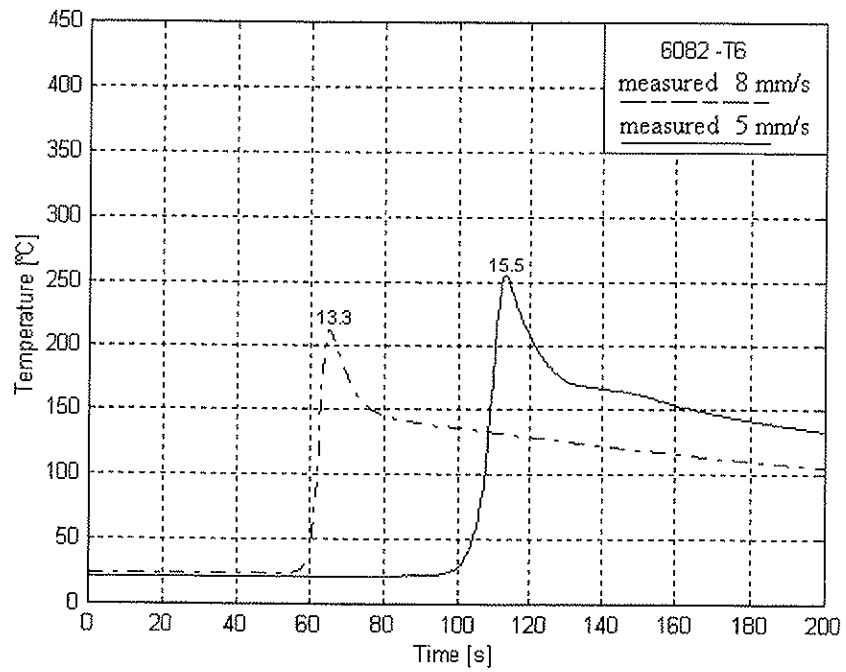Figure 10 Thermal histories in position 7, 6082-T6 plate 1-4, Appendix 4.1.

Figure 11 Thermal histories in position 8, 6082-T6 plate1-4, Appendix 4.1.

Figure 12 Thermal histories in position 1, 7108-T79 plate 5-8, Appendix 4.1.

Figure 13 Thermal histories in position 2, 7108-T79 plate 5-8, Appendix 4.1.

Figure 14 Thermal histories in position 3, 7108-T79 plate 5-8, Appendix 4.1.
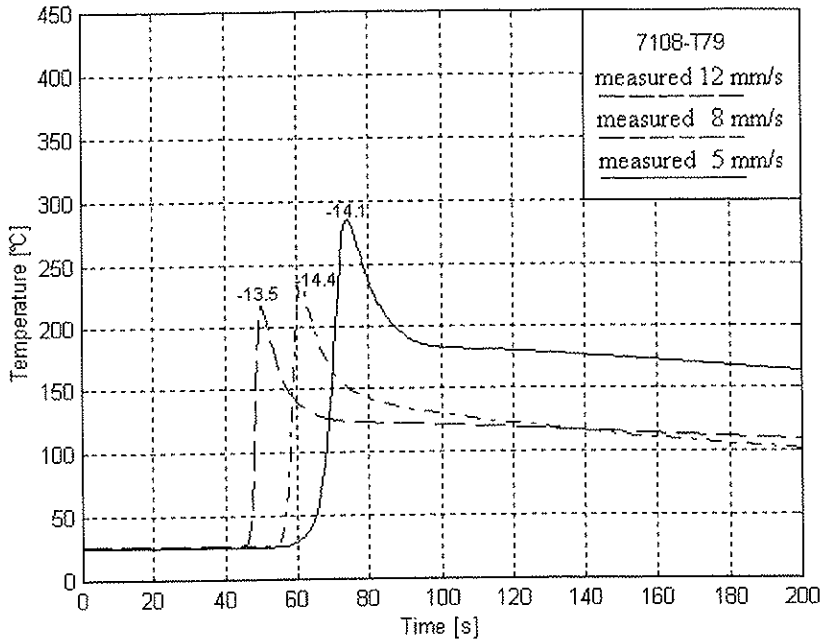
Figure 15 Thermal histories in position 4, 7108-T79 plate 5-8, Appendix 4.1.
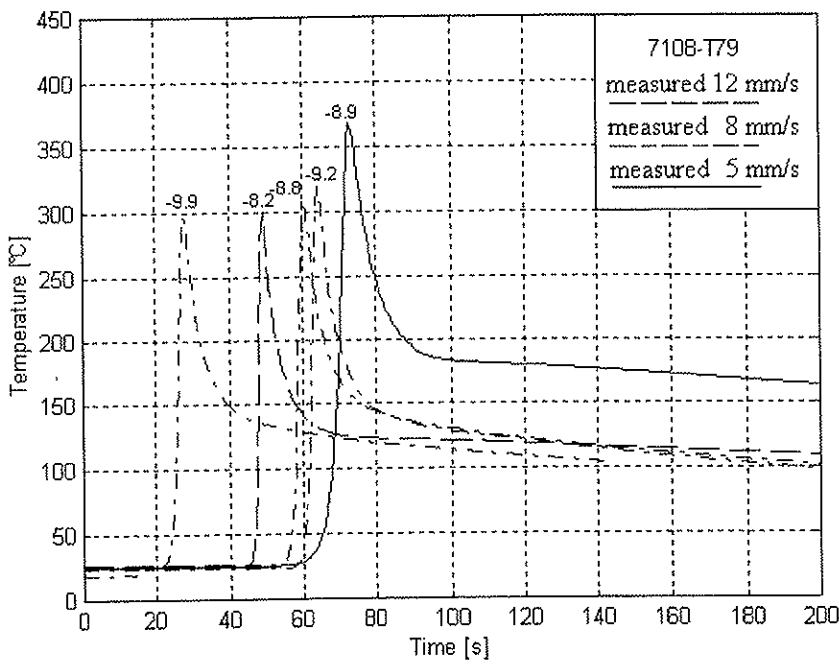
Figure 16 Thermal histories in position 5, 7108-T79 plate 5-8, Appendix 4.1, plate12 Appendix 4.2 (-9.9 $T_{max}\cong300$).
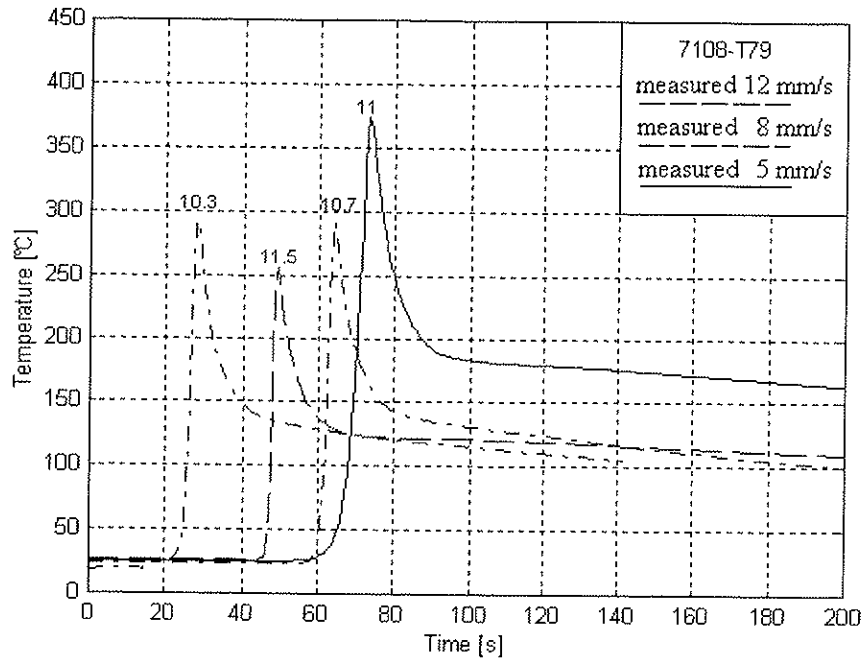
Figure 17 Thermal histories in position 6, 7108-T79 plate 5-8, Appendix 4.1, plate12 Appendix 4.2 (10.3 $T_{max}\cong300$).
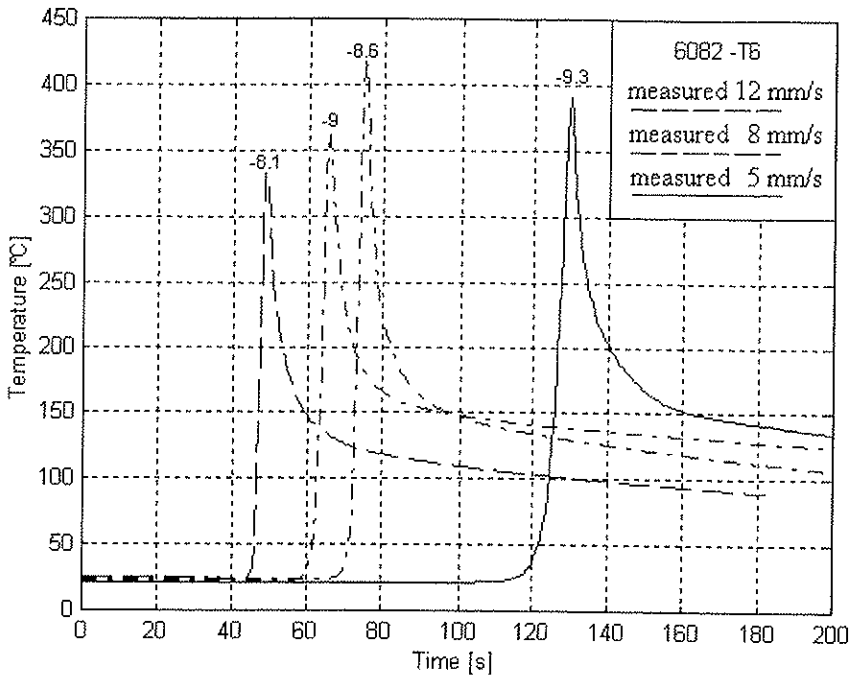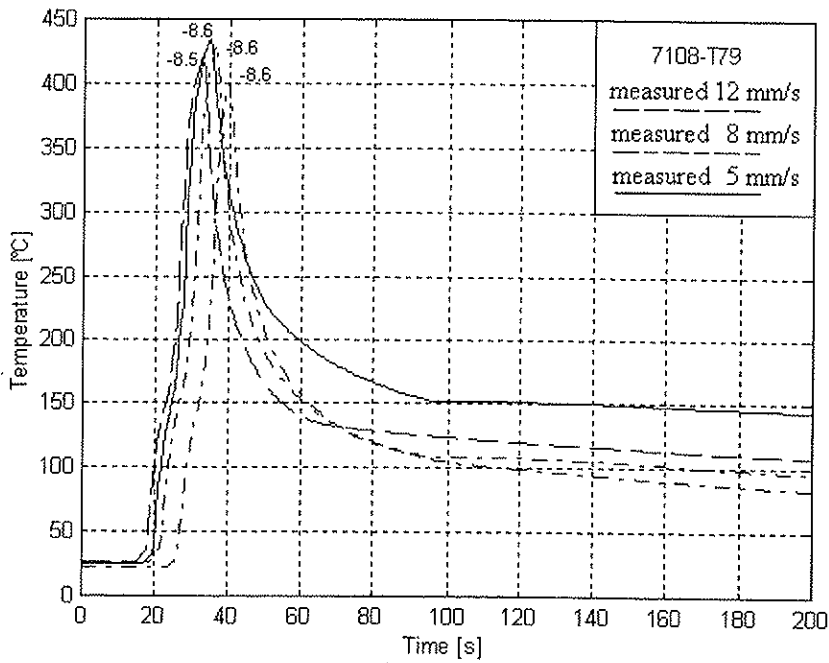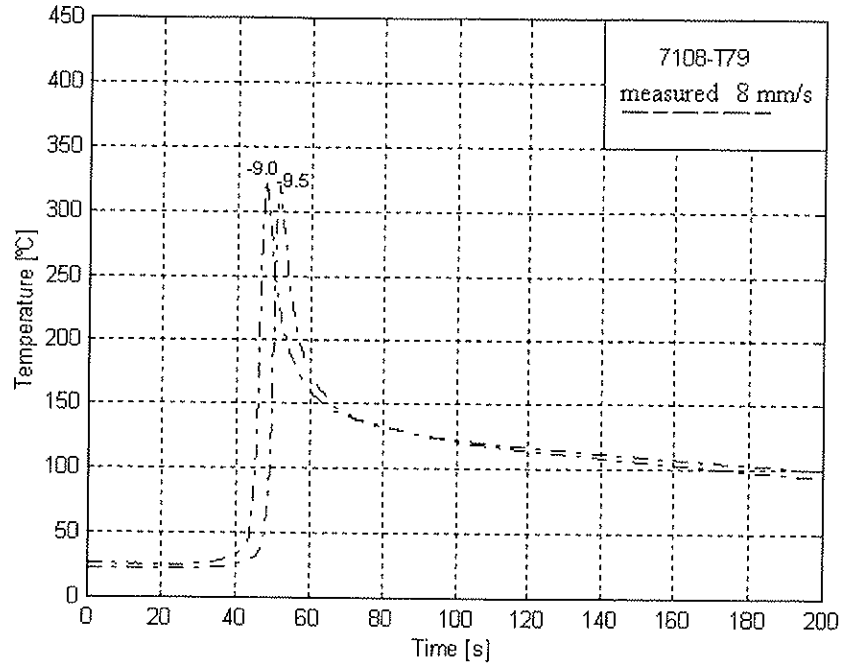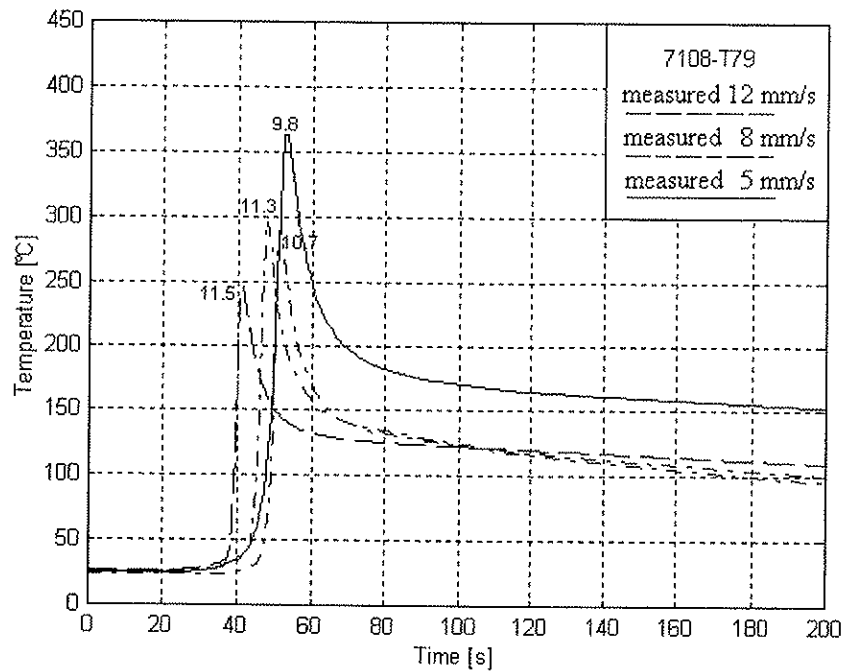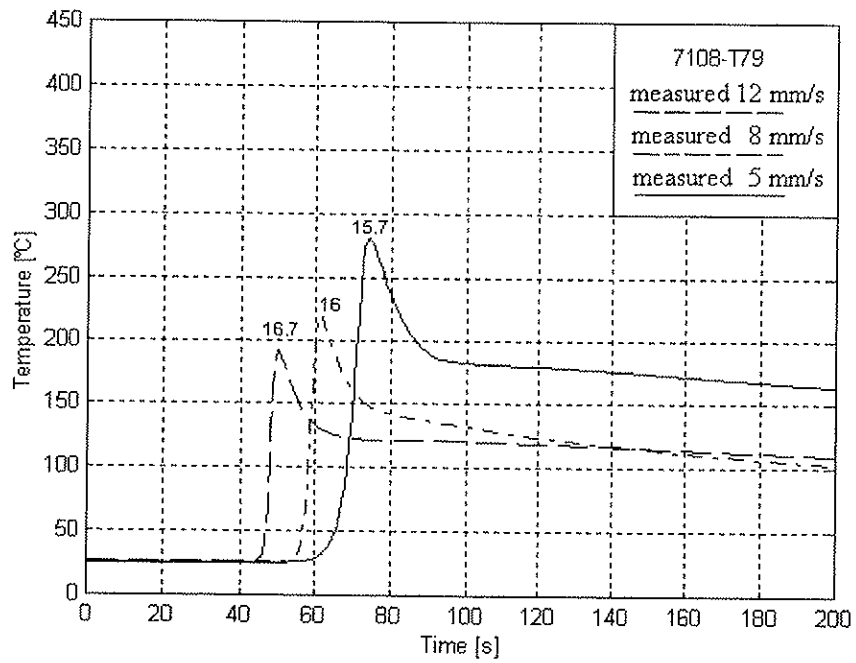

Figure 18 Thermal histories in position 7, 7108-T79 plate 5-8, Appendix 4.1.
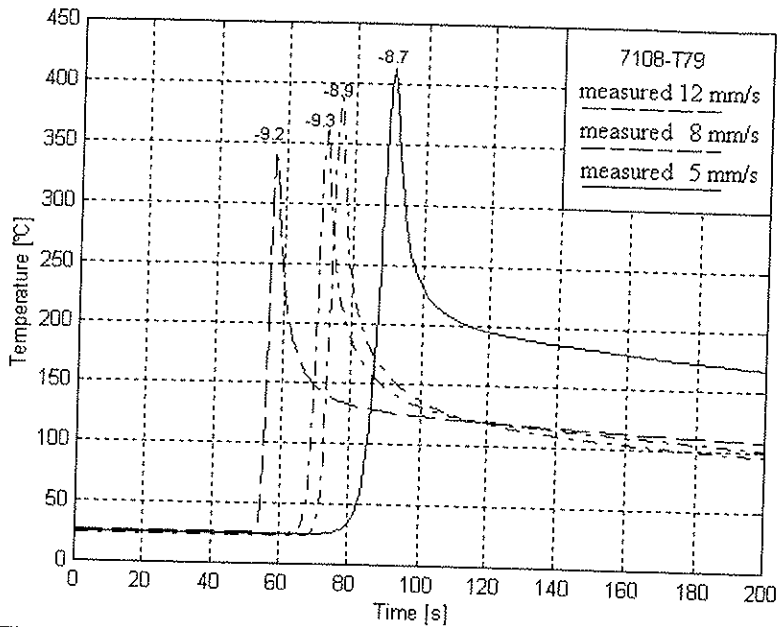
Figure 19 Thermal histories in position 8, 7108-T79 plate 5-8, Appendix 4.1.

4.3.2 Thermal programme within the deformed material

The results from the temperature measurements within the deformed material are summarised in Figure 21 throughout Figure 24. The actual positions of the thermocouples are given in Table 4, based on pictures obtained from metallographic examination, as illustrated in Figure 20. In addition, the measured peak temperatures of the thermal cycles are plotted against the thermocouple positions, as shown in Figure 25 and Figure 26.
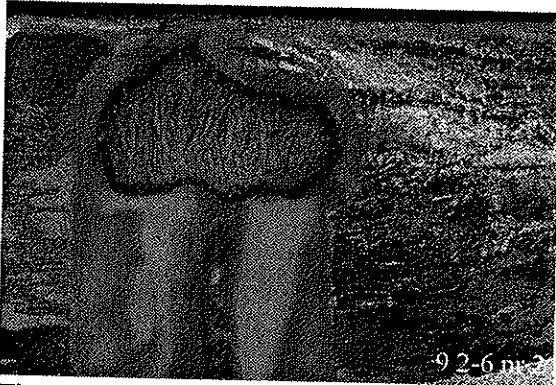
Figure 20 Photograph of thermocouple number 2 in plate 9.

Table 4 Actual position of thermocouples referred to the centre of the deformed zone.

Plate	Therm. cpl.	y-pos [mm]	z-pos [mm]	Tp	Therm. cpl.	y-pos [mm]	z-pos [mm]	Tp
9 (6082)	1	-	-	-	5	-4.6	-1.1	467.2
	2	6.5	-0.3	444.8	6	-5.0	-1.8	483.5
	3	-	-	-	7	-4.3	-2.3	464.3
	4	7.5	-1.6	372.8	8	-5.1	-2.0	444.5
10 (7108)	1	5.5	-0.8	416.3	5	-3.8	-2.0	512.4
	2	6.4	-0.4	454.9	6	-	-	-
	3	-	-	-	7	-3.8	-2.6	477.6
	4	5.8	-2.0	385.0	8	-	-	-
11 (6082)	1	-	-	-	5	-6.3	-0.6	469.5
	2	7.0	-0.5	427.7	6	-4.8	-0.6	492.7
	3	-	-	-	7	-5.5	-2.0	447.9
	4	5.8	-2.0	438.6	8	-4.5	-2.4	440.6
12 (7108)	1	7.0	-0.9	419.8	5	-	-	-
	2	-	-	-	6	-2.6	-1.9	516.8
	3	-	-	-	7	-2.5	-2.5	470.2
	4	7.3	-2.0	357.8	8	-3.0	-2.4	483.5
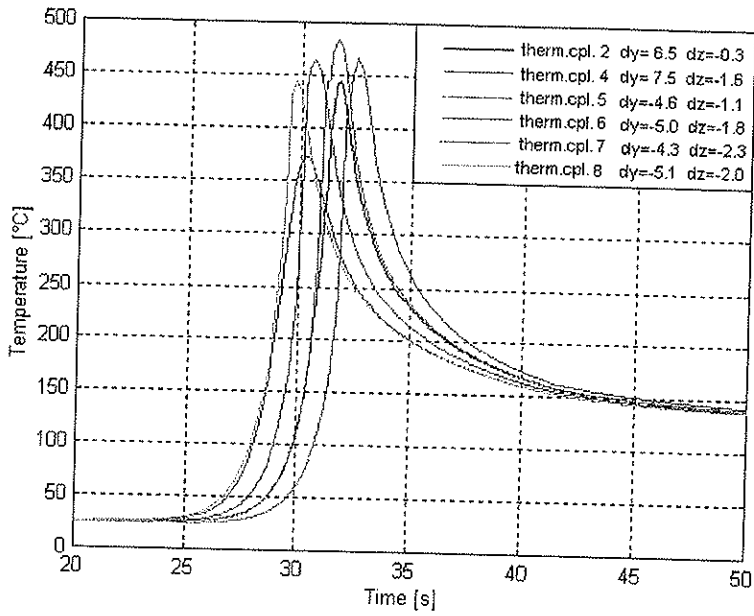
Figure 21 Thermal histories in plate 9, Appendix 4.2.
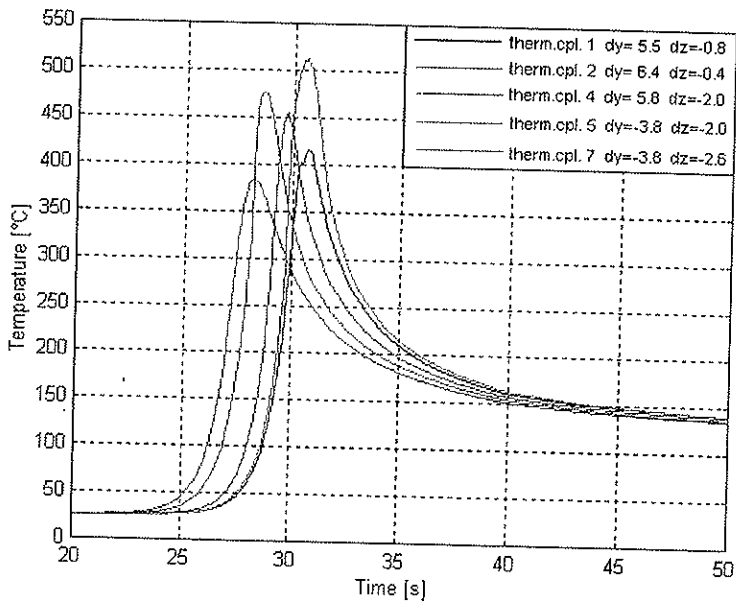
Figure 22 Thermal histories in plate 10, Appendix 4.2.
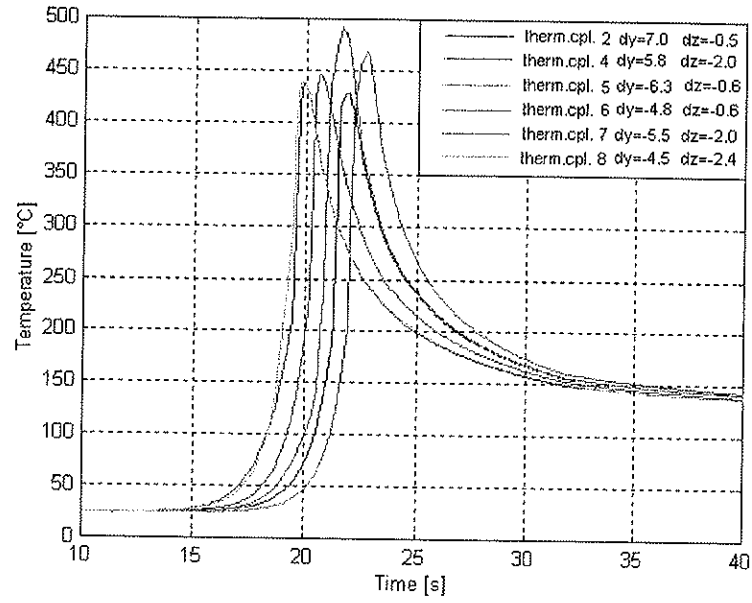
Figure 23 Thermal histories in plate 11, Appendix 4.2.
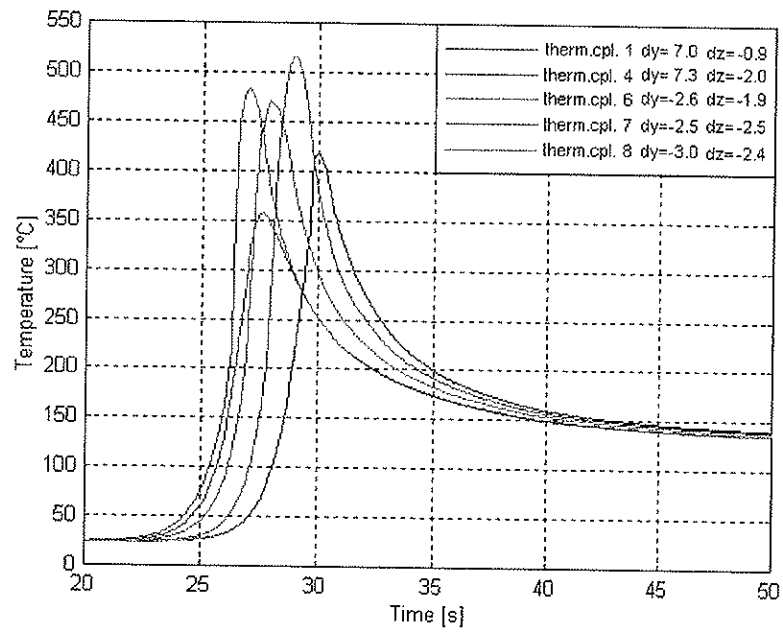
Figure 24 Thermal histories in plate 12, Appendix 4.2.
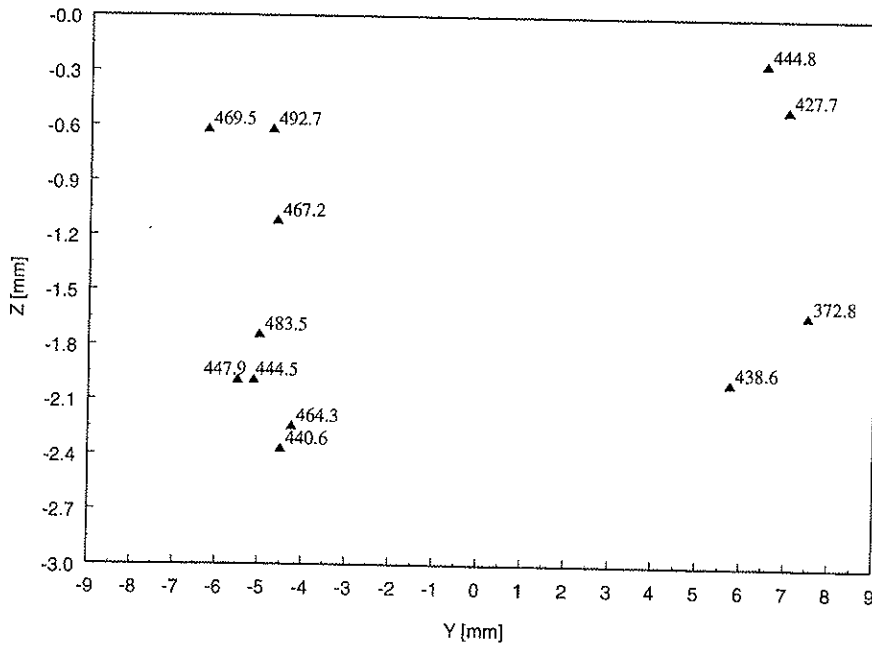
Figure 25 Measured peak temperatures in the transverse section of the weld for the 6082-T6 plates, Appendix 4.2.
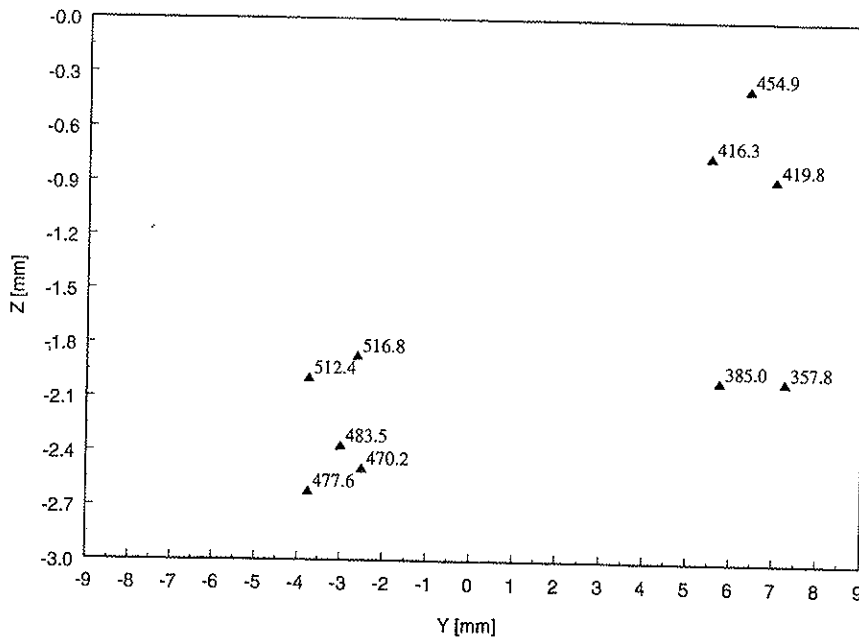
Figure 26 Measured peak temperatures in the transverse section of the weld for the 7108-T79 plates, Appendix 4.2.

4.3.3 HAZ hardness distribution

The following graphs show the hardness distribution in the cross section of the plates following FSW. Details are given in Appendix 4.1 (the sections corresponds to the thermocouple locations 4,5,6, and 7 in Figure 1).
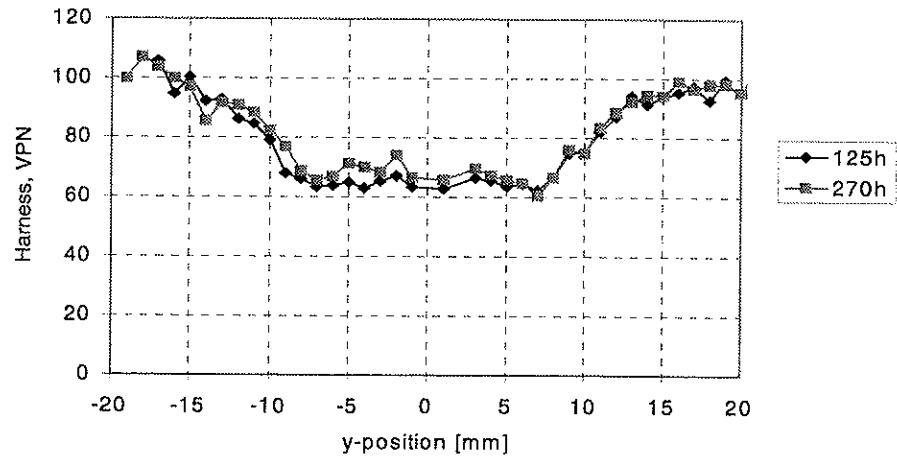
Figure 27 Hardness distribution in plate 1 (AA6082-T6), after 125 and 270 hours of natural ageing respectively, Appendix 4.1.
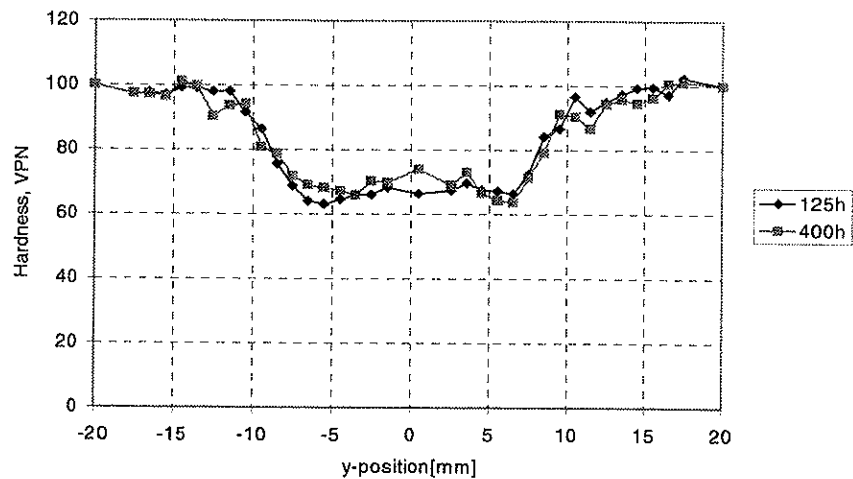
Figure 28 Hardness distribution in plate 2 (AA6082-T6), after 125 and 400 hours of natural ageing respectively, Appendix 4.1.
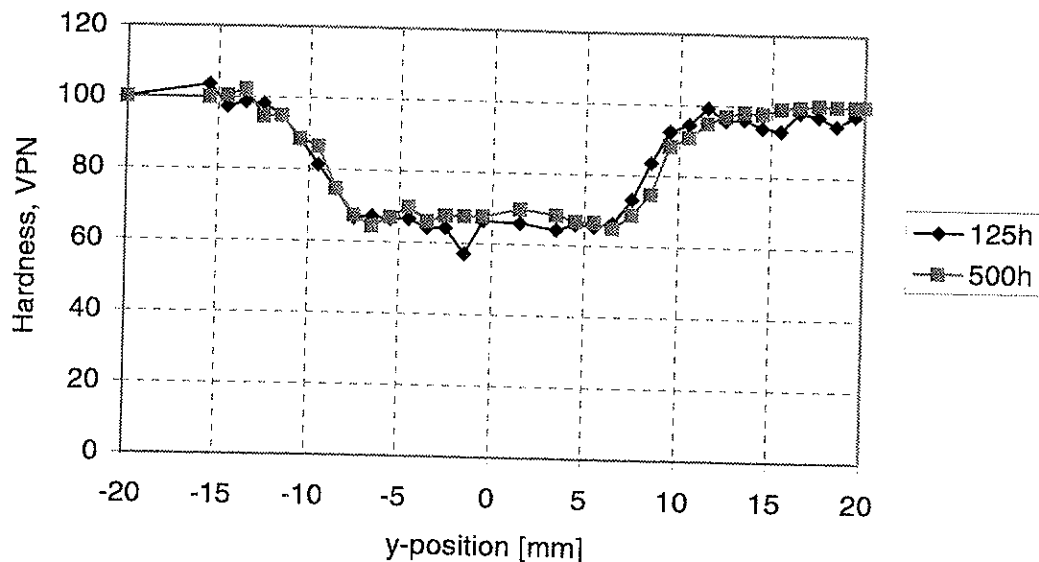
Figure 29 Hardness distribution in plate3 (AA6082-T6), after 125 and 500 hours of natural ageing respectively, Appendix 4.1.
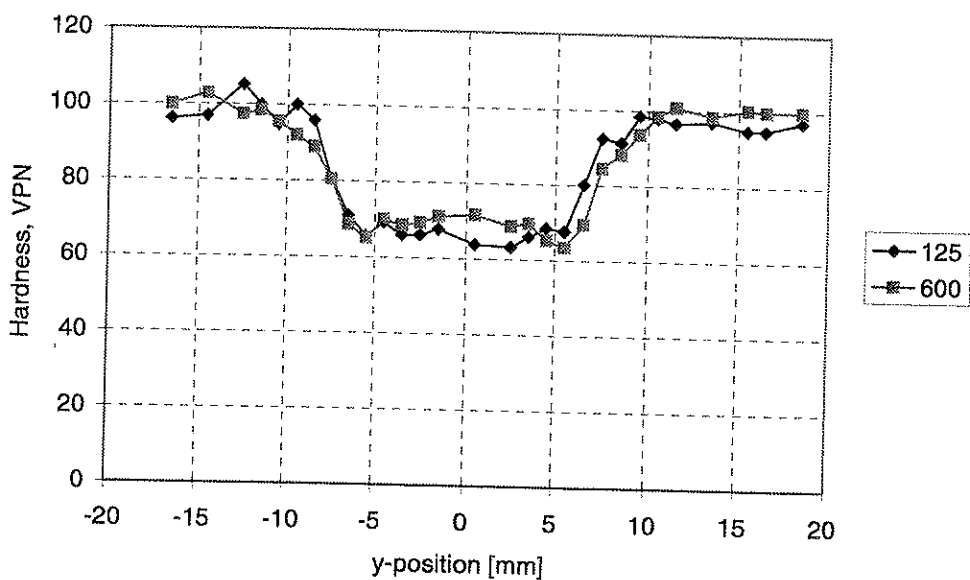
Figure 30 Hardness distribution in plate 4 (AA6082-T6), after 125 and 600 hours of natural ageing respectively, Apendix 1.
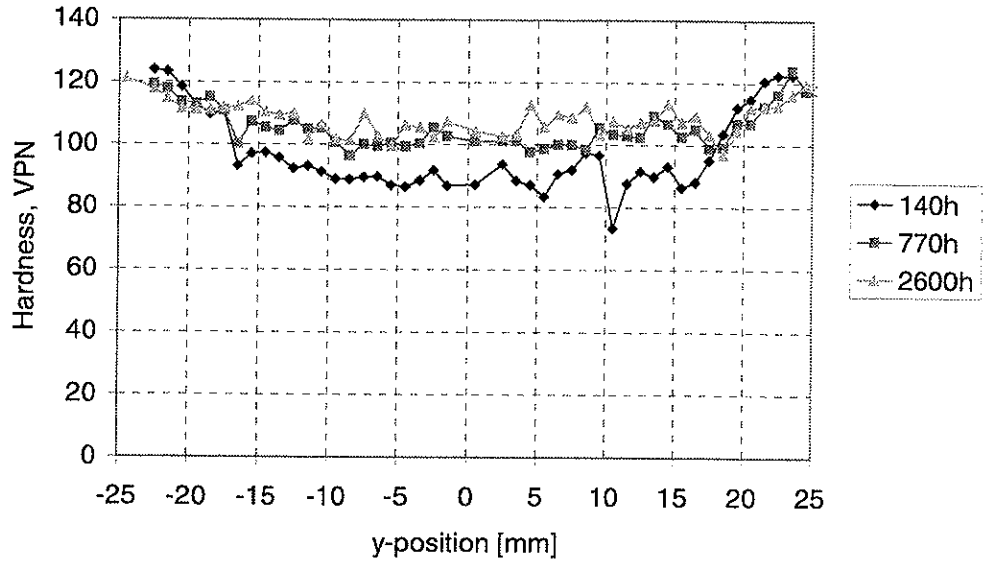
Figure 31 Hardness distribution in plate 5 (AA7108-T79), after 140, 770 and 2600 hours of natural ageing respectively, Appendix 4.1.
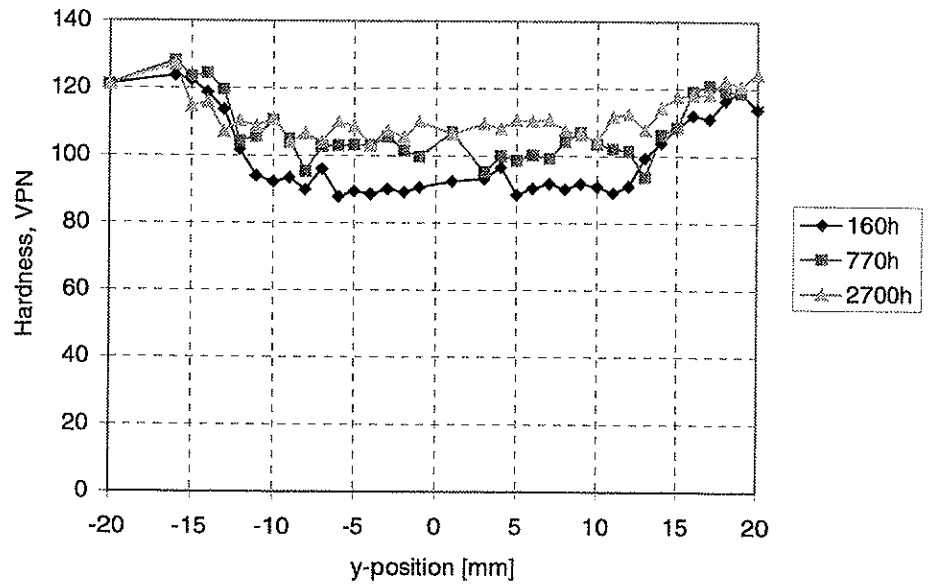
Figure 32 Hardness distribution in plate 6 (AA7108-T79), after 160, 770 and 2700 hours of natural ageing respectively, Appendix 4.1.
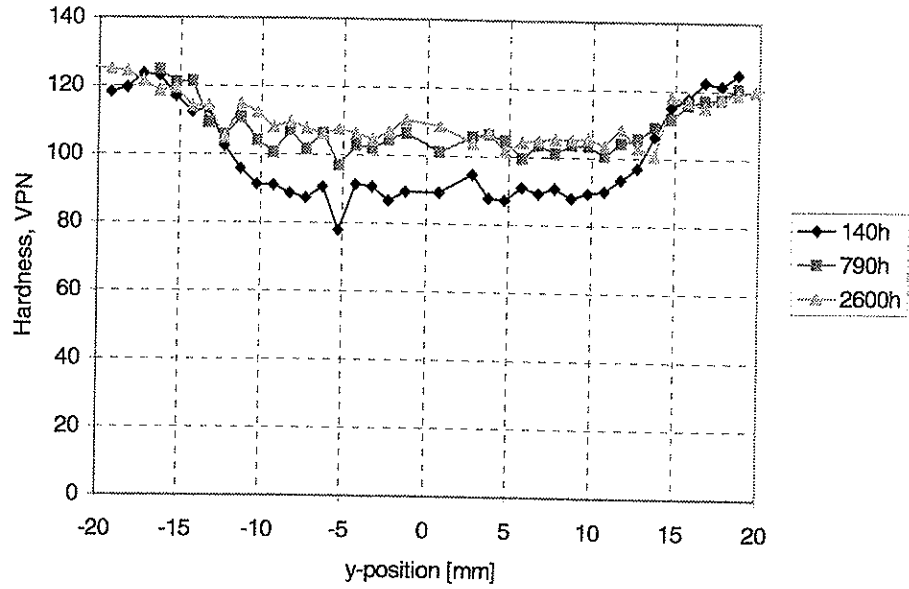
Figure 33 Hardness distribution in plate 7 (AA7108-T79), after 140, 790 and 2600 hours of natural ageing respectively, Appendix 4.1.
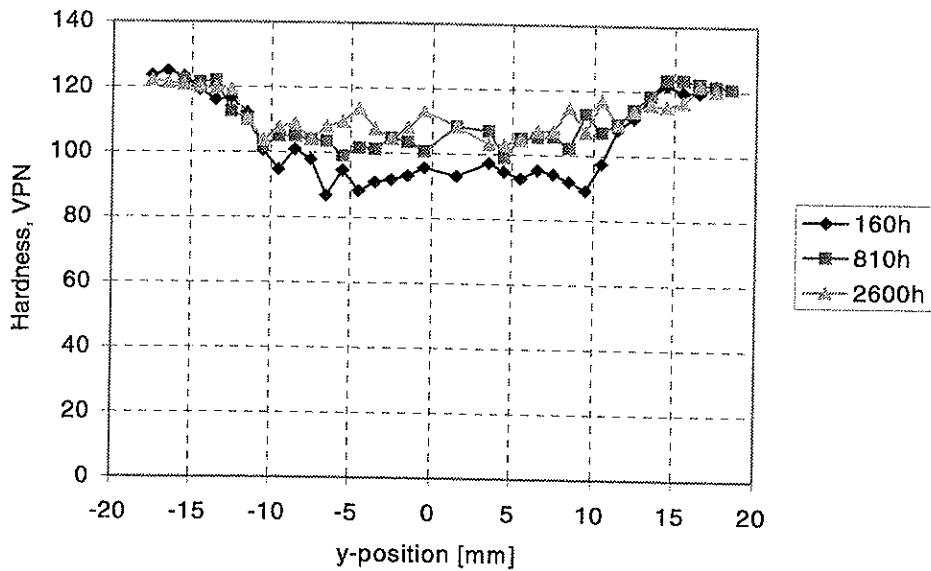
Figure 34 Hardness distribution in plate 8 (AA7108-T79), after 160, 810 and 2600 hours of natural ageing respectively, Appendix 4.1.

4.4 Evaluation of the recorded data

In order to obtain a fair comparison between different sets of data due consideration must be given to the displacement of the thermocouples inside the drilled holes, as illustrated in Figure 35. In particular, if the HAZ thermal gradients are steep, such effects may be a source of error, which can lead to a systematic discrepancy between theory and experiments.
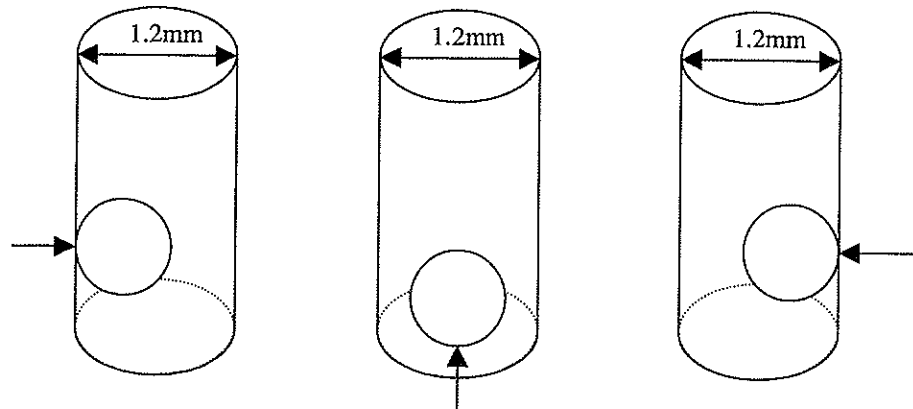
Figure 35 Schematic diagrams illustrating the displacement of the thermocouples inside the drilled holes in different directions.

4.4.1 HAZ thermal programme

In general, the thermal data show that the peak temperature in a given position tend to decrease with increasing welding speed. This is in accordance with heat conduction theory. When the hardness profiles are compared with the thermal measurements, the total HAZ width corresponds approximately to the ~300°C isotherm for the 6082-T6 alloy and the ~250°C isotherm for the 7108-T79 alloy.

4.4.2 Edge effects

By comparing the recorded thermal histories in different positions along the weld, i.e. thermocouples 1, 2, 5 and 8 in Figure 1, it is obvious that the peak temperature in a given position is higher at the edges of the plates compared to the mid regions. This shows that reflection of heat from edges interfer with the thermal programme during FSW of aluminium alloys.

4.4.3 Circumferential variation in heat generation

By comparing the HAZ hardness profiles and thermal measurements from shear and flow side of the weld, they all show symmetry across the weld centre line indicating an axisymmetric heat source. This observation is not surprising, considering the relatively short time required for one tool rotation compared to the total tool/base plate interaction time. This implies that conductive heat transfer quickly evenly distributes any circumferential variation in the heat generation[1].

4.4.4 Thermal conditions within the deformed material

The thermal data referring to the positions in Figure 2 show variations in peak temperature from ~350°C to ~500°C for both alloys, indicating steep temperature gradients in the through thickness direction beneath the tool shoulder. The majority of the thermocouples were positioned very close or just inside the deformed material, and all showed peak temperatures close to 450±20°C. This indicates that the extension of the deformed region corresponds approximately to the 450°C isotherm.

---

[1] M.J. Rusell, H.R. Shercliff and P. Threadgill, Cambridge University Engineering Department, Technocal Report CUED/C-MATS/TR242, December 1997.

Appendix 4.1

Weld number:	1997.10.23-1				
Base material ID:	6082-1				
Welding speed (mm/s):	5		Welding force (N):		6000
Rotation speed of tool(RPM):	1500		Hold time before weld travel starts(s):		-
Tool/pin status:		**New pin:**	Yes	**Weld No.:**	
Filename for data logged:	971023-1.DAT				
Execution interval for data logger (s):		0.6			
Status thermocouples before Logging:	**Elements functioning OK:**		**1-8**	**Element no. defect:**	
Time for start of logging:	1054				
Time for stop of logging:	1059				
Comments					
Location of thermocouples: **Figure 1**					

Weld number:	1997.10.23-2				
Base material ID:	6082-2				
Welding speed (mm/s):	8		Welding force (N):		6000
Rotation speed of tool(RPM):	1500		Hold time before weld travel starts(s):		-
Tool/pin status:		**New pin:**		**Weld No.:**	2
Filename for data logged:	971023-2.DAT				
Execution interval for data logger (s):		0.6			
Status thermocouples before Logging:	**Elements functioning OK:**		**1-8**	**Element no. defect:**	
Time for start of logging:	1239				
Time for stop of logging:	1246				
Comments: Results for thermocouple no.7 seems not realistic.					
Location of thermocouples: **Figure 1**					

Weld number:	1997.10.23-3			
Base material ID:	6082-3			

Welding speed (mm/s):	8	Welding force (N):	6000	
Rotation speed of tool(RPM):	1500	Hold time before weld travel starts(s):	-	
Tool/pin status:	New pin:		Weld No.:	3
Filename for data logged:	971023-3.DAT			
Execution interval for data logger (s):	0.6			
Status thermocouples before Logging:	Elements functioning OK:	1-8	Element no. defect:	
Time for start of logging:	1322			
Time for stop of logging:	1327			

Comments:
Location of thermocouples: **Figure 1**

Weld number:	1997.10.23-4			
Base material ID:	6082-4			

Welding speed (mm/s):	12	Welding force (N):	6000	
Rotation speed of tool(RPM):	1500	Hold time before weld travel starts(s):	-	
Tool/pin status:	New pin:		Weld No.:	4
Filename for data logged:	971023-4.DAT			
Execution interval for data logger (s):	0.6			
Status thermocouples before Logging:	Elements functioning OK:	1-8	Element no. defect:	
Time for start of logging:	1322			
Time for stop of logging:	1327			

Comments:
Location of thermocouples: **Figure 1**

Weld number:	1997.10.23-5			
Base material ID:	7108-5			

Welding speed (mm/s):	5		Welding force (N):	6000
Rotation speed of tool(RPM):	1500		Hold time before weld travel starts(s):	-
Tool/pin status:	**New pin:**		**Weld No.:**	5
Filename for data logged:	971023-5.DAT			
Ececution interval for datalogger (s):	0.6			
Status termocouples before Logging:	**Elements functioning OK:**	**1,3,4,5,6,7,8**	**Element no. defect:**	2 slow response
Time for start of logging:	1418			
Time for stop of logging:	1427			
Comments:				
Location of thermocouples: **Figure 1**				

Weld number:	1997.10.23-6			
Base material ID:	7108-6			

Welding speed (mm/s):	8		Welding force (N):	6000
Rotation speed of tool(RPM):	1500		Hold time before weld travel starts(s):	-
Tool/pin status:	**New pin:**		**Weld No.:**	6
Filename for data logged:	971023-6.DAT			
Ececution interval for datalogger (s):	0.6			
Status termocouples before Logging:	**Elements functioning OK:**	**1,2,3,4,5,7,8**	**Element no. defect:**	6 defect
Time for start of logging:	1444			
Time for stop of logging:	1448			
Comments:				
Location of thermocouples: **Figure 1**				

Weld number:	1997.10.23-7				
Base material ID:	7108-7				
Welding speed (mm/s):	8		Welding force (N):	6000	
Rotation speed of tool(RPM):	1500		Hold time before weld travel starts(s):		1.8
Tool/pin status:		New pin:		Weld No.:	7
Filename for data logged:	971023-7.DAT				
Execution interval for data logger (s):		0.6			
Status thermocouples before Logging:	Elements functioning OK:		1,2,3,5,6,7,8	Element no. defect:	4 defect
Time for start of logging:	1732				
Time for stop of logging:	1737				
Comments:					
Location of thermocouples: **Figure 1**					

Weld number:	1997.10.23-8				
Base material ID:	7108-8				
Welding speed (mm/s):	12		Welding force (N):	6000	
Rotation speed of tool(RPM):	1500		Hold time before weld travel starts(s):		1.8
Tool/pin status:		New pin:		Weld No.:	8
Filename for data logged:	971023-8.DAT				
Execution interval for data logger (s):		0.6			
Status thermocouples before Logging:	Elements functioning OK:		1,3,4,5,6,7,8	Element no. defect:	2 defect
Time for start of logging:	1801				
Time for stop of logging:	1808				
Comments:					
Location of thermocouples: **Figure 1**					

Appendix 4.2

Weld number:	1997.10.24-1			
Base material ID:	6082-11			

Welding speed (mm/s):	8		Welding force (N):	6000
Rotation speed of tool(RPM):	1500		Hold time before weld travel starts(s):	1.8
Tool/pin status:	**New pin:**		**Weld No.:**	9
Filename for data logged:	971024-1.DAT			
Execution interval for data logger (s):	0.1			
Status thermocouples before Logging:	**Elements functioning OK:**	**1-8**	**Element no. defect:**	
Time for start of logging:	1115			
Time for stop of logging:	1117			

Comments: - Position no. 3 mounted on topside of plate (position no. 5), all other elements mounted on rear side. - Element no. 1 defect.
Location of thermocouples: **Figure 2**

Weld number:	1997.10.24-2			
Base material ID:	7108-12			

Welding speed (mm/s):	8		Welding force (N):	6000
Rotation speed of tool(RPM):	1500		Hold time before weld travel starts(s):	1.8
Tool/pin status:	**New pin:**		**Weld No.:**	10
Filename for data logged:	971024-2.DAT			
Execution interval for data logger (s):	0.1			
Status thermocouples before Logging:	**Elements functioning OK:**	**1,2,3,5,6,7,8**	**Element no. defect:**	4
Time for start of logging:	1212			
Time for stop of logging:	1214			

Comments: - Thermocouple 2 and 3 mounted on topside of plate, position 5 and 6 respectively. - Thermocouple no. 4 defect.
Location of thermocouples: **Figure 2**

Weld number:	1997.10.24-3			
Base material ID:	6082-9			

Welding speed (mm/s):	8	Welding force (N):	6000	
Rotation speed of tool(RPM):	1500	Hold time before weld travel starts(s):	1.8	
Tool/pin status:	New pin:		Weld No.:	11
Filename for data logged:	971024-3.DAT			
Execution interval for data logger (s):	0.1			
Status thermocouples before Logging:	Elements functioning OK:	2,4,5,6,7,8	Element no. defect:	1 and 3 not active.
Time for start of logging:	1254			
Time for stop of logging:	1256			

Comments: - Position no. 1 and 3 not active because of lack of thermocouples.
Location of thermocouples: **Figure 2**

Weld number:	1997.10.24-4			
Base material ID:	7108-10			

Welding speed (mm/s):	8	Welding force (N):	6000	
Rotation speed of tool(RPM):	1500	Hold time before weld travel starts(s):	1.8	
Tool/pin status:	New pin:		Weld No.:	12
Filename for data logged:	971024-4.DAT			
Execution interval for data logger (s):				
Status thermocouples before Logging:	Elements functioning OK:	1,2,4,5,6,7	Element no. defect:	3 and 8 not active
Time for start of logging:	1327			
Time for stop of logging:	1328			

Comments: - Element no. 3 and 8 not active because of lack of thermocouples.
Location of thermocouples: **Figure 2**

Part V: Characterisation of the subgrain structure within the plastically deformed region of friction stir welds

5.1 Introduction

During FSW the material is exposed to deformation at elevated temperatures, leading to a very fine grain structure within the plastically deformed region. In the literature both dynamic recovery and dynamic recrystallization have been proposed as mechanisms for the microstructure evolution in this region during FSW of aluminium alloys /1,2,3/. In the present study post weld annealing of friction stir welded AA6082-T6 and 7108.50-T79 alloys is used to evaluate whether the reported difference in the static recrystallization behaviour of the plastically deformed region /3/ can be attributed to spatial variations in the subgrain structure in the as-welded condition. This will be done by means of the electron backscatter diffraction (EBSD) technique in combination with scanning electron microscopy (SEM), which is a widely accepted method for characterisation of microstructures and measurements of grain orientations in metals and alloys /4/.

The symbols and units used throughout the chapter are defined in Appendix 5.1.

5.2 Dynamic recovery vs. recrystallization

Based on the literature revived, it is generally accepted that aluminium and its generic alloys will dynamically recover during deformation. This is due to a high stacking fault energy, which means that dislocation climb and cross-slip will occur readily, thus allowing the dislocations to arrange themselves in cell walls that are roughly equispaced to form subgrains /5, 6/. However, some Al-Mg alloys have been reported to dynamically recrystallize due to the high solute content hindering the dislocation motion. Under such conditions nucleation of dynamic recrystallization occurs at dislocation clusters /7, 8/, but this is just in rare cases.

Based on the above findings, it is reasonable to assume that dynamic recovery is the dominating softening process for the alloys of interest here, i.e. AA6082-T6 and 7108-T79 during deformation at elevated temperatures. The stress-strain curve is then typically characterised by a rise to a plateau followed by a constant or steady state flow stress, as shown in Figure 1. During the initial stages of deformation there will be an increase in the flow stress as dislocations

interact and multiply. However, as the dislocation density rises, which means that the driving force and hence the rate of recovery increases, a microstructure of low angle boundaries and subgrains develops. At a certain strain, the rate of work hardening and recovery reaches a dynamic equilibrium, in the sense that the dislocation density remains constant and a steady state flow stress is obtained. This is shown by the plateaus in Figure 1.
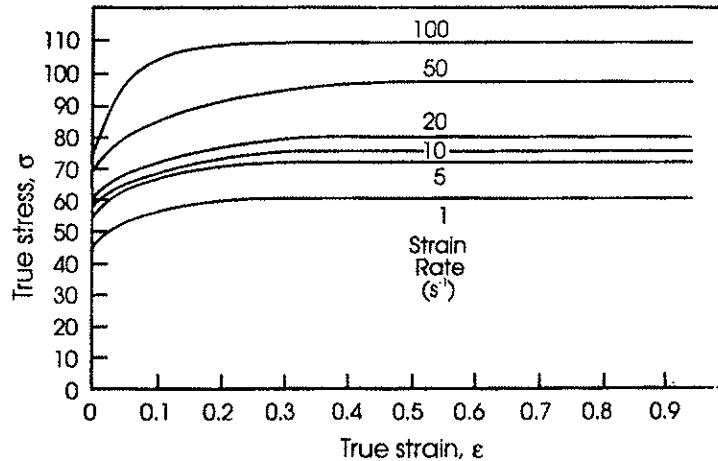

Figure 1 Stress-strain curves for Al-1%Mg at 400°C /9/.

Generally speaking, the factors which tend to promote the formation of a subgrain structure during deformation are high stacking fault energy, low solute content, large strains and high temperature of deformation /5/. Consequently, the conditions existing in FSW would be expected to promote the formation of a well-developed subgrain structure after the deformation and the cooling of the weld.

5.2.1 Constitutive relationships for dynamic recovery

When dynamic recovery takes place, the grains become elongated in the direction of the material flow and the material undergoes repoligonization, which keeps the grains dimensionally stable and equiaxed /10/. In general, an increase in temperature or decrease in strain rate will result in the formation of larger, more perfect, subgrains during the recovery process /11/. In contrast, at lower temperatures and higher strain rates the strain for nucleation of new subgrains increases, which gives rise to a finer subgrain structure in the deformed material.

The subgrain size that develops in the material under hot working conditions is inversely related to the steady state stress. When the steady state condition is reached, the dislocation generation rate will balance the dislocation annihilation rate, which means that aluminium alloys can be deformed to large strains without undergoing any significant change in the flow stress or the subgrain size. The control variables are temperature and strain rate ($\dot{\varepsilon}$), and together they define the amount of recovery per unit strain and hence, the accumulated dislocation density as well as the subgrain diameter (d). Mathematically, this relationship can be expressed as /12,13/:

$$d^{-m} = a + b \log Z_h \qquad (1)$$

where a and b are experimental constants, m is an exponent between 0.5 and 1 /14/, and Z_h is the Zener-Hollomon parameter defined by:

$$Z_h = \dot{\varepsilon} \exp\left[\frac{Q}{RT}\right] \qquad (2)$$

Equation (2) is generally valid for most aluminium alloys, irrespective of the mode of deformation /15/. Since the equations relating stress to temperature and strain rate are the same as for creep, it has been possible to show that the activation energy Q for deformation of aluminium alloys remains essentially unchanged over a strain rate range of eight orders of magnitude /12, 13/. Figure 2 shows the relationship between substructural characteristics and deformation parameters for hot worked aluminium alloys for different values of the Zener-Hollomon parameter.
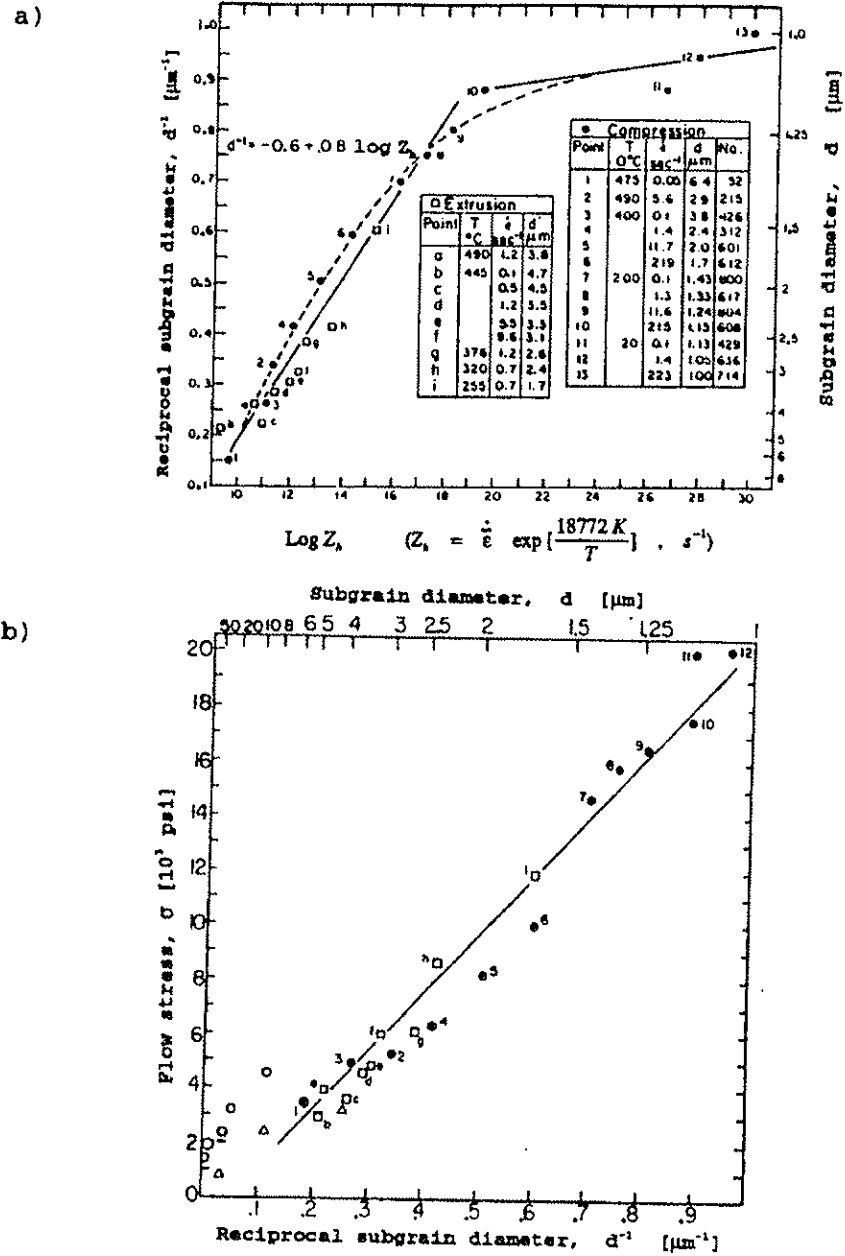
Figure 2 Relationship between substructural characteristics and deformation parameters for hot worked aluminium. a) Dependence of subgrain diameter on temperature T and strain rate $\dot\varepsilon$, b) Dependence on high temperature flow stress σ on subgrain diameter d /16/.

5.3 General background for the EBSD technique

Since the discovery of the EBSD technique by Venables and Harald in 1973 /17/ the technique has emerged to become an important tool in a multitude of different fields. The principle of the EBSD technique is that the packscattered Bragg diffracted electrons, which form when a stationary electron beam is focused on a steeply tilted sample in a SEM, are collected by a phosphor screen. The packscattered electrons form a pattern, so called EBSP, constituted of Kikuchi lines that can be viewed on a TV screen, as shown for the experimental set-up illustrated in Figure 3. By using dedicated software, the pattern is indexed by a PC giving a unique description of the crystal orientation at the primary beam position. Furthermore, it is possible to map complete surface areas by moving the primary electron beam pixel by pixel, storing the crystallographic orientation in each pixel, giving a complete picture of the relative orientation of the grains and detecting all grain boundaries. By applying a colour for each set of Euler angles, it is possible to obtain a picture of the grain structure based on the individual grain orientation.
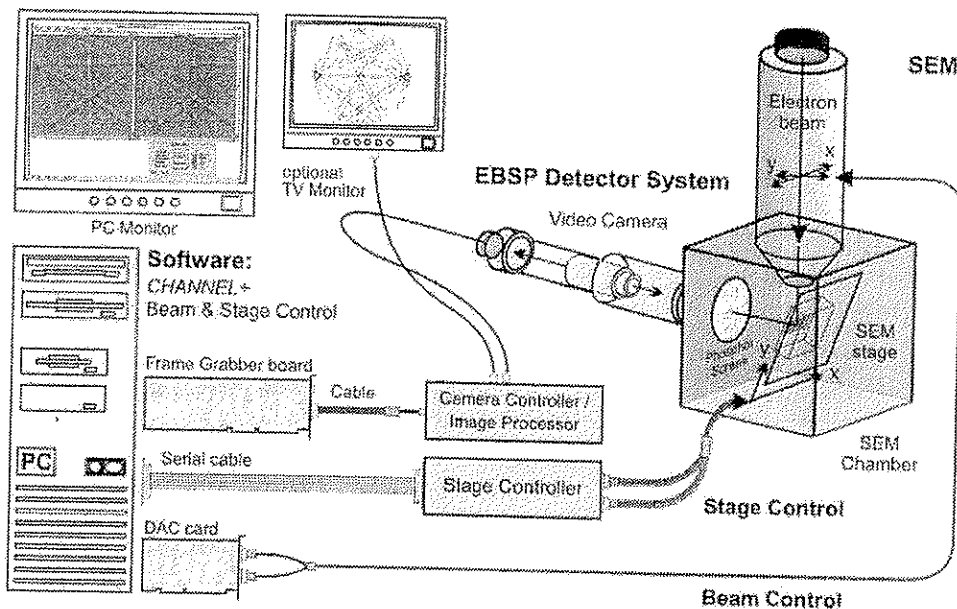
Figure 3 Sketch of EBSD experimental set-up /18/.

5.4 Experimental programme

The panels selected for this investigation were friction stir welded, using the operating parameters corresponding to Series No. 3 and 8 in Table 1 (see Part IV of the thesis). These series refer to the aluminium alloy 6082-T6 and 7108.50-T79, respectively.

5.4.1 Base materials

The microstructure of the two base materials is shown in Figure 4 and 5.

Figure 4 Microstructure of base material, extruded AA6082-T6 panel (20X).

Figure 5 Microstructure of base material, extruded 7108-T79 panel (40X).

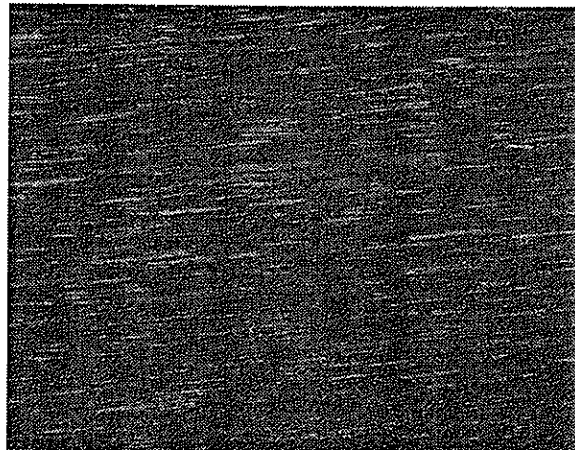As expected, both alloys exhibit deformed grains that are strongly elongated in the extrusion direction. This type of microstructure is typical of aluminium alloys containing dispersoids for inhibition of recrystallization and grain growth /5/.

5.4.2 Post weld annealing

In order to investigate the thermal stability of the microstructure within the plastically deformed region of the welds, small samples of the AA6082-T6 and 7108.50-T79 materials were immersed into a salt bath at varying temperatures and holding times. The heat treatment procedure employed is summarised in Table 1. Both the as-welded and the annealed specimens were first ground, and then polished down to a 1μm surface finish before anodising, using a reagent consisting of 760ml. of H_2O and 40ml. of HBF_4. The subsequent visual inspection of the reheated specimens was carried out in a light microscope under polarized light.

Table 1 Heat treatment procedure used for post weld annealing.

Alloy	Temperature (°C)	Annealing time (min)
6082-T6	510	1
	510	15
7108.50-T79	475	15
	475	30

5.4.3 EBSD analyses

Cross-sections of the as-welded materials were first ground, and then polished down to a 1μm surface finish before electropolishing, using a reagent consisting of 78ml. of perchloric acid, 120ml. of H_2O, 700ml. of ethanol and 100ml. of ethylenglycolmonobutylether ($C_6H_{14}O_2$), to remove any previous mechanical deformation from the surface. The EBSD analysis was designated to obtain a complete mapping of the microstructure at specific positions in the through thickness direction of the weld, as described previously in Section 5.2. The examination was done using a JEOL 840 SEM equipped with a NORDIF

EBSP hardware and CHANNEL + EBSP software for fully automated pattern indexing. The beam was set to scan an area of 75x100 μm^2, with a constant step size of 1 μm. A description of this system and the applied experimental set-up has been reported elsewhere /4/.

5.4.4 Hardness measurements

In order to detect possible hardness variations within the plastically deformed region due to spatial variations in the subgrain structure, a series of Vickers hardness measurements were performed in the through thickness direction of the welds close to the centre line. These measurements were done using a Matsuzawa DVK-1S hardness testing device at a constant load of 0.5 kg for the 6082-T6 alloy and 1 kg for the 7108-T79 alloy.

5.5 Results

5.5.1 Heat treatment experiments

The results from the FSW and the post weld annealing experiments are shown in Figure 6 through 11. When comparing the microstructures in the as-welded condition (Figures 6 and 9) with the microstructures obtained after post weld annealing (Figures 7-8 and 10-11, respectively) it is evident that some regions of the weld have recrystallized whereas other regions seem unaffected. At the same time the micrographs show that an increase in the annealing time does not significantly affect the grain size after the onset of recrystallization. This means that grain growth is effectively impeded by the presence of a fine distribution of stable dispersoids.

Figure 6 Microstructure of as-welded AA6082-T6 friction stir welded plate.

Figure 7 Microstructure of post weld annealed AA6082-T6, 1 min at 510°C.

Figure 8 Microstructure of post weld annealed AA6082-T6, 15 min at 510°C.
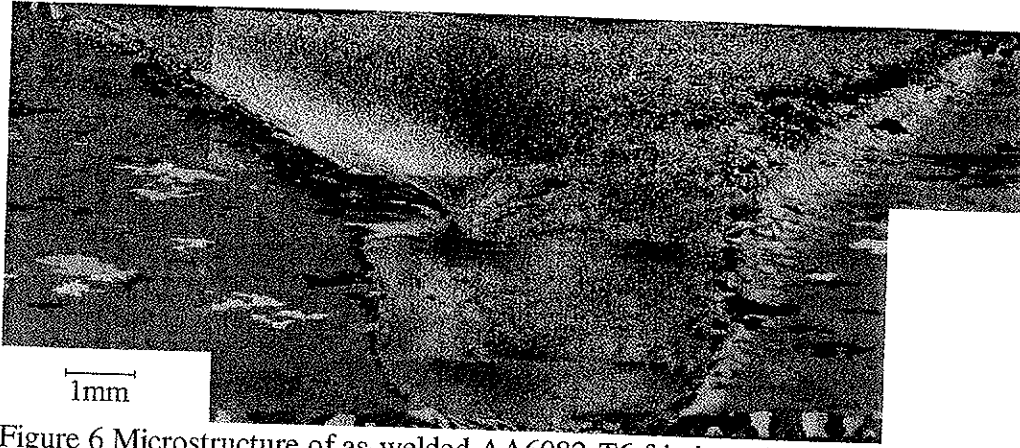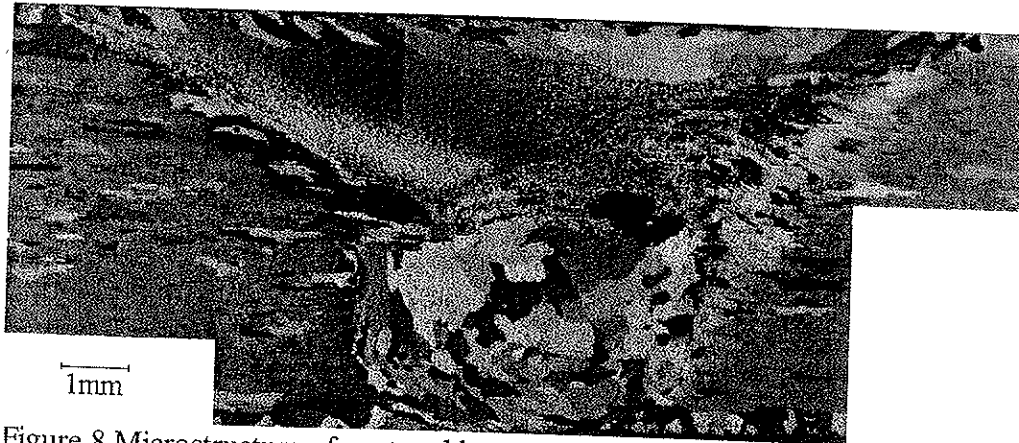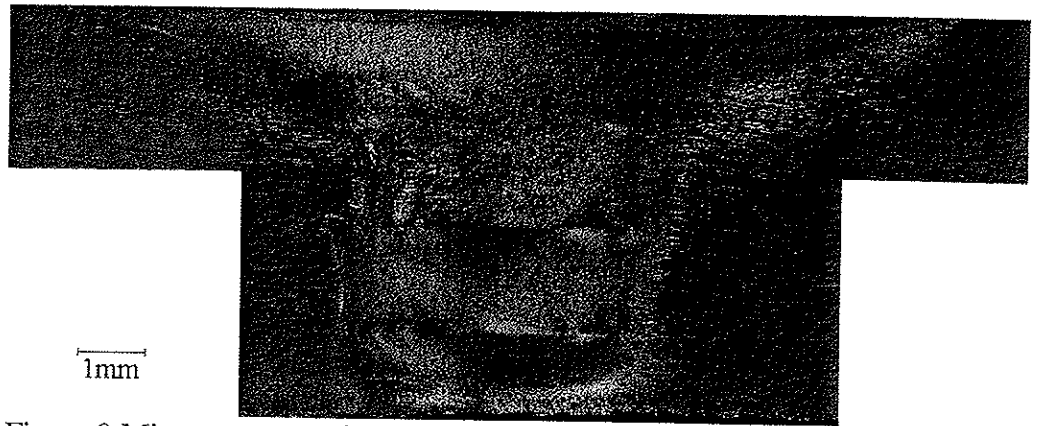
Figure 9 Microstructure of as-welded AA7108.50-T79 friction stir welded plate.
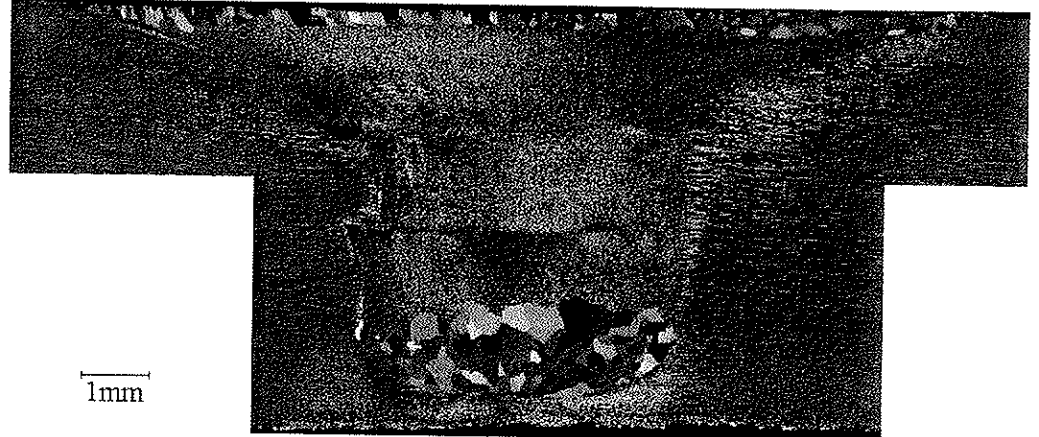

Figure 10 Microstructure of post weld annealed AA7108.50-T79, 15 min at 475°C.

Figure 11 Microstructure of post weld annealed AA7108.50-T79, 30 min at 475°C.

5.5.2 EBSD orientation maps

Based on the results obtained from the post weld annealing experiments it is possible to divide the plastically deformed part of the weld into two distinct regions, i.e. recrystallized and non-recrystallized. In order to reveal possible differences in the subgrain structure between these two regions, detailed EBSD mapping of the as-welded specimens was performed. This was done at the locations indicated in Figure 12.

A: Recrystallized region
B: Non-recrystallized region
C: Location of the EBSD measurements
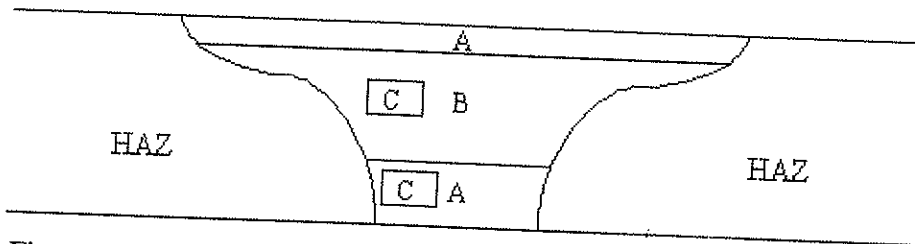
Figure 12 Schematic diagram showing the recrystallized and non-recrystallized regions within the plastically deformed material after post weld annealing. The corresponding locations of the EBSD measurements are also indicated.

Figures 13 and 14 show representative EBSD orientation maps for the AA6082-T6 and AA7108-T79 weldment, respectively. Figures 13a and 14a show the areas that did not recrystallize after post weld annealing, while Figure 13b and 14b show the microstructure within the recrystallized regions. Superimposed on these maps is also the spatial misorientation between the individual grains. Here, low angle grain boundaries are characterised by misorientations between 1.5 to 15°, and are indicated by the thin lines in the maps. Conversely, high angle grain boundaries are defined by misorientations greater than 15°, and are marked as thick solid lines.

(a)

75μm

100μm

(b)

75μm

100μm

Figure 13 EBSD orientation maps for AA6082-T6 in the as-welded condition; (a) area unaffected by post weld annealing, (b) area recrystallized after post weld annealing.

(a)

75μm

100μm

(b)

75μm

100μm

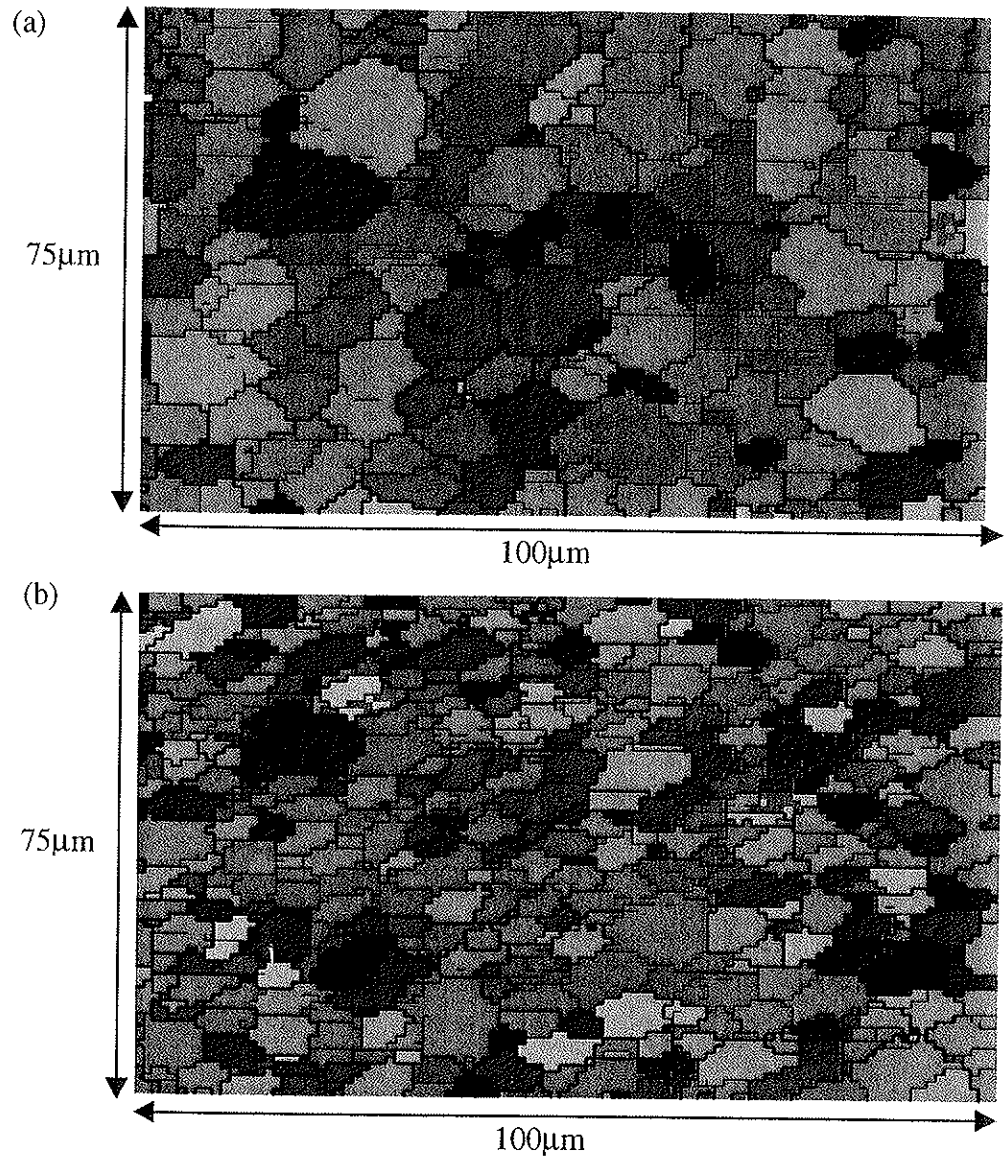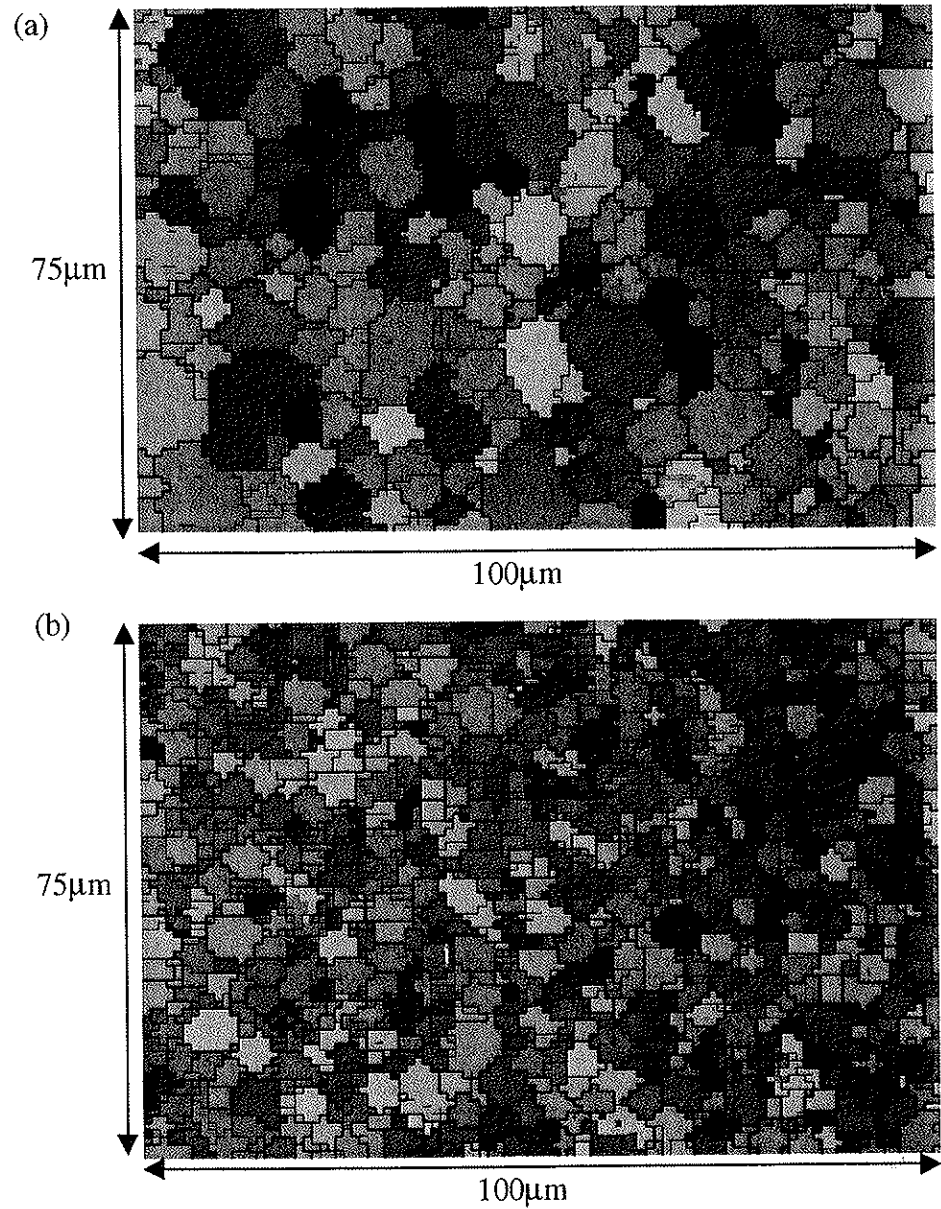Figure 14 EBSD orientation maps for AA7108-T79 in the as-welded condition; (a) area unaffected by post weld annealing, (b) area recrystallized after post weld annealing.

It is evident from these orientation maps that the microstructure within the plastically deformed region of both welds consists of a mixture of low and high angle grain boundaries, as frequently observed after dynamic recovery /5/. Moreover, there is a clear difference in the subgrain structure between the two regions examined, i.e. the finest subgrain size is observed within the area that did not recrystallize after post weld annealing. This difference is quantified in Table 2, which contains average numbers for the subgrain size in the two regions, as determined by means of the mean linear intercept technique.

Table 2 Average sub-grain size for the two weldments.

Weldment	Sub-grain size (μm)	
	Region A*	Region B**
AA6082-T6	3.5	4.8
7108-T79	2.5	3.8

* Refers to Figures 14b and 15b.
** Refers to Figures 14a and 15a.

5.5.3 Hardness measurements

The results from the Vickers hardness measurements are shown in Figure 15. These measurements were taken in the through-thickness direction of the welds close to the centre line.
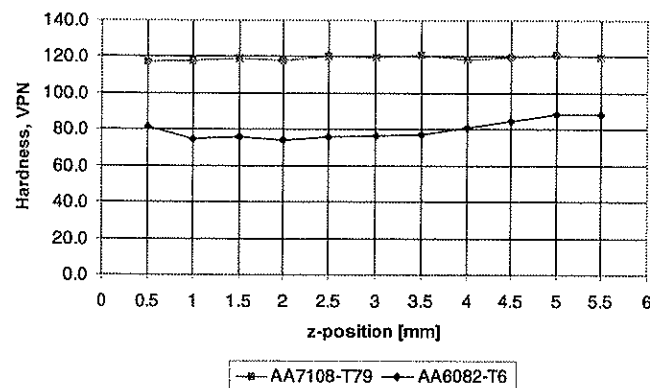

Figure 15 Hardness profiles in the through-thickness (z) direction of the welds close to the centre line. The testing is done in the as-welded condition after 12 months of natural ageing.

It is evident from Figure 15 that the local hardness within the plastically deformed region of the welds is not significantly affected by the observed variation in the subgrain size in the through-thickness direction. This means that precipitation strengthening due to natural ageing will completely override the contribution from work hardening when the subgrain size is, say, 2.5 μm or larger. Both alloys show the same behaviour, but the strength recovery following natural ageing is most significant in the 7108-T79 weldment.

5.6 Discussion

From the EBSD orientation maps presented in Figures 13 and 14 it is obvious that dynamic recovery is the most likely softening process during FSW of the 6082-T6 and the 7108-T79 alloys. This observation is not surprising, considering the fact that dislocation climb and cross-slip occur readily in Al at elevated temperatures because of the high stacking fault energy /5, 6/.

5.6.1 Estimation of local strain rates during FSW

In general, the Zener-Holloman (Z_h) parameter provides a basis for evaluating the evolution of the subgrain structure during hot deformation, as discussed previously in Section 5.2.1. As shown by McQueen and Jonas /16/, the following relationship exists between the subgrain diameter d and the Z_h- parameter in aluminium alloys:

$$d = \left[-0.60 + 0.08 \log Z_h \right]^{-1} \tag{3}$$

where

$$Z_h = \overset{\bullet}{\varepsilon} \exp\left[\frac{18772}{T_p}\right] \tag{4}$$

and T_p is the peak temperature of the thermal cycle in a given position (in K).

By inserting the measured values for the subgrain size from Table 2 and using the 3-D heat flow model presented in Part III of the thesis to calculate the peak temperature distribution during FSW, it is possible to estimate the local strain rate within the plastically deformed region, as shown in Table 3. Notice that the

reported differences in T_p between the two weldments are due to the different welding speeds used in the experiments, i.e. 8mm/s for the AA6082-T6 alloy and 12mm/s for the AA7108-T79 alloy.

Table 3 Estimated strain rates within the plastically deformed region of the experimental friction stir welds.

Alloy	position *	T_p (°C)	d (μm)	Z_h	$\dot{\varepsilon}$ (s^{-1})
6082-T6	B	550	4.8	1.28E+10	1.6
	A	540	3.5	1.10E+11	10.3
7108-T79	B	500	3.8	5.82E+10	1.7
	A	450	2.5	3.26E+12	17.3

* Defined in Figure 12.

It is important to realise that the estimated values in Table 3 are conservative in that they represent upper limits for the local strain rates. This is because the peak temperature of the thermal cycle in each position is used as input to the Zener-Holloman equation. In practice, the final subgrain structure is the result of a series of events that occur during heating and cooling. Hence, both the effective temperatures and the real strain rates may be significantly lower than the values indicated in Table 3.

5.6.2 Deformation pattern within the plastically deformed region

As shown in Table 3, the estimated strain rates within the plastically deformed region of the friction stir welds are quite low compared with the rotational speed of the tool, which, at least, is one order of magnitude higher. This means that the condition for sticky friction at the matrix/tool interface is not met under the prevailing circumstances, probably because of asperity (or local) melting. The phenomenon of local melting is commonly observed in such aluminium alloys during rapid heating. A requirement is that the material is heated above the eutectic temperature at a rate which does not allow the eutectic phase to fully dissolve into the matrix /19/. If the conditions for local melting are met, the presence of a liquid film at the matrix/tool interface will lubricate both the shoulder and the pin, thus resulting in lack of friction. Consequently, local melting may have an indirect effect on the observed deformation pattern during FSW by reducing the effective strain rate in the vicinity of the rotating tool.

5.7 Conclusions

The following conclusions can be drawn from the present investigation:

- The SEM-EBSD technique has proved to be a useful method for characterisation of the microstructure within the plastically deformed region of friction stir welds.
- Based on such examinations, it is concluded that both the 6082-T6 and the 7108-T79 alloys exhibit a microstructure consisting of a mixture of low and high angle grain boundaries in the as-welded condition. The subgrain size within the plastically deformed region is typically between 2.5-5 μm. These results show that dynamic recovery is the most likely softening process during FSW of aluminium alloys, since it allows the material to accommodate the plastic deformation imposed by the rotating pin at elevated temperatures through dislocation climb and cross-slip.
- Calculations based on the Zener-Holloman equation suggest that the local strain rate within the plastically deformed region of the friction stir welds varies from about 1 to 20 s^{-1}. These values are quite low compared with the rotational speed of the tool, which, at least, is one order of magnitude higher.
- The indications are that local melting is the main cause for the reduced effective strain rate in the vicinity of the rotating tool by contributing to the formation of a liquid film at the tool/matrix interface.

5.8 References

1 O.V. Flores, C. Kennedy, L.E. Murr, et.al., Microstructural Issues in a Friction-Stir Welded Aluminium Alloy, Scripta Materialia, Vol. 38, No. 5 pp.703-708, 1998.

2 C.J. Dawes and W.M. Thomas, welding Journal, March 1996, pp. 41-45.

3 H.S. Yang, Microstrucural Developent in Friction Stir Welding of Aluminium Alloys, Proceedings of The 6th International Conference on Aluminium Alloys, ICAA-6, Toyohashi, Japan, July 5-10 1998, Vol.3, pp. 1483-1488.

4 J. Hjelen, Proc. 3rd Int. Confr. on Aluminium Alloys-Their Physical and Mecahnical Properties, Trondhiem, Norway, June 1992, Vol.II, pp.408-413, Publ. The University of Trondheim, The Norwegian Institute of Technology.

5 F.J. Humphereys and M. Hatherly, Recrystallization and related annealing phenomena, Pergamon, Elsevier Science Ltd., Oxford, U.K (1996).

6 T. Sheppard, Temperature and Speed Effects in hot extrusion of aluminium alloys, Metals technology, April, 1981, pp. 130-141.

7 T. Sheppard, N.C. Parson and M.A. Zaidi, Dynamic recrystallization in Al-7Mg alloy, Metal Science, Vil. 17, October 1983, pp. 481-490.

8 H.J. McQueen, E. Evangelista, J. Bowles and G. Crawford, Hot Deformation and Dynamic Recrystallization of Al-5Mg-0.8Mn Alloy, Metal Science, Vol 18, August 1984, pp. 395-402.

9 Puchi E.S., Beynon J.H., and Sellars C.M. (1988), in Int. Conf. on Thermomechanical Processing of Steels, Thermec-88. Tokyo, ISI Japan. 2, 572.

10 McQueen H.J. Wong W.A. and Jonas J.J., Can. J. Phys., vol. 45, 1967, pp. 1225-1235.

11 Bird J.E., Mukherjee A.K. and Dorn J.E., In "Quantitative Relation between Properties and Microstructure", Eds. Brandon D.G and Rosen A., Isr. Program Sci. Transl., 1969, pp. 255-342.

12 Sellars C.M. and McG. Tegart W.J., Int. Met. Rev., 1972, vol. 17, pp. 1-24.

13 Jonas J.J., Sellars C.M. and McG. Tegart W.J., Int. Met Rev., 1969, Vol. 14, pp. 1-24.

14 Zaidi M.A. and Sheppard T., Metal Sci., 1982, vol. 16, pp.229.

15 Zaidi M.A. and Wert J.A., "Thermomechanical Processing of Aluminium Alloys", In Aluminium alloys – Contemporary Research and Applications, Treatise on Material Science Technology, Eds. Vasudevan A.K. and Doherty R.D., 1989, vol.31, pp. 137-167.

16 McQeen H.J. and Jonas J.J., Treatise on Materials Science Technology, "Plastic Deformation of Materials", Academic Press, New York, N.Y., 1975, Vol. 6, pp 393-493.

17 J.A. Venables and C.J. Harland, Phil. Mag., 27 (1973) 1193.

18 brochure: HKL Software, Hobro, Denmark.

19. Ø. Grong: Metallurgical Modelling of Welding, 2. edition, The Institute of Materials, London, 1997, pp. 46.

Appendix 5.1 – Nomenclature

a, b	Experimental constants in grain size equation (μm)
d	Subgrain diameter (μm)
m	Exponent in grain size equation.
Q	Activation energy for deformation (J/mol)
R	Universal gas constant (8.314 J/molK)
T	Temperature (°C)
T_p	Peak temperature (°C)
Z_h	Zener-Holloman parameter (s^{-1})
$\dot{\varepsilon}$	Strain rate (s^{-1})

Part VI: Experimental validation of the FSW-process model

6.1 Introduction

In order to check the validity of the 3-D thermal model developed in Part III of the thesis, the thermal histories reported in Part IV are compared with the computed ones. Furthermore, the thermal model is coupled with dedicated microstructure models to predict the resulting hardness distribution across the weld zone. The measured hardness profiles reported in Part IV of the thesis are then used as a basis for comparison between theory and experiments.

The symbols and units used throughout the chapter are defined in Appendix 6.1.

6.2 Calibration of model

In the following, the input parameters in the thermal model are briefly summarised.

6.2.1 Thermal properties

The thermal properties of the base materials are listed in Table 1.

Table 1 Summary of thermal properties and input data used in heat flow model.

Parameter	ρc (J/m^3°C)	a (mm^2/s)	μ	T_{max} (°C)
Value	$2.4\ 10^6$	58	0.4	555

Note that uniform thermal properties have been assumed for both alloys i.e. 6082-T6 and 7108-T79 to simplify the calculation procedure.

6.2.2 Operating parameters

The operating parameters used in the simulations are the same as those applied in the welding trials reported in Part IV of the thesis (Table 1). It follows that the only variable here is the travel speed, which has the target values of 5, 8 and 12 mm/s, respectively.

6.2.3 Maximum temperature beneath the tool shoulder

In thermal processing of aluminium alloys it is generally accepted that local melting will occur if the material is heated above the eutectic temperature at a rate which does not allow the eutectic phase to fully dissolve into the matrix. In FSW the presence of a liquid film would be expected to lubricate the tool shoulder, leading to a drop in the heat input as the coefficient of friction, μ, decreases from about unity to zero.

During high-speed extrusion of AlMgSi-alloys, asperity melting has been reported to occur already at the eutectic temperature of about 555°C /1/, i.e. far below the solidus temperature of the alloy. In the case of the AlMgZn alloys the eutectic temperature is about 475°C. This means that local melting may occur in the range from 475 to 606°C, where 606°C corresponds to the solidus temperature of the alloy /2/.

As shown in Part IV of the thesis the measured thermal cycles are similar at equal positions in the two base plates. This means that the total heat generation is essentially the same, both in 6082-T6 and 7108.50 T79. Hence, it is reasonable to assume that the maximum temperature T_{max} beneath the tool shoulder is also constant in the two cases.

In order to define a reasonable average value for the maximum temperature, computed thermal cycles with different input values for T_{max} have been compared with those recorded for the high peak temperature region adjacent to the deformed material. The comparison shows that a maximum temperature of 555°C is a reasonable compromise under the prevailing circumstances, as indicated in Figure 1.
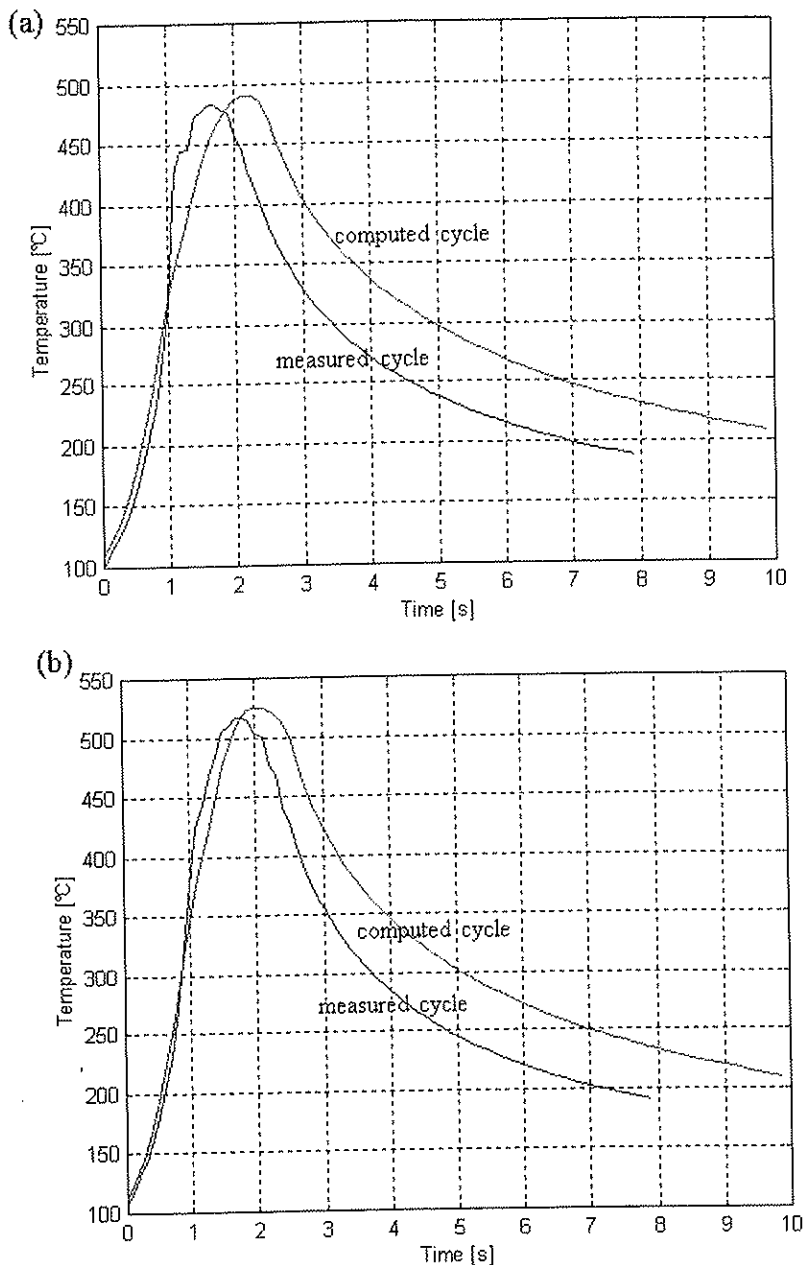
(a)

(b)

Figure 1 Comparison between measured and computed thermal histories for thermocouples located adjacent to plastically deformed region beneath the tool shoulder for a constant input value of T_{max} of 555°C, (a) AA6082-T6 (#6 plate 9), (b) 7108.50-T79 (#6 plate12). Experimental conditions as in Appendix 4.2 (Part IV).

6.2.4 Friction coefficient

Although the coefficient of friction is changing continuously during the welding cycle (i.e. from unity at the dry sliding start towards zero when the temperature for local melting is reached at the tool/base-material interface), it is convenient to keep the coefficient constant in the simulations.

In previous work done on modelling of continuos drive friction welding, the frictional coefficient is assumed to be constant and equal to 0.5. This is close to the conditions reported for sticky friction /3/. Moreover, results obtained from dry sliding tests at ambient temperatures yield a coefficient of about 0.25 for steel sliding on aluminium /4/. Based on these findings, a frictional coefficient of μ=0.4 seems reasonable for both alloys. This means that the frictional conditions during FSW fall between those reported for sticky friction and dry sliding.

6.3 Comparison between measured and computed thermal cycles

In the following, the experimental HAZ thermal cycles reported in Section 4.3 (Part IV) are compared with the computed ones, using the 3-D thermal model and the input parameters summarised in Table 1. Because the thermal diffusivity and all input parameters are assumed to be constant and independent of alloy composition, the same sets of computed thermal cycles are used as a basis for comparison in both cases (i.e. AA6082-T6 and 7108.50-T79).

All the thermal cycles referring to positions 2 to 7 (see Figure 1 in Part IV) are compared with the computed ones. For the series corresponding to a welding speed of 8 mm/s, two parallel experiments were performed. Here the most representative cycle at each position is used as a basis for comparison. Moreover, in cases where the measured point falls between two grid points, the hot side is used for comparison. The results are presented in Figures 2 through 13.
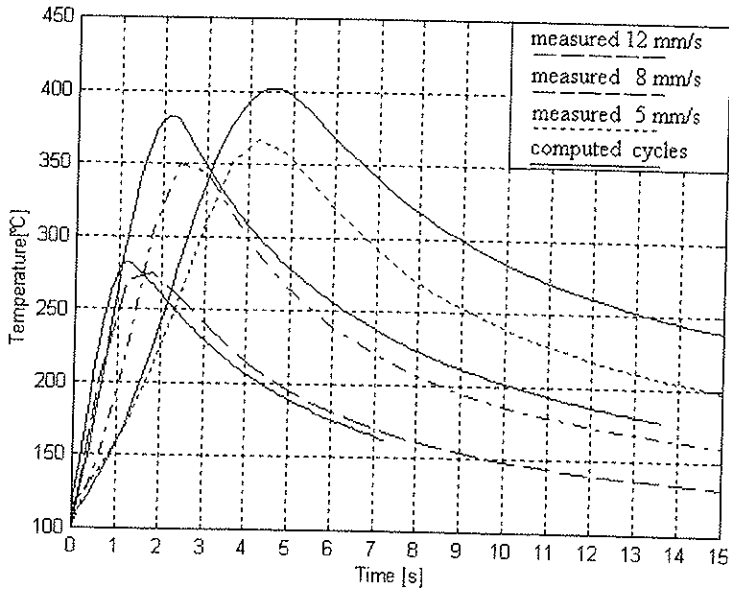
Figure 2 Comparison between measured and computed thermal histories for alloy AA6082-T6. The location of the thermocouples refers to position 2 in plates 1,3 and 4 respectively, as defined in Part IV of the thesis (Appendix 4.1).

Figure 3 Comparison between measured and computed thermal histories for alloy AA6082-T6. The location of the thermocouples refers to position 3 in plates 1,3 and 4 respectively, as defined in Part IV of the thesis (Appendix 4.1).

Figure 4 Comparison between measured and computed thermal histories for alloy AA6082-T6. The location of the thermocouples refers to position 4 in plates 1,3 and 4 respectively, as defined in Part IV of the thesis (Appendix 4.1).
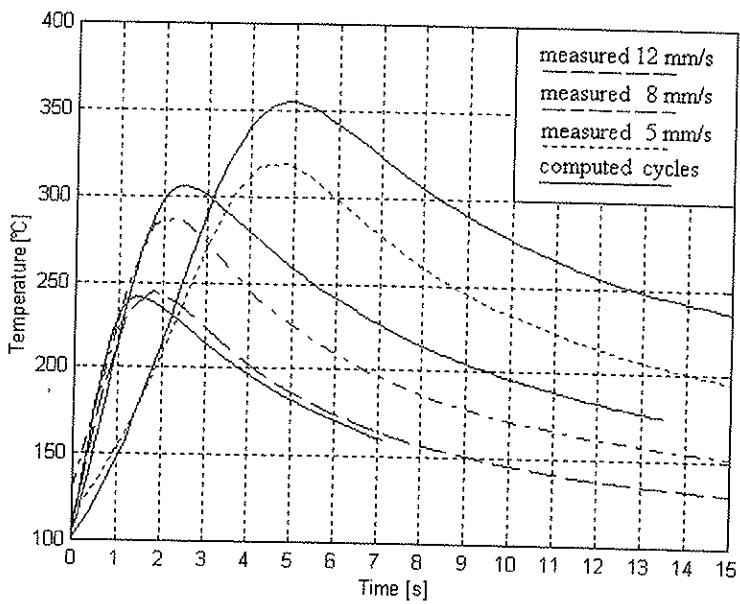

Figure 5 Comparison between measured and computed thermal histories for alloy AA6082-T6. The location of the thermocouples refers to position 5 in plates 1 and 2 respectively, as defined in Part IV of the thesis (Appendix 4.1).

Figure 6 Comparison between measured and computed thermal histories for alloy AA6082-T6. The location of the thermocouples refers to position 6 in plates 1,3 and 4 respectively, as defined in Part IV of the thesis (Appendix 4.1).
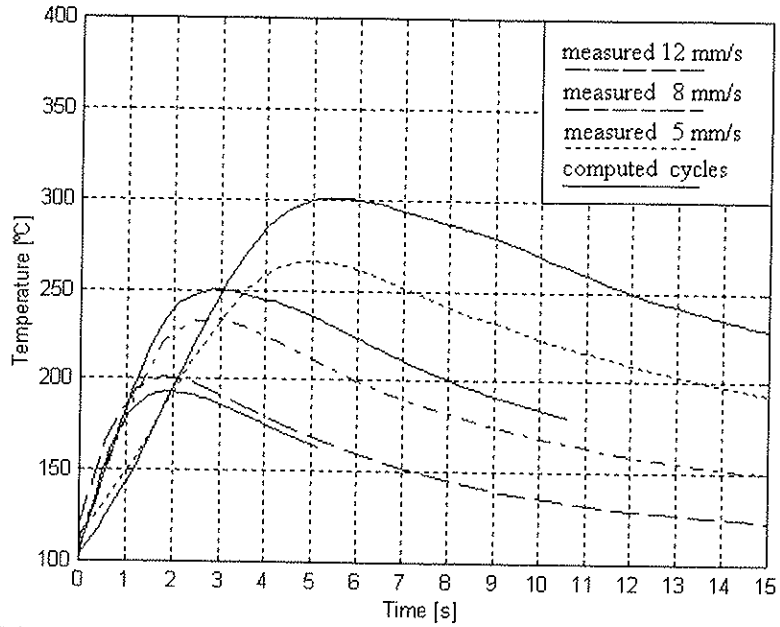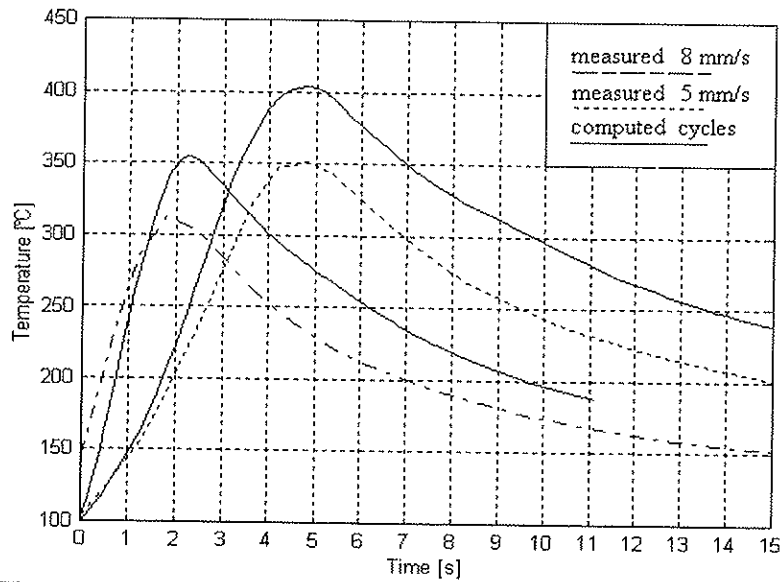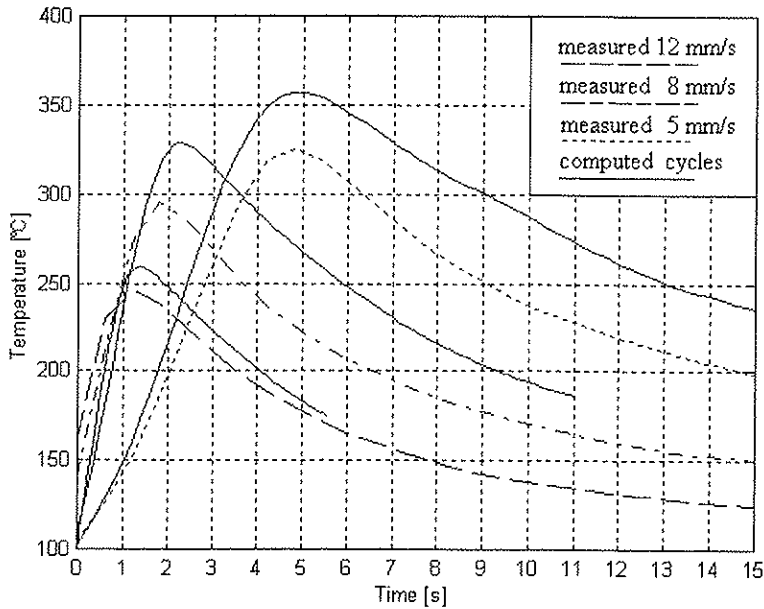

Figure 7 Comparison between measured and computed thermal histories for alloy AA6082-T6. The location of the thermocouples refers to position 7 in plates 1 and 3 respectively, as defined in Part IV of the thesis (Appendix 4.1).

Figure 8 Comparison between measured and computed thermal history for alloy 7108.50-T79. The location of the thermocouple refers to position 2 in plate 6, as defined in Part IV of the thesis (Appendix 4.1).

Figure 9 Comparison between measured and computed thermal histories for alloy 7108.50-T79. The location of the thermocouples refers to position 3 in plates 5,6 and 8 respectively, as defined in Part IV of the thesis (Appendix 4.1).
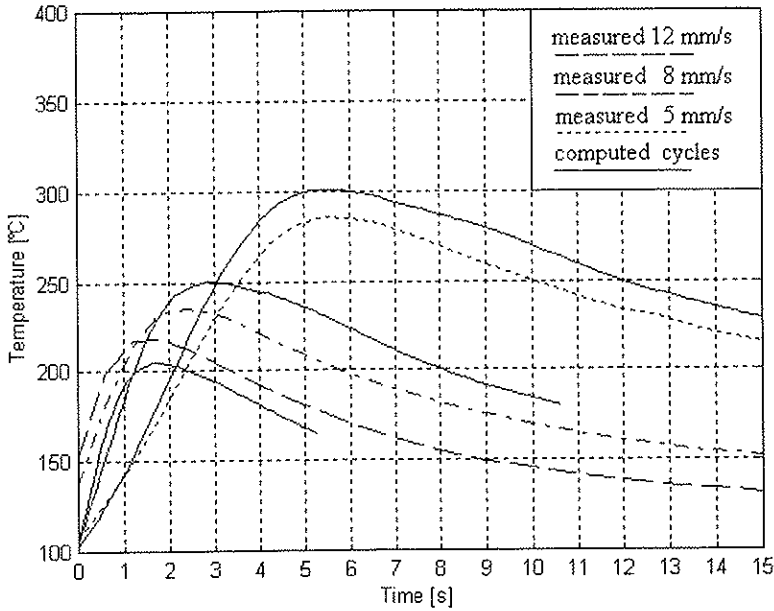
Figure 10 Comparison between measured and computed thermal histories for alloy 7108.50-T79. The location of the thermocouples refers to position 4 in plates 5,6 and 8 respectively, as defined in Part IV of the thesis (Appendix 4.1).
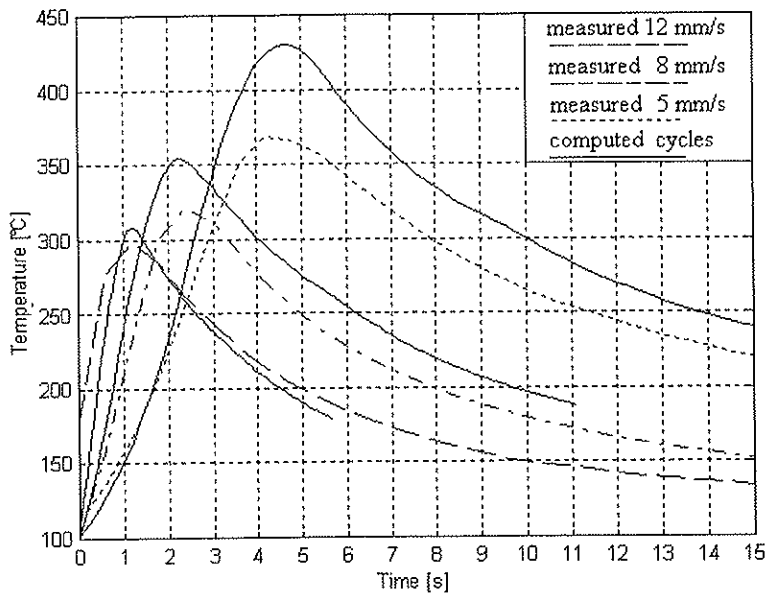
Figure 11 Comparison between measured and computed thermal histories for alloy 7108.50-T79. The location of the thermocouples refers to position 5 in plates 5,7 and 8 respectively, as defined in Part IV of the thesis (Appendix 4.1).
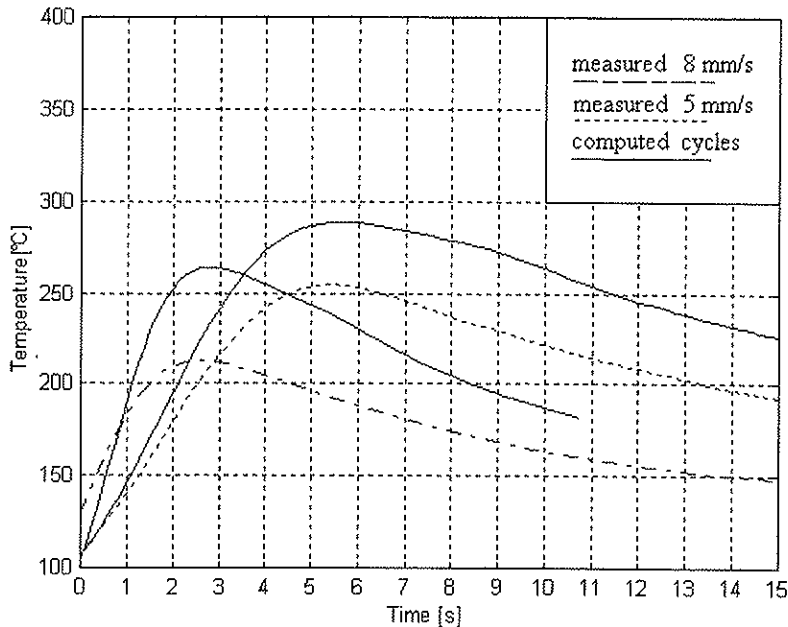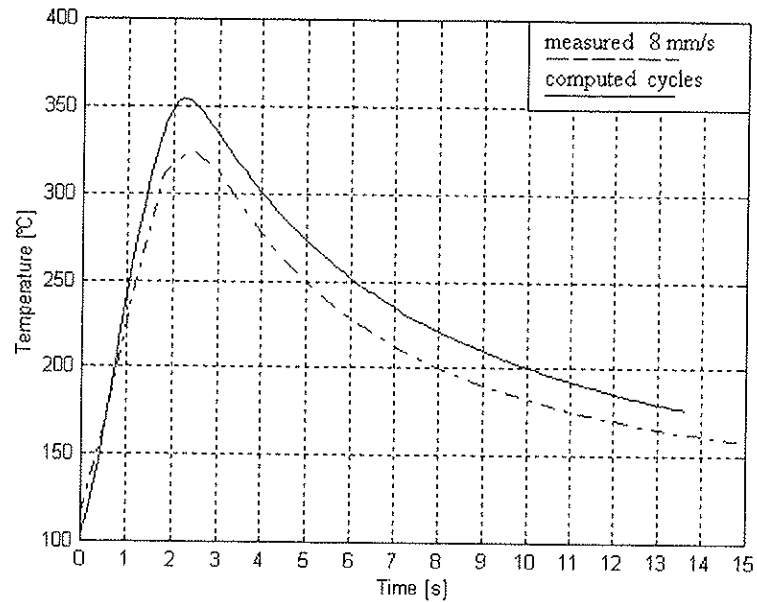
Figure 12 Comparison between measured and computed thermal histories for alloy 7108.50-T79. The location of the thermocouples refers to position 6 in plates 5,7 and 8 respectively, as defined in Part IV of the thesis (Appendix 4.1).
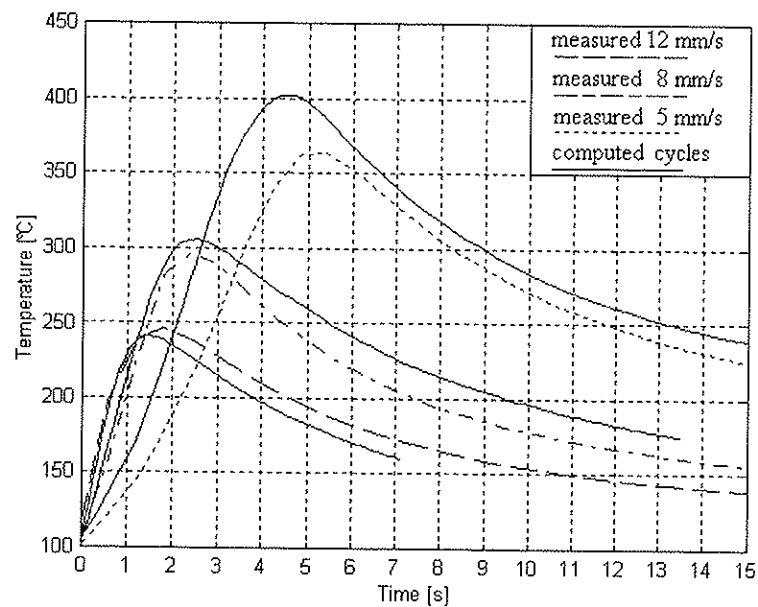

Figure 13 Comparison between measured and computed thermal histories for alloy 7108.50-T79. The location of the thermocouples refers to position 7 in plates 5,6 and 8 respectively, as defined in Part IV of the thesis (Appendix 4.1).
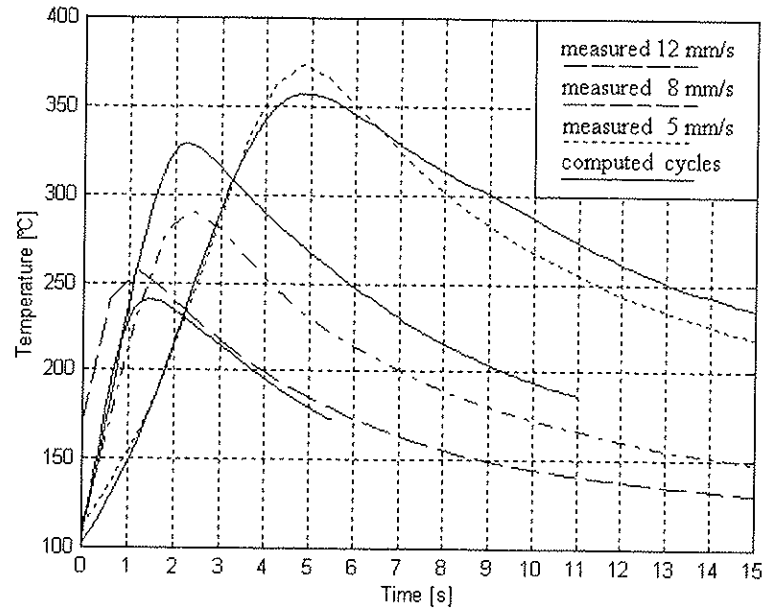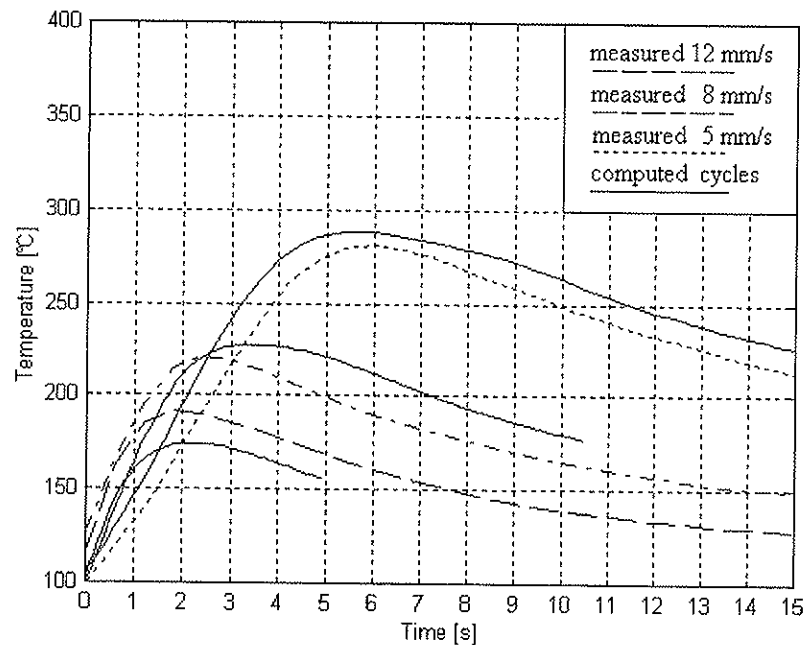
Based on these results, the following main conclusion can be drawn:

6.3.1 Peak temperatures

There appears to be a general trend that the computed peak temperatures are consistently higher than the measured ones. This result is to be expected, as the hot side is used as a basis for comparison when the position of the thermocouple falls between two grid-points.

As shown in Figure 14, the thermal gradient in the transverse (y) direction of the plate is of the order of 15 to 25°C per mm within the high peak temperature region of the weld HAZ. Considering the fact that the diameter of the fused thermocouple head is 1.2 mm (which means that the sampling volume is even larger), it is not surprising to find that the computed peak temperatures, with some exceptions, are consistently 20 to 30°C higher than the measured ones.
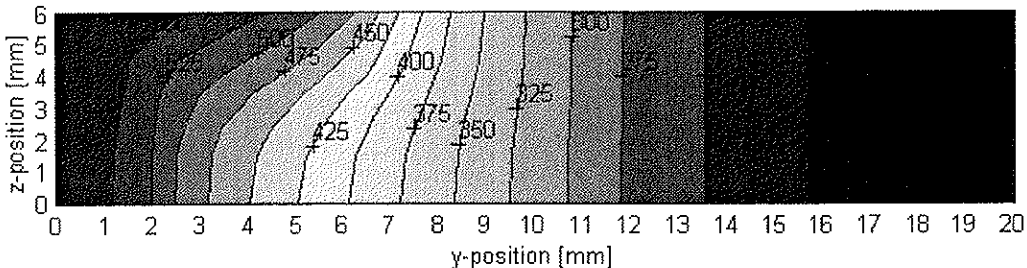
Figure 14 Computed peak temperature contour plot in the transverse (y) direction of the plate for a constant travel speed of 8mm/s. Only half the plate is considered due to symmetry.

6.3.2 Heating and cooling leg of thermal cycles

Besides the observed discrepancy between the predicted and measured peak temperatures, the overall impression is that the thermal model adequately reproduces the heating and cooling conditions within the central part of the HAZ. This is evidenced by the fact that the curves representing the heating and cooling leg of the thermal cycles tend to be parallel and just slightly shifted in time. Consequently, the thermal model seems to be sufficiently comprehensive and relevant to be used as a tool for calculating the temperature distribution

during friction stir welding, in spite of the number of simplifying assumptions involved (e.g. constant values for a, μ and T_{max} and no exchange of heat to the surroundings).

6.4 Coupling of Thermal and Microstructure Models

In the following the thermal model is coupled with the microstructure models described in Part I of the thesis. The MatLab subroutines used to calculate the HAZ hardness distribution are summarised in Appendix 6.2. A brief description of the constitutive equations embedded in the code is given below.

6.4.1 AA6082-T6 weldments

During welding of AA 6082-T6 alloys reversion of β''-precipitates will occur to an increasing extend in the peak temperature range from 250 to 500°C. This is associated with a continuos decrease in the HAZ hardness until the dissolution process is completed. During cooling of the weld, some solute recombines to form coarse, metastable β'(Mg_2Si) precipitates which do not contribute to strengthening. However, in the region beneath the tool shoulder a large fraction of alloying elements will remain in solid solution at the end of the thermal cycle, thereby giving conditions for extensive age-hardening at room temperature over a period of 5-7 days.

6.4.1.1 Reversion model

If the number of particles per unit volume is constant, and the particle volume fraction f and radius r do not vary independently, reversion can be described by a single state variable f. Under such conditions simple diffusion theory shows that the volume fraction falls from its initial value f_0 according to the equation /5, 6/:

$$\frac{f}{f_0} = 1 - \left(\int dt/t_1^* \right)^{n_1} \qquad (1)$$

where n_1 is a time exponent (<0.5), and t_1^* is the time taken for complete particle dissolution at a given temperature defined as /5, 7/:

$$t_1^* = t_{r_1}^* \exp\left[\left(\frac{Q_s'}{n_1 R} + \frac{Q_d}{R}\right)\left(\frac{1}{T} - \frac{1}{T_{r_1}}\right)\right] \qquad (2)$$

Because this equation satisfies the additivity conditions pertaining to an isokinetic reaction it can be integrated numerically over the actual weld thermal cycle in any position within the HAZ.

6.4.1.2 Natural ageing model

By considering the form of the C-curve for precipitation of non-hardening β'(Mg$_2$Si) precipitates at dispersoids, coupled with an analysis of the natural ageing kinetics, Myhr and Grong /5/ arrived at the following expression for the net precipitation increment, referred to the initial content of hardening phases in the peak aged base material:

$$\frac{f}{f_0} = \Phi\left[(1 - X_C)^{I_1} - \alpha_1\right]^2 \qquad (3)$$

where

$$I_1 = \left[\int dt/t_2^*\right]^{n_2} \qquad (4)$$

Here Φ is a proportionality constant, while t_2^* denotes the time taken to precipitate a certain fraction ($X=X_c$) of β' at an arbitrary temperature T. The variation of t_2^* with temperature is given as /5, 8/:

$$t_2^* = t_{r2}^* \exp\left[\frac{A_0}{R}\left(\frac{1}{T(T_{eq} - T)^2} - \frac{1}{T_r(T_{eq}^* - T_r)^2}\right) + \frac{Q_d}{R}\left(\frac{1}{T} - \frac{1}{T_r}\right)\right] \qquad (5)$$

6.4.1.2 Response equation

The strength of 6XXX-alloys is primarily determined by the density and size of the hardening β''-(Mg$_2$Si) precipitates. In the model, the local strength level is calculated via a so-called response equation, which is based on simple dislocation theory /8, 5/:

$$\alpha = \left(HV - HV_{min}\right)/\left(HV_{max} - HV_{min}\right) = f/f_0 \qquad (6)$$

Here HV_{min} denotes the intrinsic matrix strength after complete particle dissolution, while HV_{max} is the original base metal strength in the T6 temper condition.

6.4.1.3 Input parameters

Table 2 summarises the input parameters used in the AA6082-T6 microstructure model. These values are, with one exception, the same as those used previously by Myhr and Grong /5/.

Table 2 Summary of input data used in AA6082-T6 microstructure model /5/.

Parameter	Value
Q_s	30 [kJ/mol]
Q_d	130 [kJ/mol]
$t_{r_1}^*$ (at 375°C)	200 [s] *
HV_{max}	110 [VPN]
HV_{min}	42 [VPN]
A_0	3.6 10^8 [JK^2/mol]
T_s	520 °C
$t_{r_2}^*$ (at 350°C)	3 s

* The value is taken from Ref. /7/

6.4.2 AA7108.50-T79 weldments

Typically, the 7108.50 variant contains 5.4wt% Zn and 0.8wt% Mg. This means that the alloy contains excess Zn compared to the Mg-rich 7108.70 variant described in Part I of the thesis (Section 1.5.3). Thus, some modifications of the previously reported microstructure model are required.

6.4.2.1 Precipitate stability

Information about phase relations within the Al-Zn-Mg system can be obtained from well-established sources /9/. Figure 15(a) shows the calculated solvus boundary for the equilibrium η phase in 7108.50, where the matrix concentration is assumed to follow the stoichiometric line for decomposition of pure MgZn$_2$ in Figure 15(b).

Mathematically, the variation in the Zn concentration with temperature can be described as:

$$C = C^* \exp\left(-\frac{\Delta H_{app}}{RT}\right) \qquad (7)$$

where ΔH_{app} is the apparent solvus boundary enthalpy for the reversible dissolution/precipitation reaction. The other symbols have their usual meaning and are defined in Appendix 6.1.

Based on the above relation it is possible to calculate the equilibrium solvus temperature T_{eq} as a function of composition from the data reported by Philips /9/. By substituting the appropriate values for C^* (in wt%) and ΔH_{app} (in J/mol) into equation (7) and equating with respect to T_{eq}, we obtain:

$$T_{eq}(°C) \approx \frac{-35550}{R\ln(C/5004)} - 273 \qquad (8)$$

where $C = C_{Zn} - C_{Zn}^0 = C_{Zn} - 1.0943$

From a thermodynamic standpoint the hardening precipitates will be less stable than the equilibrium η phase at elevated temperatures. Their dissolution temperature can, in turn, be estimated by considering the influence of particle

curvature on the solid solubility through the Gibbs-Thompson equation according to the procedure described in Part I of the thesis:

$$T_{eq}' = T_{eq} \frac{\Delta H_{app} - \Omega}{\Delta H_{app}} \qquad (9)$$

By combining equation (8) with equation (9), it is possible to express T_{eq}' solely in terms of measurable quantities:

$$T_{eq}'(°C) \approx \left(\frac{35550 - \Omega}{35550} \right) \left(\frac{-35550}{R \ln(C/5004)} \right) - 273 \qquad (10)$$

Equation (10) provides a means for estimating the metastable solvus boundaries for the GP-zones and the η phase in 7108.50, using input data from Table 3. The results from such computations are included in Figure 15 (a). In both cases it is assumed that a single value of Ω holds for each type of precipitates rather than allowing for spatial variations in the particle size of a given type. Although this represents an oversimplification of the problem, its relevance to welding is thought to be acceptable in the context of the mathematical model being developed.

Table 3 Summary of input data used in the thermodynamic model for the AA7108.50-T79 alloy /2/.

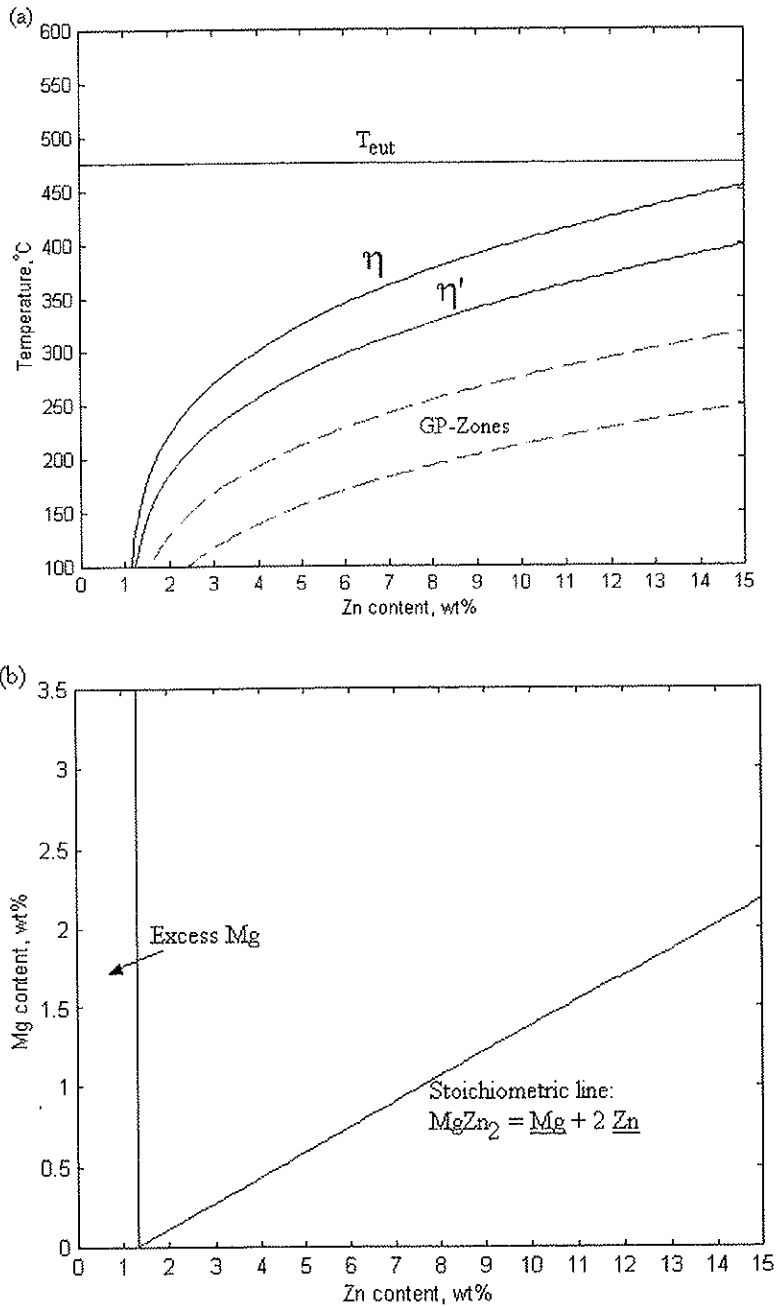| Parameter	Value	Comments
γ	0.25 J m^{-2}	Fixed for all precipitates
V_m	2x10^{-5} m^3 mol^{-1}	Fixed for all precipitates
$r_o(\eta')$	3.7 nm	Reasonable average value
r_o (GP-zones)	1-1.5 nm	Typical range reported for GP-zones /10/

Figure 15 Phase relations within the 7108.50 alloy system; (a) Predicted stable and metastable solvus boundaries, (b) Resulting change in matrix concentrations during phase decomposition.

6.4.2.2 Kinetics of particle dissolution

In general, phase changes in metals and alloys involve three basic steps, i.e. nucleation, growth and coarsening. However, when a previous stabilised microstructure is subjected to rapid heating, the material will respond to this change by a process of reversion. Consequently, in the present case it is sufficient to consider the kinetics of particle dissolution in order to model the extent of HAZ softening occurring during friction stir welding.

As a starting point, the so-called invariant size solution of Whelen /11/ is considered for the limiting case where the transient part of the diffusion field around the particles can be neglected:

$$\frac{dr}{dt} = -\frac{C_i - C_m}{C_p - C_i}\frac{D}{r}$$

(11)

It follows that the particles will start to dissolve when C_i exceeds C_m. The mean solute concentration in the matrix, C_m, will, in turn, depend on the instantaneous volume fraction of hardening precipitates in the material, and can be calculated from the lever rule /6/:

$$C_m = C_0\left(1 - \frac{f_0(r/r_0)^3}{f_m}\right)$$

(12)

Based on equations (11) and (12) it is possible to quantify the extend of particle dissolution occurring during FSW. However, because of the direct coupling between the particle radius r and the matrix concentration C_m, no closed isokinetic solution can be found in this particular case. Hence, integration must be carried out stepwise with time over the actual thermal cycles, as shown by the MatLab algorithm listed in Appendix 6.2.

6.4.2.3 Response equations

The next step is to develop a model for the precipitation strength loss. For simplicity, particle shearing is assumed to be the dominant strengthening mechanism both in the base metal and within the weld HAZ. Under such conditions the following expression was derived in Part I of the thesis (Section

1.5.3.4), relating the strength loss to the current value of the mean particle radius:

$$\alpha_1 = \frac{S_1 - S_{min}^0}{S_{max}^0 - S_{min}^0} = \left(\frac{\Delta\sigma_p}{\Delta\sigma_{p,m}}\right) = \left(\frac{f}{f_0}\right)^{1/2}\left(\frac{r}{r_0}\right)^{1/2} = \left(\frac{f}{f_0}\right)^{2/3} = \left(\frac{r}{r_0}\right)^2 \qquad (13)$$

Here α_1 is referred to as the dimensionless strength parameter, while S_1 denotes a specific mechanical property such as hardness (HV) and strength. The maximum and minimum values S_{max}^0 and S_{min}^0 represent the hardness or strength in the aged hardened and fully reverted condition, respectively.

In Al-Zn-Mg weldments most of the strength will be recovered during subsequent natural ageing. From a kinetic standpoint natural ageing is an extremely difficult process to model because of the interaction between quenched-in vacancies and the GP-zone formation. However, purely on deterministic grounds the relationship between the matrix solute content C_m and the maximum fraction of hardening precipitates that forms during natural ageing Δf_p can be obtained from a simple 3-D kinetic (cell model), assuming site saturation and that the reaction is interface controlled /5, 6/. Based on these assumptions the following relationship was derived in Part I of the thesis (Section 1.5.3.5), relating the HAZ strength recovery to the corresponding natural ageing potential immediately after welding:

$$\alpha_2 = \frac{S_1 - S_2}{S_{max} - S_{min}^0} = \left(\frac{\Delta\sigma_p}{\Delta\sigma_{p,m}}\right) = \left(\frac{f_p}{f_{p,m}}\right)^{1/2}\left(\frac{r}{r_m}\right)^{1/2} = \left(\frac{C_m - C_m^0}{C_0 - C_m^0}\right)^2 \qquad (14)$$

Equation (14) predicts that the resulting HAZ hardness or strength following natural ageing will drop from $S_2 = S_{max}$ within the fully reverted region (where $C_m = C_0$) to some lower value $S_2 < S_{max}$ within the partly reverted HAZ because of the reduced solute content available for GP-zone formation. The increase in S_{max} with time can, in turn, be read from the experimental ageing curve shown in Figure 16 which applies to the 7108.50 alloy in the fully reverted condition.
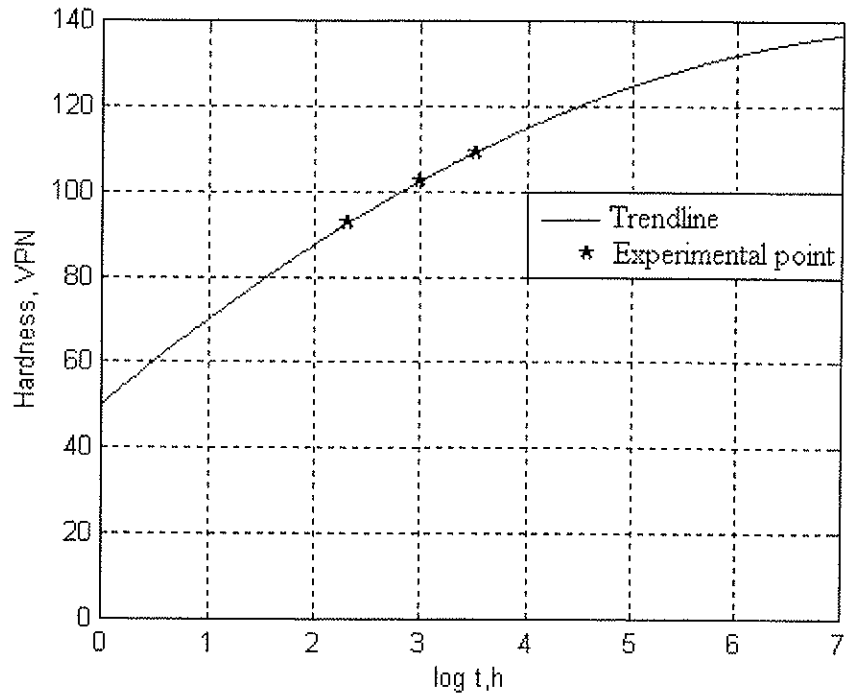
Figure 16 Experimental natural ageing curve for a fully reverted 7108.50-T79 alloy.

6.4.2.4 Summary of input data

The input parameters used in the microstructure model for the 7108.50-T79 alloy are summarised in Tables 4 and 5.

Table 4 Summary of input data used in the dissolution model for the 7108.50-T79 alloy /2/.

Parameter	Value	Comments
D_o	$1.05 \times 10^{-4} \mathrm{m}^2 \mathrm{s}^{-1}$	Reasonable average value /12/
Q	127.9 kJ mol^{-1}	Reasonable average value /12/
C_p	85 wt %	Fixed for all precipitates
f_o	0.016	Chosen
f_m	0.018	Calculated from a mass balance, assuming stoichiometric compound formation

Table 5 Summary of input data used in the strength model for the 7108.50-T79 alloy /2/.

Parameter	Value	Comments
S^o_{max}	120 VPN	Hardness in T79 temper condition
S^o_{min}	50 VPN	Hardness in fully reverted condition
C_o	5.4 wt %	Typical Zn content in base material
C^o_m	0.56 wt %	Calculated from equation (29) in Part I, using input data from Tables 3 and 4

6.5 Comparison between measured and predicted hardness profiles

In the following, the measured hardness profiles in Part IV of the thesis are compared with the predicted ones. The predicted hardness profiles are calculated via the subroutines and algorithms listed in Appendix 6.2, using the 3-D heat flow model developed in Part III of the thesis.

The results pertaining to the AA 6082-T6 and 7108.50-T79 weldments are summarised in Section 6.5.1 and 6.5.2, respectively. These data refer to welding at three different travel speeds, i.e. 5, 8 and 12 mm/s, respectively.

6.5.1 AA6082-T6 weldments

Figures 17 through 19 show a comparison between measured and predicted hardness profiles in the transverse direction of the AA6082-T6 welds following prolonged natural ageing.

Figure 17 Comparison between measured and predicted hardness profiles in Plate 1 after 270 hours of natural ageing. Operating conditions as defined in Part IV of the thesis (Appendix 4.1).

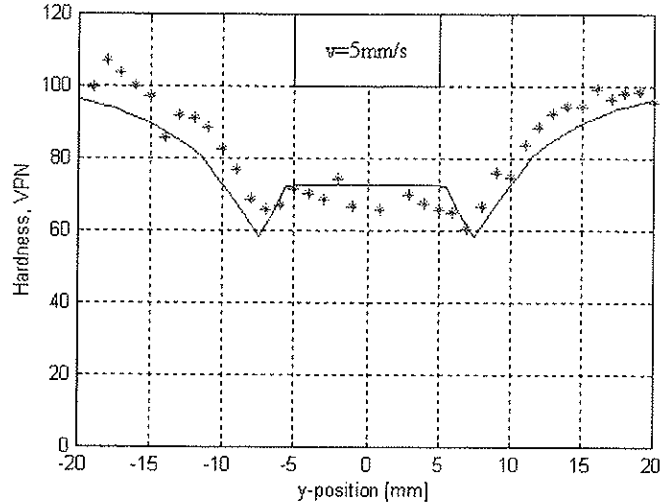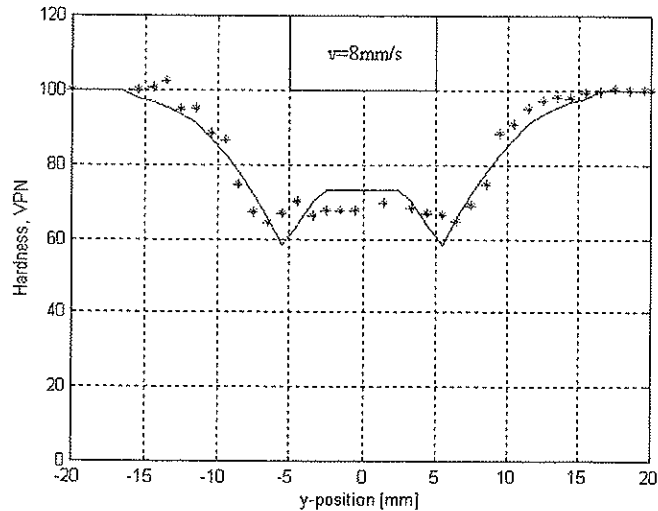Figure 18 Comparison between measured and predicted hardness profiles in Plate 2 after 400 hours of natural ageing. Operating conditions as defined in Part IV of the thesis (Appendix 4.1).
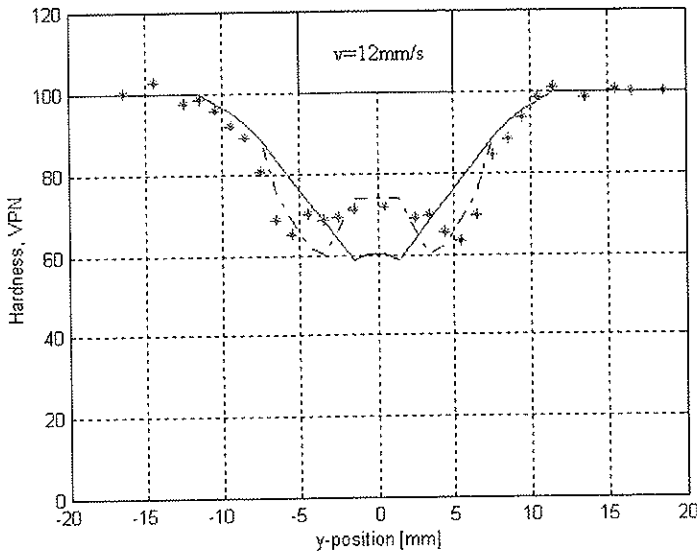
Figure 19 Comparison between measured and predicted hardness profiles in Plate 4 after 600 hours of natural ageing. Solid and broken curves refer to an input value of $t_{r_1}^*$ of 200 and 20s, respectively. Operating conditions as defined in Part IV of the thesis (Appendix 4.1).

In general, the combined microstructure and strength models are seen to predict adequately the response of the base material to FSW. This supports the previous conclusion in Part V of the thesis that thermal effects are the main cause for the observed strength loss during FSW of age hardening aluminium alloys. An exception is welding at high speeds, i.e. 12 mm/s (Figure 19), where parts of the HAZ fall within the plastically deformed region beneath the tool shoulder. In that case the predicted dissolution kinetics are too slow to account for the observed strength loss. The deviation arises probably from the fact that a plastically deformed material will respond much quicker to reheating than an undeformed material because the dislocation tangles within the substructure will act as high diffusivity paths for the solute atoms. In the present process model this "short circuiting" can be simulated by reducing the input value for the time constant $t_{r_1}^*$ in Table 2 from 200 to, say, 20 seconds so that full particle dissolution is achived within a narrow region beneath the tool shoulder during the welding operation (i.e. about ±2mm from the weld centre line). If such an empirical correction is included, a satisfactory agrement between theory and experiments is also obtained for the highest welding speed, as shown by the dotted hardness profile in Figure 19.

6.5.2 7108.50-T79 weldments

Figures 20 through 22 show a comparison between measured and predicted hardness profiles in the transverse direction of the 7108.50-T79 welds at different natural ageing times.

Figure 20 Comparison between measured and predicted hardness profiles in Plate 5 after 140 and 2600 hours of natural ageing, respectively. Operating conditions as defined in Part IV of the thesis (Appendix 4.1).

Figure 21 Comparison between measured and predicted hardness profiles in Plate 6 after 160 and 2700 hours of natural ageing, respectively. Operating conditions as defined in Part IV of the thesis (Appendix 4.1).
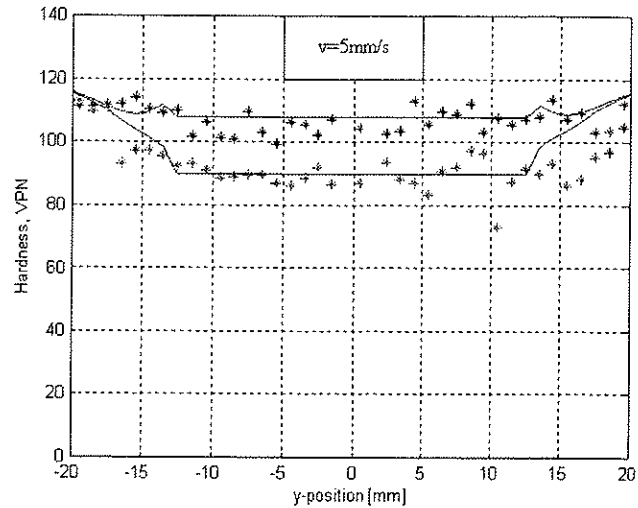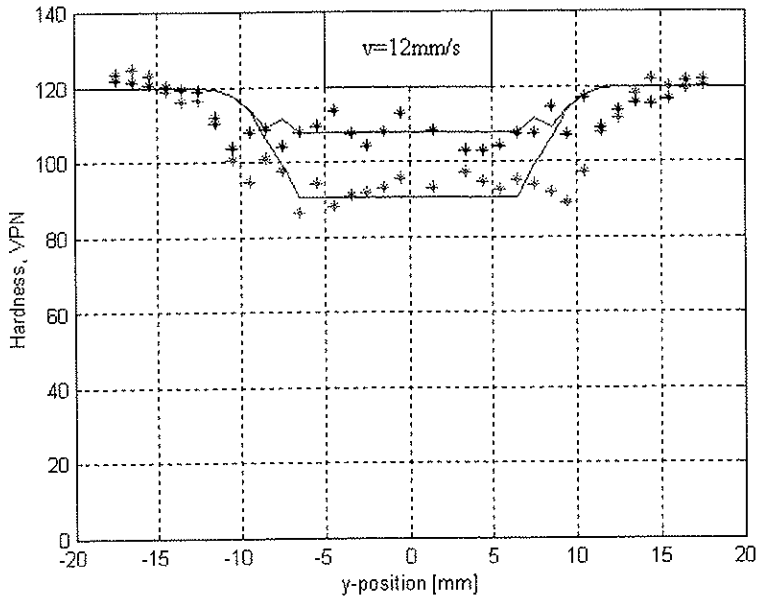
Figure 22 Comparison between measured and predicted hardness profiles in Plate 8 after 160 and 2600 hours of natural ageing, respectively. Operating conditions as defined in Part IV of the thesis (Appendix 4.1).
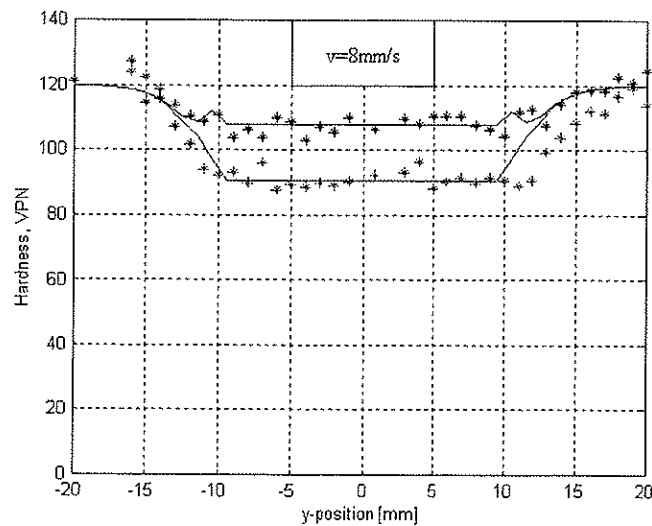
In general, the overall agreement between theory and measurements is good in the sense that the observed strength recovery after welding is adequately captured in the simulations. An interesting feature is that these welds do not reveal the characteristic drop in hardness within the partly reverted region of the HAZ, as frequently observed during fusion welding of similar materials /2/. It follows from Figures 20 through 22 that the strength recovery due to natural ageing occurs more or less evenly across the entire soft zone of the welds. This suggests that the conditions existing in FSW are different from those normally experienced during conventional fusion welding.

6.6 Conclusions

The basic conclusions that can be drawn from the experimental validation of the FSW process model are the following:

- In general, the 3-D heat flow model yields a temperature-time pattern that is consistent with experimental observations. Typically the computed peak temperatures are 20 to 30°C higher than the measured ones. This discrepancy is acceptable and within the accuracy of the thermocouple measurements.
- The implementation of the classical microstructure and strength models for fusion welding in the numerical code shows that thermal effects are the main cause for the observed strength loss during FSW of age hardening aluminium alloys. Only in cases where the welding speed is high, the plastic deformation introduced by the rotating tool will accelerate the dissolution of the hardening precipitates. This is because the HAZ and the plastically deformed region overlap at low heat inputs.

It is concluded that the combination of a microstructure model with an appropriate heat flow model creates a powerful tool for alloy design and optimisation of welding conditions for both Al-Mg-Si and Al-Zn-Mg extrusions.

6.7 References

1 O. Reiso, "The Effect of Composition and Homogenization Treatment on Extrudability of AlMgSi Alloys", Proceedings of the 3rd Int. Aluminium Extrusion Technology Seminar, Atlanta, GA, Aluminium Association, 1984, Vol.1, pp. 31-40.

2 B. Bjørneklett, Ph.D. Thesis, The Norwgian University of Science and Technology, Trondheim, Norway, 1998.

3 O.T. Midling Ph.D. Thesis, The Norwegian Institute of Technology, Trondheim, Norway, 1990.

4 Friction Data Guide: An Engineering Study of Coefficient of Friction of Materials and Coatings. Slide-chart presentation from General Magnaplate Corp., 1331 U.S., Route 1, Linden, NJ 07036, ©1988

5. O.R. Myhr and Ø. Grong: Acta Metall. Mater., 1991, vol 39, 2693-2702; ibid.,2703-2708.

6 Ø. Grong, Metallurgical Modelling of Welding, 2nd Ed., The Institute of Materials, London, 1997.

7 O.R. Myhr, Ø. Grong, S. Klokkehaug, H.G. Fjær and A.O. Kluken: Sci. Techn. Weld. Join., 1997, vol.2, pp.245-253.

8 D.H. Bratland, Ø. Grong, H.R. Shercliff, O.R. Myhr and S. Tjøtta: Overview No. 124 Acta Mater., 1997, vol 45, 1-22.

9 H. W. L. Philips, "Annotated Equilibrium Diagrams of Some Aluminium Alloys", 1959, London (UK), The Institute of Metals.

10 J. E. Hatch, "Aluminum, Properties and Physical Metallurgy", 1984, Ohio (USA), American Soc. for Metals.

11 M. J. Whelan, Met. Sci., 1969, 5, 95-97.

12 P. E. Drønen and N. Ryum, Met. Trans. 25A, 1994, 521-530.

Appendix 6.1 - Nomenclature

A_0	material constant related to the potency of the heterogeneous nucleation cites in actual alloy (Jmol^{-1})
α	dimensionless supersaturation
α_1, α_2	dimensionless strength parameters
C_i	particle/matrix interface concentration (wt%)
C_m	mean solute concentration in the matrix (wt%)
C_p	solute concentration within the particle (wt%)
C_m^o	matrix solute content in stabilised base material (wt%)
D	diffusion coefficient (m^{2}s^{-1})
f	volume fraction of precipitates
f_m	maximum possible volume fraction of hardening precipitates that can form at absolute zero
f_0	initial volume fraction of precipitates in base material.
f^*	volume fraction of precipitates formed during natural ageing
HV_{max}	hardness in the temper condition (VPN)
HV_{min}	hardness in the fully reverted condition (VPN)
ΔH_{app}	apparent solvus boundary enthalpy (J mol^{-1})
I_1	kinetic strength of thermal cycle
n_1	time exponent
Q_d	activation energy for diffusion of Mg in Al (J mol^{-1})
R	universal gas constant (8.314 Jmol^{-1} K^{-1})
r	particle radius (m)
r_0	initial particle radius (m)
r_m	maximum size of GP-zones (m)
S_1	hardness or strength following particle dissolution (VPN or Pa)
S_2	hardness or strength following reheating and natural ageing (VPN or Pa)
S_{max}^o	hardness or strength in age hardened base material (VPN or Pa)
S_{max}	maximum hardness or strength following natural ageing (VPN or Pa)
S_{min}^o	hardness or strength in fully reverted condition (VPN or Pa)
T	chosen reference temperature (°C, K)
T_r, T_{r_1}	chosen reference temperature (°C, K)
T_s	phase boundary solvus temperature

T_{eq}	equilibrium solvus temperature of actual alloy (°C, K)
T_{eq}^{*}	equilibrium solvus temperature of reference alloy (°C, K)
T_{eq}'	metastable solvus temperature (°C or K)
t	time (s)
t_{r_1}	retention time (s)
t_1^{*}	maximum holding time for complete dissolution (s)
t_2^{*}	time taken to precipitate a certain fraction, defined by the C-curve (s)
$t_{r_1}^{*}$	maximum hold time for complete dissolution at reference temperature (s)
t_{r2}^{*}	time taken to precipitate a certain fraction of β'-Mg$_2$Si at a chosen reference temperature (s)
V_m	molar volume (m^{3}mol^{-1})
X_c	fraction transformed
Φ	proportionality constant
Ω	contribution of the interface curvature to the reaction enthalpy (J mol^{-1})
$\Delta\sigma_p$	net precipitation strength increment (Pa)
$\Delta\sigma_{p,m}$	net precipitation strength increment in base material (Pa)
γ	interfacial energy (Jm^{-2})

Appendix 6.2 – MatLab Algorithms used for Calculation of the Microstructure Evolution during FSW

```
function HVplan=hvplan(Ttot,dts,xpos,model);

%This function calculates the resulting hardness distribution at x-position,
%xpos, from the variable Ttot containing the whole thermal history for the
%plate during welding and cooling. Ttot is obtained from the function Thist
%listed in Appendix 3.2.

%model=1, Al-6082
%model=2, Al-6082 (tref=20 in deformed region)
%model=3, Al-7108.70-T6 (as described in Ref./2/)
%model=4, Al-7108.50-T79

l=max(size(Ttot));
[x,y,z]=size(Ttot{1,1});
HVplan=zeros(1,y,z);

T=zeros(l,1);
i=xpos;

if model==1
  for j=1:y
    for k=1:z
      for a=1:l
        T(a)=Ttot{1,a}(i,j,k);
      end
      HVplan(1,j,k)=HVhaz(T,dts); %dissolution and ageing model 6082-T6
from Myhr and Grong.
    end
  end

  yzplot(HVplan,1,[50 55 60 65 70 75 80 85 90 95 99 100],2);
end %end val=1

if model==2
  for j=1:y
    for k=1:z
```

```
   for a=1:1
      T(a)=Ttot{1,a}(i,j,k);
   end
   if j<8
      HVplan(1,j,k)=HVhazd(T,dts);
%dissolution and ageing model 6082-T6 from Myhr and %Grong.
   else
      HVplan(1,j,k)=HVhaz(T,dts);
%dissolution and ageing model 6082-T6 from Myhr and %Grong.
   end
  end
 end

 yzplot(HVplan,1,[50 55 60 65 70 75 80 85 90 95 99 100],2);

end %end val=2

if model==3
  for j=1:y
    for k=1:z
      for a=1:1
        T(a)=Ttot{1,a}(i,j,k);
      end
      [S2,r,rsol,rtime]=solut(T,dts);
      HVplan(1,j,k)=S2;
    end
  end

  yzplot(HVplan,1,[120 125 130 135 140 145],2);

end %end val=3

if model==4
  for j=1:y
    for k=1:z
      for a=1:1
        T(a)=Ttot{1,a}(i,j,k);
      end
      [S2,r,rsol,rtime]=solut50(T,dts);
      HVplan(1,j,k)=S2;
```

```
        end
    end

    yzplot(HVplan,1,[90 95 100 105 110 115 119 120],2);

end %end val=4
```

Procedures used to calculate the microstructure evolution in AA6082-T6 weldments

```
function HV=HVhaz(Temp,dts);
HVmin=42;
HVmax=100;

%Calculating resulting hardness for all thermal %history. %From PhD thesis
Myhr pp.59
X=micro(Temp,dts); %dissolution model
X2=micro2(Temp,X,dts); %ageing model

if X2>X
    HV=HVmin+(HVmax-HVmin)*X2; %resulting hardness
end

if X>X2 | X==X2
    HV=HVmin+(HVmax-HVmin)*X; %resulting hardness
end

function X=micro(Ts,dts);
% dissolution model
clear X;
Qs=30000;   %[J]
Qd=130000;  %[J]
Tref=375;   %[°C]
R=8.31;
tref=200; %[s]
[l1,l2]=size(Ts);
% To avoid problems with [1 x] and [x 1] matrixes.
if l1<l2
    l1=l2;
end
```

```
sumval=0;

%Function 4-36; Metallurgical Modelling of Welding by %Grong.
for i=1:11
   ts=tref*exp(((((2*Qs)/R)+(Qd/R))*(1/(Ts(i)+273)-1/(Tref+273))));
   tval=dts/ts;
   sumval=sumval+tval;
end


%taking account for impigement of diffusion fields,
%fig. 4.20 pp.329 Metallurgical Modelling of Welding %by Grong.
%Functions taken from program text pp.118 procedure %"Xd_vs_Integral"
PhD thesis Myhr.
if log10(sumval)>0.0 | log10(sumval)==0.0
   X=0;
end
if log10(sumval)<-6.55
   logX=-10.2*(exp(-0.014*-6.55)-1)-1.486e-4*(6.55)^4.3396;
   X2=1-exp(2.302585*logX);
   X=1-10^(log10(exp(0.5*2.30258*log10(sumval)))+log10(exp(0.5*2.30258*-
6.55))-log10(X2));
end
if log10(sumval)<0.0 & log10(sumval)>-6.55
   logX=-10.2*(exp(-0.014*log10(sumval))-1)-1.486e-4*(-
log10(sumval))^4.3396;
   X=1-exp(2.302585*logX);
end


function X2=micro2(Ts,alfa,dts);
%ageing model
Qd=130000;  %[J]
Tref2=350;
tref2=3;
Ts2=520;

R=8.31;
A0=3.6e8;

[l1,l2]=size(Ts);
```

```
% To avoid problems with [1 x] and [x 1] matrixes.
if l1<l2
    l1=l2;
end

sumval2=0;

%function 32 pp. 58 PhD thesis Myhr
for i=1:l1
    if Ts(i)>=450 | Ts(i)<=200
        tval2=0;
    end
    if Ts(i)<450 & Ts(i)>200
        A=1/((Ts(i)+273)*(Ts2-Ts(i))*(Ts2-Ts(i)));
        B=1/((Tref2+273)*(Ts2-Tref2)*(Ts2-Tref2));
        C=1/(Ts(i)+273)-1/(Tref2+273);
        t2s=tref2*exp(A0/R*(A-B)+Qd/R*C);
        if t2s<1e-20 % to avoid dividing by zero!
            t2s=1e-20;
        end
        tval2=dts/t2s;
    end
    sumval2=sumval2+tval2;
end

if sumval2>1
    sumval2=1;
end

alfa2=0.56*(0.95)^sumval2;
X2=0.56*(sqrt(alfa2/0.56)-alfa)^2;


function HV=HVhazd(Temp,dts);
HVmin=42;
HVmax=100;

%Calculating resulting hardness for all thermal %histories.
%From PhD thesis Myhr pp.59
```

```
X=microd(Temp,dts); %dissolution model
X2=micro2(Temp,X,dts); %ageing model

if X2>X
  HV=HVmin+(HVmax-HVmin)*X2; %resulting hardness
end

if X>X2 | X==X2
  HV=HVmin+(HVmax-HVmin)*X;  %resulting hardness
end


function X=microd(Ts,dts);
% dissolution model in deformed material.
clear X;
Qs=30000;  %[J]
Qd=130000;  %[J]
Tref=375;  %[°C]
R=8.31;
tref=20; %[s]
[l1,l2]=size(Ts);
% To avoid problems with [1 x] and [x 1] matrixes.
if l1<l2
  l1=l2;
end

sumval=0;

%Function 4-36; Metallurgical Modelling of Welding by Grong.
for i=1:l1
  ts=tref*exp((((2*Qs)/R)+(Qd/R))*(1/(Ts(i)+273)-1/(Tref+273)));
  tval=dts/ts;
  sumval=sumval+tval;
end

%taking account for impigement of diffusion fields,
%fig. 4.20 pp.329 Metallurgical Modelling of Welding by Grong.
%Functions taken from program text pp.118 procedure "Xd_vs_Integral"
%PhD thesis Myhr.
if log10(sumval)>0.0 | log10(sumval)==0.0
```

```
    X=0;
end
if log10(sumval)<-6.55
    logX=-10.2*(exp(-0.014*-6.55)-1)-1.486e-4*(6.55)^4.3396;
    X2=1-exp(2.302585*logX);
    X=1-10^(log10(exp(0.5*2.30258*log10(sumval)))+log10(exp(0.5*2.30258*-
6.55))-log10(X2));
end
if log10(sumval)<0.0 & log10(sumval)>-6.55
    logX=-10.2*(exp(-0.014*log10(sumval))-1)-1.486e-4*(-
log10(sumval))^4.3396;
    X=1-exp(2.302585*logX);
end
```

Procedures used to calculate the microstructure evolution in AA7108.70-T6 weldments

```
function [S2,r,rsol,rtime]=solut(T,time);
%This function calculates the solution of particles in a AlMgZn alloy on the
%basis of a temperature and time vector: r=solut(T,time);
%Output is a vector containing change in particle radius.
%Al-7108.70-T6

%constants
Cp=85;   %[wt%]
C0=5.4;  %[wt%]
C0m=0.56;%[wt%]
f0=0.02;
fm=0.0223;
D0=1.05E-4; %[m2/s]
Q=127900; %[J/mol]

aget=1; %[hours]
Smax=55+24.167*log10(aget)-1.8333*(log10(aget))^2;  %[VPN]
S0max=140; %[VPN]
S0min=55; %[VPN]

R=8.31434; %[J/Kmol]

gam=0.25;  %[J/m2]
```

```
Vm=2E-5;   %[m3/mol]
r0=2.5E-9; %[m]

omega=2*gam*Vm/r0;

[a,b]=size(T);
% To avoid problems with [1 x] and [x 1] matrixes.

if a<b
  r=zeros(a,b+1)+r0;
  a=b;
else
  r=zeros(a+1,b)+r0;
end

rsol=r;

for i=1:a
  Ci=2590*exp((omega-32000)/(R*(T(i)+273)));
  Cm=C0*(1-f0*(r(i)/r0)^3/fm);
  if i==a
    dt=time(a)-time(a-1);
  else
    dt=time(i+1)-time(i);
  end
  D=D0*exp(-Q/(R*(T(i)+273)));
  if r(i)==0
    dr=0;
  else
    dr=-((Ci-Cm)/(Cp-Ci))*D/r(i)*dt;
  end
  r(i+1)=r(i)+dr;
  if r(i+1)<0   %checking if particle has gone into solution.
    r(i+1)=0;
  end
  if dr<0
    rsol(i+1)=r(i+1);
  else
    rsol(i+1)=rsol(i);
  end
```

```
end
rtime=time;
rtime(a+1)=rtime(a)+rtime(2);

alfa1=(rsol(a)/r0)^2;
Cm=C0*(1-f0*(rsol(a)/r0)^3/fm);
alfa2=((Cm-C0m)/(C0-C0m))^2;

S2=S0min+alfa1*(S0max-S0min)+alfa2*(Smax-S0min); %check S0max in
equation!!!
```

Procedures used to calculate the microstructure evolution in AA7108.50-T79 weldments

```
function [S2,r,rsol,rtime]=solut50(T,time);
%This function calculates the solution of particles in a AlMgZn alloy on the
%basis of a temperature and time vector: r=solut(T,time);
%Output is a vector containing change in particle radius.
%Al-7108.50-T79

%constants
Cp=85;   %[wt%]
C0=5.4;   %[wt%]
C0m=0.56;%[wt%]
f0=0.016;
fm=0.018;
D0=1.05E-4; %[m2/s]
Q=127900; %[J/mol]

aget=2600; %[hours]
Smax=50+21.2886*log10(aget)-1.27067*(log10(aget))^2; %[VPN]
S0max=120; %[VPN]
S0min=50; %[VPN]

R=8.31434; %[J/Kmol]

gam=0.25;  %[J/m2]
Vm=2E-5;   %[m3/mol]
r0=3.7E-9; %[m]
```

```
omega=2*gam*Vm/r0;

[a,b]=size(T);
% To avoid problems with [1 x] and [x 1] matrixes.

if a<b
  r=zeros(a,b+1)+r0;
  a=b;
else
  r=zeros(a+1,b)+r0;
end

rsol=r;

for i=1:a
  Ci=5004*exp((omega-35550)/(R*(T(i)+273)));
  Cm=C0*(1-f0*(r(i)/r0)^3/fm);
  if i==a
    dt=time(a)-time(a-1);
  else
    dt=time(i+1)-time(i);
  end
  D=D0*exp(-Q/(R*(T(i)+273)));
  if r(i)==0
    dr=0;
  else
    dr=-((Ci-Cm)/(Cp-Ci))*D/r(i)*dt;
  end
  r(i+1)=r(i)+dr;
  if r(i+1)<0   %checking if particle has gone into solution.
    r(i+1)=0;
  end
  if dr<0
    rsol(i+1)=r(i+1);
  else
    rsol(i+1)=rsol(i);
  end
end
rtime=time;
rtime(a+1)=rtime(a)+rtime(2);
```

```
alfa1=(rsol(a)/r0)^2;
Cm=C0*(1-f0*(rsol(a)/r0)^3/fm);
alfa2=((Cm-C0m)/(C0-C0m))^2;
S2=S0min+alfa1*(S0max-S0min)+alfa2*(Smax-S0min); %check S0max in
equation!!!
```

PART VII: APPLICATIONS OF THE PROCESS MODEL

7.1 Introduction

In recent years, significant progress has been made in the understanding of physical processes that take place during welding of age hardening aluminium alloys/1,2,3/. A synthesis of that knowledge has, in turn, been consolidated into process models, which provide a mathematical description of the relation between the main welding variables (e.g. heat input, plate thickness, joint configuration etc.) and the resulting weld properties, based on sound physical principles. The components of such a model are:

(i)   A numerical heat flow model for prediction of the temperature time pattern during welding.

(ii)   Kinetic models for prediction of the microstructure evolution (e.g. volume fraction of hardening precipitates) as a function of time and temperature.

(iii)   Response equations, based on dislocation theory, which provide quantitative information about the HAZ hardness or strength following welding.

In Part VII of the thesis, the concept is further developed and applied to friction stir welding (FSW) of 6082-T6 and 7108-T79 extrusions. The former alloy is commonly used for structural applications, while 7108-T79 has traditionally been utilised in the production of autoparts such as bumpers, but are now also being used in load-bearing structures like ship deckings and stiffeners in different temper conditions (e.g. T4, T6 or T79).

7.2 Case study 1: Limitations in the heat input during FSW

In the following, three different case studies will be presented to illustrate the basic features of the process model and how the final properties achieved depend on the HAZ temperature distribution. Table 1 contains a summary of welding parameters used in the case study.

Table 1. Summary of welding parameters used in Case study 1.

Case No.	T_{max}* [°C]	w [rot/min]	P [MPa]	d [mm]	v [mm/s]	R [mm]	μ
case 1.1	555	1500	30	6	5	7.5	0.4
case1.2	555	1500	30	6	10	7.5	0.4
case1.3	555	1500	30	6	15	7.5	0.4

*Assumed maximum temperature beneath the tool shoulder.

By utilising the computer programme presented previously, it is possible to construct two-dimensional maps which show characteristic isothermal and hardness contours in the HAZ. Examples of such diagrams are given in Figures 1 through 3 for the combination of parameters listed in Table 1. These refer to welding of 100 mm wide and 150 mm long Al-Mg-Si plates in the T6 temper condition.
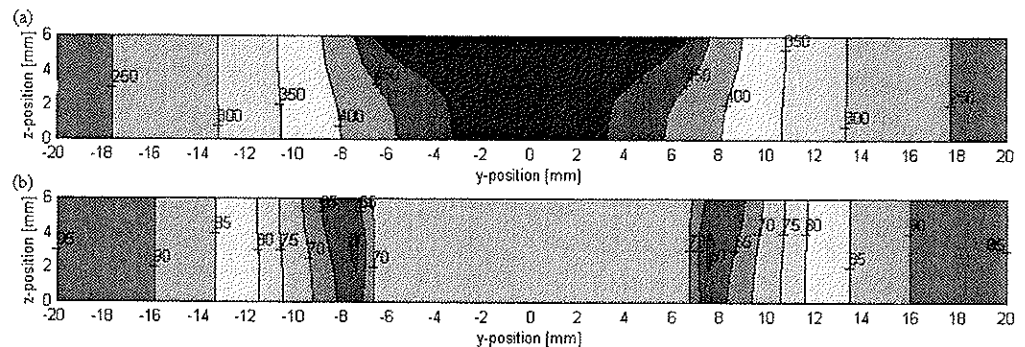

Figure 1a) Computed peak temperature contours in the cross section of the weld at pseudo-steady state b) Resulting HAZ hardness distribution following natural ageing [HV]; operating conditions as in Table 1 (case 1.1).
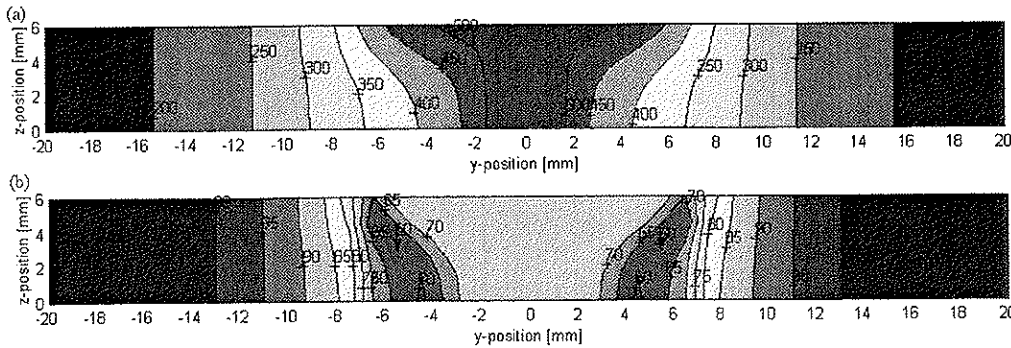
Figure 2a) Computed peak temperature contours in the cross section of the weld at pseudo-steady state b) Resulting HAZ hardness distribution following natural ageing [HV]; operating conditions as in Table 1 (case 1.2).
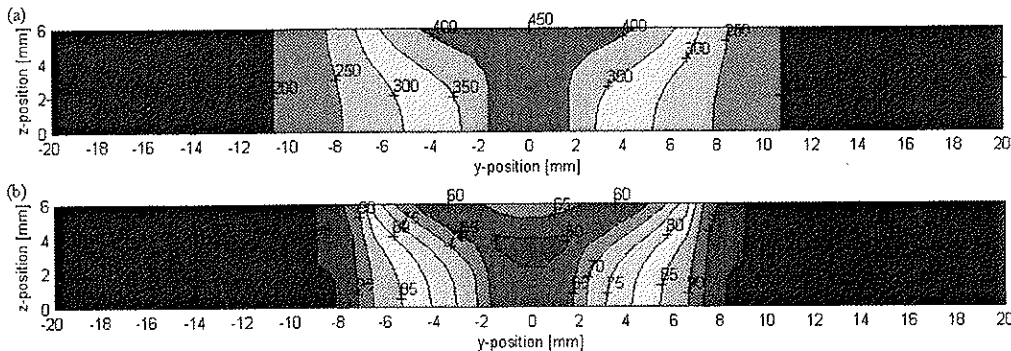

Figure 3a) Computed peak temperature contours in the cross section of the weld at pseudo-steady state b) Resulting HAZ hardness distribution following natural ageing [HV]; operating conditions as in Table 1 (case 1.3).

A closer inspection of the figures reveals a direct relationship between the HAZ thermal programme and the resulting hardness distribution following natural ageing. In general, a narrow width of the HAZ during FSW of Al-Mg-Si extrusions requires the use of a low energy input per unit area of the weld (i.e. a small q_0/vd ratio). As shown in Figure 3, the softest parts of the HAZ fall within the fully plasticized region of the weld when the travel speed is 15 mm/s. This observation is in sharp contrast to the results in Figures 1 and 2, where parts of the soft zone are located outside the fully plasticized region of the weld. In the latter case, the predicted HAZ hardness profiles closely resemble those observed during conventional arc welding of AA6082-T6 alloys/1,2/. This means that the potential of FSW cannot be fully utilised in engineering design, unless the heat input is reduced to minimise the strength

loss within the weld HAZ (compatible with the requirement of a sufficient preheating of the material in front of the tool shoulder).

7.3 Case study 2: Heat loss through the steel backing plate

In this case study, the process model will be used to evaluate how heat losses through the steel backing plate influence the thermal field and the resulting hardness distribution during FSW of 7108-T79 plates.

7.3.1 Problem description

During FSW a considerable amount of heat may be conducted through the steel backing plate if it is not properly insulated from the aluminium extrusion by means of a protective ceramic layer. In certain cases this may be desirable (e.g. when welding is carried out at very low speeds) because the use of a steel backing plate will reduce the HAZ strength loss and thereby improve the mechanical integrity of the joint. In other cases (e.g. in production of ship deckings), where a high welding speed is required, the heat generation itself will be a limiting factor. Under such conditions, thermal insulation of the backing plate is a better solution for the reasons given below.

In the simulations, the heat generated by the rotating action of the tool is allowed to diffuse into a 25mm thick steel backing where the lower surface is kept at a constant temperature of 25°C. Conversely, welding on an insulated backing plate is simulated by assuming that both the upper and the lower surface of the extrusion is impermeable to heat. The operating conditions are summarised in Table 2 for welding at a constant speed of 8mm/s. These case studies refer to welding of 100mm wide, 150mm long and 6mm thick Al-Zn-Mg plates in the T79 temper conditions.

Table 2 Summary of welding parameters used in Case study 2.

Case No.	T_{max}* [°C]	w [rot/min]	P [MPa]	d [mm]	R [mm]	μ	λ** [Wmm^{-1}°C^{-1}]
case2.1	555	1500	30	6	7.5	0.4	0
case2.2	555	1500	30	6	7.5	0.4	0.04

*Assumed maximum temperature beneath the tool shoulder.
** Thermal conductivity of backing plate.

7.3.2 Simulation results

Figure 4 shows how the thermal conditions in the front of the tool are influenced by the use of a steel backing plate. Here the position x=0 defines the centre of the tool shoulder. It is obvious that the heat diffusion into the steel backing plate reduces the peak temperatures beneath the tool shoulder at the same time as the thermal gradients ahead of the tool become considerably steeper.
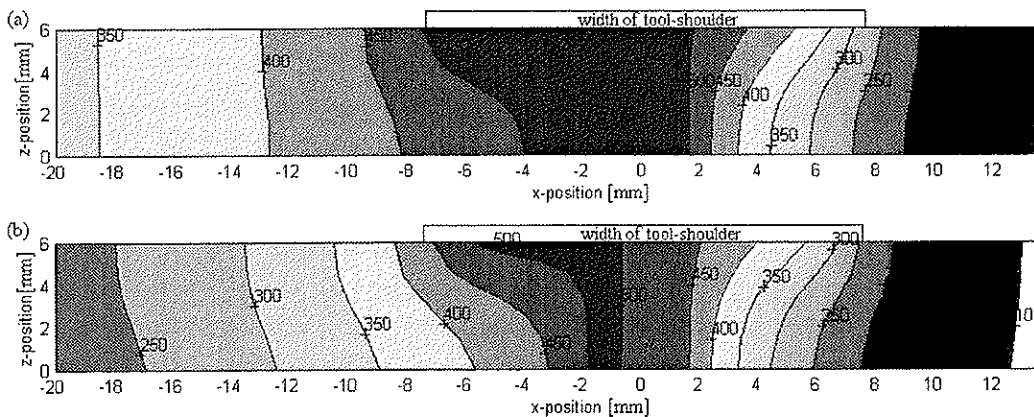

Figure 4 Predicted isothermal contours in the length direction of the plate under different welding conditions; (a) use of an insulated backing plate, (b) use of a steel backing plate. Operating conditions as in Table 2.

Because the use of a steel backing plate implies that the material is not adequately preheated before it reaches the tool shoulder, the flow stress will be so high that the material cannot adequately accommodate the subsequent plastic deformation. This will eventually lead to pin fracture and the formation of weld defects. This "cold" weld problem is well known from ordinary production welding, but can perhaps be overcome by simply employing an isolated backing plate, as illustrated in the present case study.

In practice, due consideration must also be given to the HAZ microstructure and strength evolution, as a highest possible load bearing capacity of the joint requires that the permanent strength loss after welding is minimised. The important relationship between the heat flow conditions and the resulting hardness distribution in the cross section of the welds is illustrated in Figures 5 through 7. From these figures it is obvious that the total width of the HAZ is smallest when a steel backing plate is used. However, because Al-Zn-Mg

weldments will regain most of their strength during subsequent natural ageing, the minimum HAZ hardness will essentially be the same in both cases.
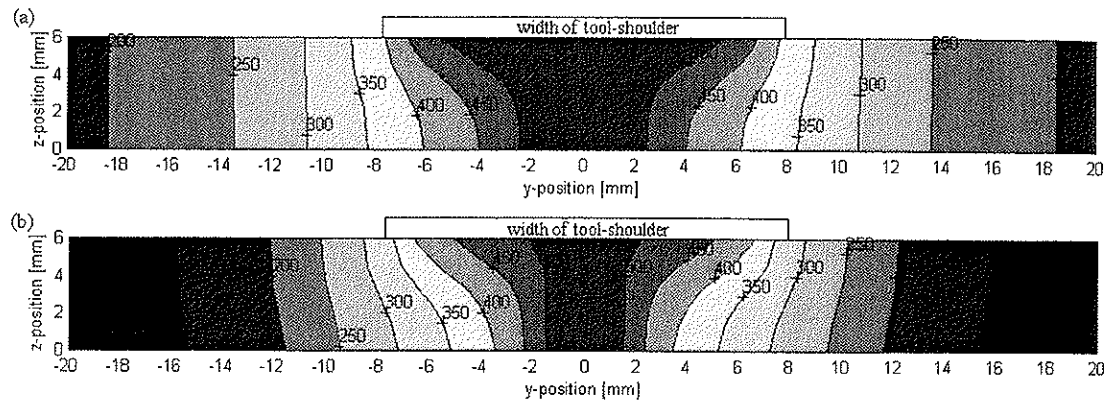

Figure 5 Predicted isothermal contours in the cross section of the plate under different welding conditions; (a) use of an insulated backing plate, (b) use of a steel backing plate. Operating conditions as in Table 2.
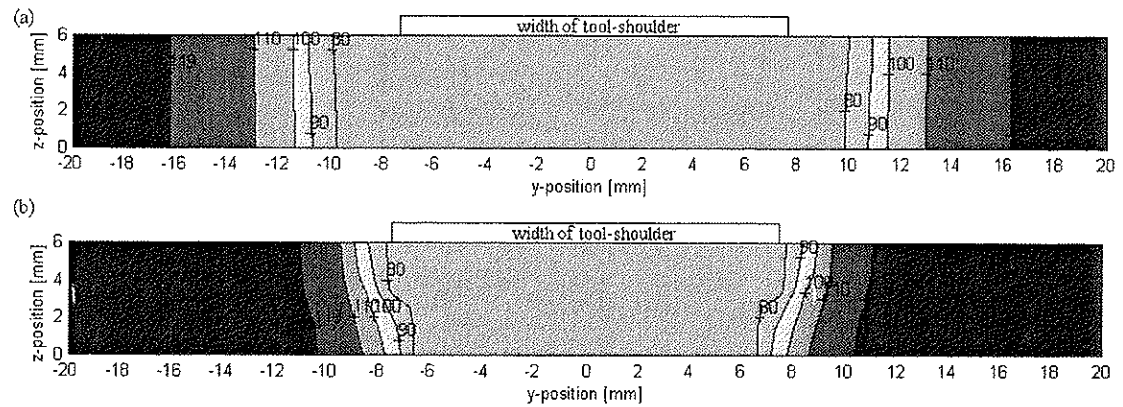

Figure 6 Predicted hardness distribution in the cross section of the plates after 24 hours of natural ageing; (a) use of an insulated backing plate; (b) use of a steel backing plate. Operating conditions as in Table 2.
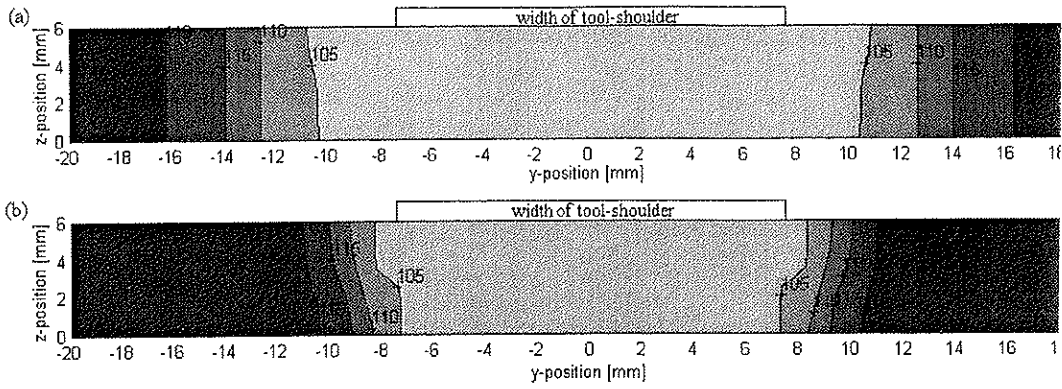
Figure 7 Predicted hardness distribution in the cross section of the plates after 4 weeks of natural ageing; (a) use of an insulated backing plate; (b) use of a steel backing plate. Operating conditions as in Table 2.

7.3 References

1. Ø. Grong: Metallurgical Modelling of Welding, Second Edition, The Institute of Materials, pp. 393, 1997.
2. O.R. Myhr and Ø. Grong: Acta Metall. Mater., 1991, 39, 2693-2702; ibid.,2703-2708.
3. Børge Bjørneklett, Ph.D thesis, Norwegian University of Science and Technology, 1998.